Dynamic Clearance Modelling of Steam Turbines

Prepared by:
Michael Anthony Jared Ross
RSSMIC022

Department of Mechanical Engineering
University of Cape Town

Supervisor:
A/Prof. Wim Fuls

January 2022

Submitted to the Department of Mechanical Engineering at the University of Cape Town in fulfilment of the academic requirements for a Master of Science degree in Mechanical Engineering

Key Words: TURBINE MODELLING, THERMAL EXPANSION, CLEARANCES, TURBINE START-UP, FINITE ELEMENT ANALYSIS, PROCESS MODELLING

Abstract

With the desire for conventional coal-fired power plants to perform flexible operations, the impact of this operation has become important to the field of steam turbine modelling. This study sought to develop a computationally inexpensive turbine model with minimal OEM input in order to predict the internal clearances of high-pressure and intermediate-pressure turbines from a large power utility's current turbine fleet.

The study saw the utilisation of the Nozzle Analogy theory to develop a 1D multistage turbine thermofluid model as well as the development of a representative 1D turbine process model in order to predict the fluid temperatures within a steam turbine during transient operation. From this model a further 3D FEA turbine model of both the HP and IP turbine units were developed using basic turbine diagrams to apply the predicted temperature boundaries and predict the thermal and structural transient loading response of turbine components during a full Cold Start procedure.

The result of this study was the successful validation, within a 10% error, of the 1D and 3D Turbine models against plant data from the candidate unit. This was in the form of known process data of unit performance, as well as thermocouple and differential expansion data taken from sensors housed on the turbine unit itself. Through the validation of these parameters, various calibration techniques were developed over the course of the study allowing investigators to gain insight into turbine aging, operator intervention as well as broad turbine component response. The successful establishment of the paired turbine model allowed investigators to evaluate the cold clearances defined during construction and maintenance of these turbine units in industry, which contributes greatly to the availability and efficiency of the unit during transient operations. Additionally, the establishment of this model allowed for an investigation of the role that start-up speed has on turbine component response.

This study demonstrated that the development of such a modelling methodology was possible and yielded results that were accurate and insightful in understanding turbine component responses which are otherwise impossible to measure during real-world operation.

Plagiarism Declaration

I, Michael Anthony Jared Ross, hereby declare the work contained in this dissertation to be my own. All information which has been gained from various journal articles, text books or other sources has been referenced accordingly. I have not allowed, and will not allow, anyone to copy my work with the intention of passing it off as their own work, or part thereof.

Signed by candidate

30 May 2022

Name - Michael Ross

Date

Acknowledgements

I wish to take this opportunity to acknowledge the following people and institutions for their help and assistance during this project:

- The Eskom Power Plant Engineering Institute (EPPEI) for providing the support and funding to pursue my masters research as well as the support from the Eskom Turbine Study Committee.
- The Applied Thermofluid Process Modelling (ATProM) research group, and my fellow postgraduate colleagues, for the professional support and mentoring during the course of my studies. The many coffee breaks and comradery will be cherished.
- The University of Cape Town for the opportunity and support to undertake my studies at a world-class institution
- A/Prof Wim Fuls for his constant mentorship and academic support during the course of the project, I feel that the growth I have seen as an engineer is as a direct result of the impact he has had. I will forever be thankful for your mentorship
- Dr Gary de Klerk for facilitating communications between myself and Eskom structures to ensure that I had the required information to perform my research in addition to the technical knowhow in the early development of the project
- To my parents, Jenny and Ashley, for firstly giving me the opportunity to pursue my aspirations, especially in the pursuit of postgraduate qualifications, as well as the emotional support and encouragement over the course of my education. I would not be here without you.
- Lisa Felix for the love and support during this project and my studies. For bearing with the overnight simulations and technical discussions over the dinner table. Thank you for always being by my side during this project.

Table of Contents

List of Figures

List of Tables

List of Nomenclature

General symbols

A - Through-flow area

A_{surf} - Surface area

c - Specific heat

g - Gravitational Acceleration ($g = 9.81$ m/s^2)

$\dot{m}$ - Steam mass flow

N_{stage} - Number of turbine stages

R - Gas constant

S - Secondary heat sources

T - Temperature

T_o - Ambient Temperature

T_∞ - Nominal inlet steam temperature

$T_{i.m}$ - Initial metal temperature

v_b - Blade velocity

dx - Element length

z - Number of seal teeth

Greek symbols

α - Stator exit flow angle

γ - Specific hear ratio of gas

λ_0 - Surface heat transfer convective coefficient

μ - Steam viscosity

ρ - Density

Acronyms and Abbreviations

OEM - Original Equipment Manufacturer

HPT - High Pressure Turbine

IPT - Intermediate Pressure Turbine
LPT - Low Pressure Turbine
FEM - Finite Element Modelling
FEA - Finite Element Analysis

1. Introduction

1.1 Problem Statement

With the growing contribution of renewable energy into the South African electrical grid, the operating principle of existing and future coal-fired power plants, that belong to the South African power utility, will see a shift from baseload to flexible operation. This will give rise to steam turbine units on such coal-fired power plants spending more time in transient operating conditions. The contribution of internal clearances in the efficiency and internal damage of steam turbines within Eskom's turbine fleet will become increasingly significant during these transient operations. With these clearances being impossible to measure in-service, as well as the unavailability of detailed geometric measurements from Original Equipment Manufacturers (OEMs) due to intellectual property protection, it is necessary for a numerical modelling solution to be formulated to predict these clearances.

1.2 Objectives

This study saw the development of a paired steam turbine modelling methodology in order to measure the internal clearance behaviour of turbine components during transient operations. The objectives of the study were to:

- Use the Nozzle Analogy Theory, formulated by Fuls [1], to accurately predict fluid temperatures through an operational steam turbine
- Develop a 3-dimensional FEA model of a candidate steam turbine to predict the thermal expansion of turbine components
- Accurately predict the internal clearance behaviour within an operational steam turbine during a full cold start-up procedure
- Establish the methodology with minimal OEM input (i.e. blade geometries and component sizing)
- Develop a methodology which was computationally inexpensive

1.3 Scope of Study

Scope

This study focused exclusively on the steam turbine modelling of a unit found within Eskom's coal-fired power plant fleet. Additionally, focus was placed on the modelling of the High Pressure (HP) and Intermediate Pressure (IP) turbines as these experience the largest temperature variations and expansion. This study focused on cold start-up of a candidate steam turbine. The study focused on the prediction of thermal expansion observed in turbine components with limited process data and turbine geometry.

Assumption

Some specific assumptions were made at the relevant modelling phases, but a general assumption was made that the heat balance diagrams collected from site represented a turbine unit designed for optimum operating conditions. Additionally, the heat balance diagrams were the expected behaviour of the unit in an “as-built” configuration.

Exclusions

This study excluded the prediction of thermal stresses generated within turbine components, in order to simplify the 3-dimensional models and to focus primarily on the thermal expansion of components. This work also excluded the detailed modelling of the Low-Pressure (LP) turbine due to the similarities in flow behaviours through the IP and LP units. As this study focused on the development of a methodology, it would be reasonable to expect the developed methodology to be applicable to the LP turbine as well.

1.4 General Methodology

The methodology employed in this study pursued two major outcomes:

1. The ability to model interstage fluid temperatures through an operational steam turbine with minimal geometric input from the turbine OEM (Reflected in Objectives 1, 2 and 4).
2. Utilise a paired modelling approach to create a comprehensive thermal picture of turbine component behaviour in a computationally inexpensive manner (Reflected in Objectives 1, 3, 4 and 5).

The methodology built on the research of Fuls and Clark [2], in using Flownex SE to develop a 1D thermofluid models of the HP and IP turbine units, using the Nozzle Analogy developed by Fuls [1]. The results of the Flownex SE model, detailing the steam temperature progression through the turbine flow passages, will then be used as thermal boundary conditions for a Finite Element Model (FEM) turbine model in order to predict the differential expansion and resulting clearance behaviours during the selected operating conditions. The methodology is represented in Figure 1, below.

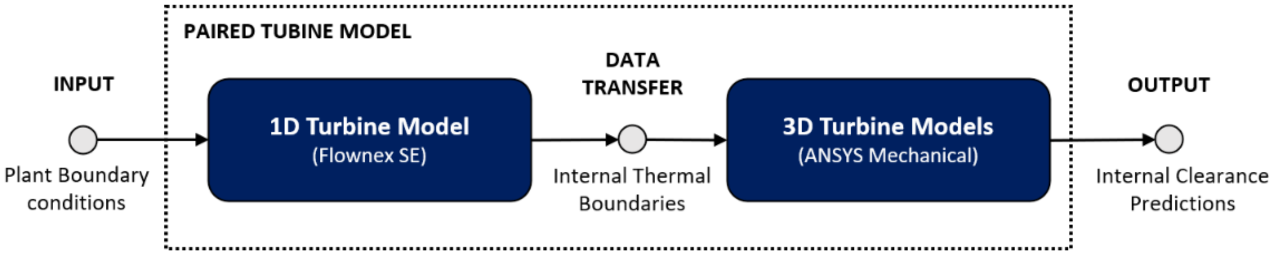

Figure 1: General Methodology

The focus of this study was the performance of the paired model methodology in predicting the clearance behaviour in steam turbines during transient operation. Therefore, the study focused on three particular operating conditions:

1. Steady State, Full-Load operation
2. Load Change Event
3. Cold Start-Up Procedure

Following the execution of the Cold Start-Up simulation, the clearance behaviour will be extracted from the 3D-FEM turbine model to comment on the efficacy of cold clearance and its effect on possible interference or inefficiencies brought about during turbine start-up.

1.5 Overall Report Structure

This report includes a review of literature delving into the South African electrical system, previous approaches taken in the transient modelling of steam turbines, and the introduction of the two software packages, Flownex SE and ANSYS Mechanical. In introducing these packages, the underlying heat transfer, thermodynamic and Finite Element Analysis (FEA) principal equations used by these packages will be explored.

The report details the development of a full one-dimensional (1D) turbine process model, capturing peripheral flow paths as well as the transient adaptation steam turbine modelling approaches developed by Fuls and Clark [1][2]. This is followed sequentially by a low-load validation of the results of the application of this 1D model against heat balance diagrams from the candidate unit, a transient load-change validation, and a full cold start-up procedure.

Building upon these results and validations, the report proceeds to detail the development of the three-dimensional (3D) HPT and IPT FEA models, using minimal geometric inputs. The FEA process, including a mesh independence study and boundary condition specification study, was included as a demonstration of the computational efficiency of the developed turbine model. Finally, a thermal and structural simulation of the cold start-up procedure is performed on the two FEA models, with clearance behaviours being captured from this phase of the study.

A final analysis of the findings gathered from both the 1D and 3D analyses is discussed with recommendations and conclusions offered.

2. Literature Review

2.1 Integrated Power Grids and thermal considerations

With increasing global awareness of climate change and the rise in the feasibility and use of renewable energy sources, it has become necessary to re-imagine the future of the generation and distribution of electricity. It follows that with increasing degrees of integration of renewable energy sources into the powder grid, conventional power generation through coal-fired power plants, traditionally operating at base load [3], will instead be required to undertake increasingly more flexible operations.

The global trend is evident within the South African context, a region rich in resources for renewable energy applications. In a recent study conducted by the Council for Scientific and Industrial Research (CSIR), it was concluded that by the end of 2019, 11.5 TWh was supplied by wind, solar photovoltaic (PV) and concentrated solar power (CSP) in South Africa [4], compared to only 2.2 TWh in 2014. A limitation of renewable energy production, particularly solar PV, is the dependence on weather conditions at the plant's location [3]. Therefore, unlike in conventional power plants, national renewable power production will fluctuate over a 24-hour period, giving rise to the idea of an integrated grid reflecting an interplay of renewable and more 'traditional' energy sources. Such an integrated electrical grid would be able to accommodate the described fluctuations in renewable energy production [3]. The vision of a fully integrated grid is one in which renewable energy sources would be deployed first, where possible, with conventional coal-fired power plants fulfilling the difference in supply and load.

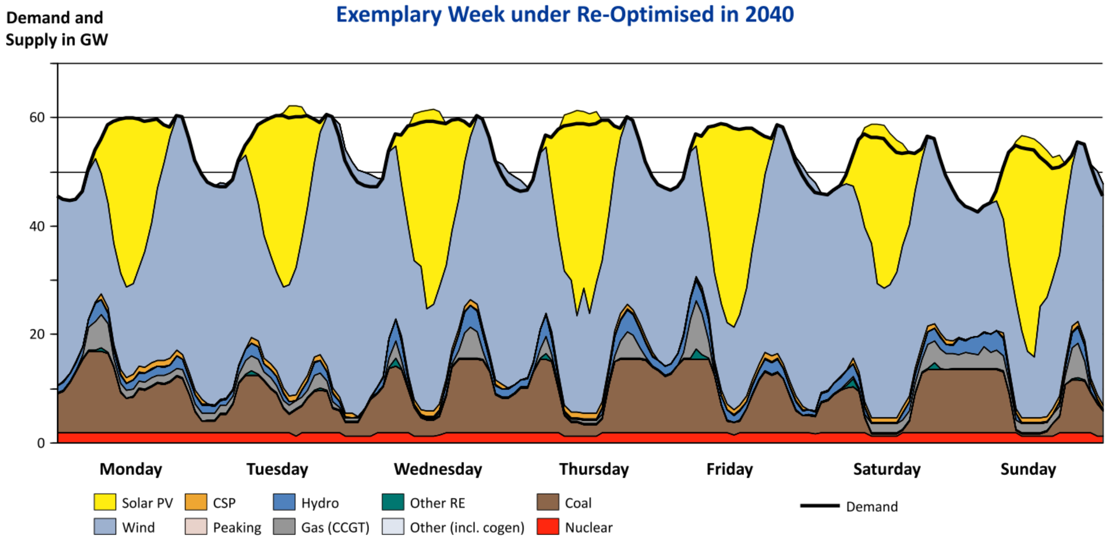

Figure 2: Optimised electrical mix in 2040 in South Africa [5]

Within the South African context, and in order to fully investigate the ability to transform the current grid to a more integrated form, it is beneficial to look at the means by which electricity is currently produced. Electricity is produced by Eskom, a State-Owned Enterprise (SOE) with the sole mandate to provide electricity to South Africa. Due to the abundance of coal in South Africa, the large majority of power plants are coal-fired (86%) with smaller percentages of nuclear (4%), hydroelectric (5%) and gas (5%) plants to support the rest of the grid [6]. This would suggest that the primary focus in creating an integrated grid in South Africa would be the performance of conventional coal-fired power plants in the new grid.

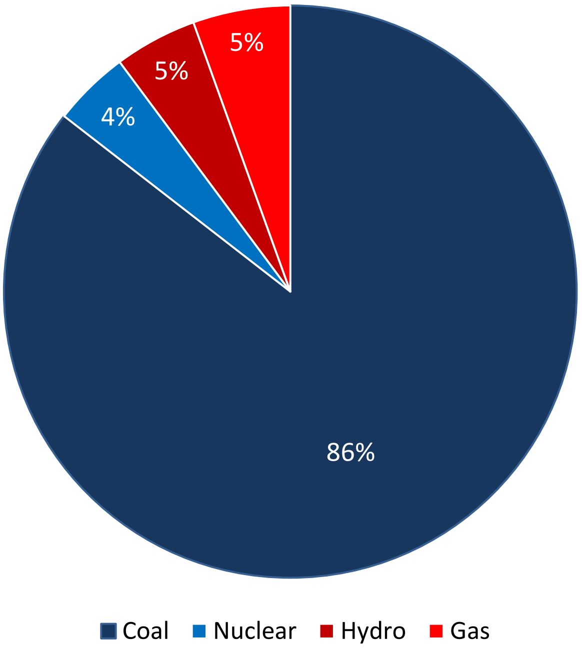

Figure 3: Eskom Power Generation Capacity Distribution as of 2020

However, since conventional coal-fired power plants were designed with a baseload operation in mind, a significant question for an integrated grid would be the capacity and challenges for conventional power plants to adopt a flexible operational mode going forward. Mills [3] looked at this very question, in an analysis of conventional coal-fired power plants fulfilling flexible operations. Mills suggested that the risks posed to plants were categorised as follows:

- Increased wear and tear of components
- Increased maintenance and outages, due to increased component failure
- Increased operation and maintenance costs to maintain efficiency of the plant
- Increased fuel costs and higher emissions due to reduced efficiency because of flexible operation

Mills Identifies the “boiler, steam turbine, emission control system… as well as auxiliary components” [3] as primary components of the power plant to be affected by flexible operation. He further suggests that the transients introduced by flexible operation pose a fatigue risk to high pressure components [3] and that particular strain is posed in the start-up and shut down of coal-fired power plants [3]. It is clear from Mills’ work that flexible operation of coal-fired power plants is not a straightforward shift in operational methodology and that a thorough understanding of integral plant components is vital to the safe, economical, and efficient operation of coal-fired power plants.

Thermal stresses that arise from fluctuating steam temperatures are common in flexible operation, and particularly evident in turbine operation. Turbine flexibility is limited by thermal stress considerations during operation [7], in that thermal stresses limit the rate of the transients of flexible operation.

Ramp rate, the ability for a plant to change load over a given time, is a pivotal component of the feasibility of conventional coal-fired power plants. The importance of ramp rate is illustrated in the Duck Curve [8], a graph used to illustrate the net power generation required to service a region’s full load.

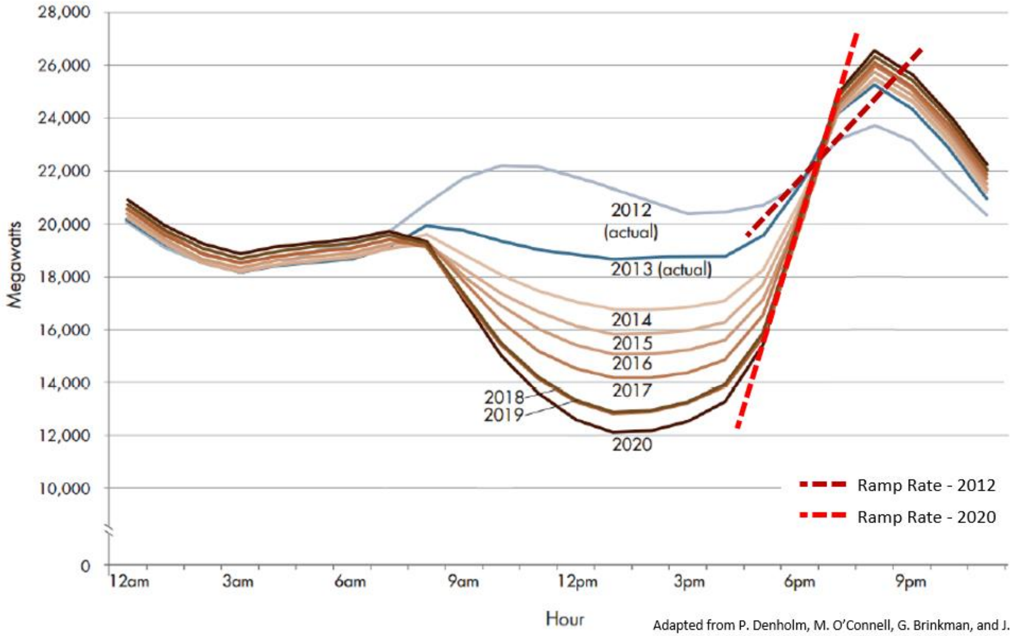

Adapted from P. Denholm, M. O’Connell, G. Brinkman, and J. Jorgenson, “Overgeneration from Solar Energy in California: A Field Guide to the Duck Chart

Figure 4: Duck Curve demonstrating net power generation required after solar PV contributions between 2012 and 2020

As is illustrated in Figure 4, solar photovoltaic (PV) generation can account for a substantial portion of the load required between 8am and 6pm, the times when the sun is shining. However, the transition seen after 6pm is where conventional coal-fired power plants will have to provide the required power. Figure 4 illustrates that with the steadily increasing capacity of solar PV between 2012 and 2020, there is an equivalent increase in the ramp rate needed from conventional power plants. It is for this reason that it would be vital for investigations to be focused on the effects that such increases in ramp rate would have on boilers, turbine units as well as the rest of a coal-fired power plant.

The concern of Mills for high pressure components, such as turbine units, during flexible operation is shared by Henderson [9] who further isolates the damage that can occur in the turbine rotors as well as in the turbine valves and casings [9]. The manifestations of the varying thermal load on these components are commonly seen in differential expansion of turbine components during times of flexible operation as well as during start-up and shut down.

2.2 Transient Turbine Modelling

Modelling the transient behaviour of steam turbines is of particular interest due to the abovementioned challenges posed by renewable energy, but also due to the regular make up of a particular national grid. In the Ukraine, for example, a lack of peak power brought about by the unreliability of the current turbine fleet [10] leads to frequent start-ups. A number of researchers have studied the effect that these frequent start-ups, and the natural cooling that precedes, has on the lifetime of turbine units. In the work of Tovazhnyanskyy [10], the need for such models was highlighted in providing the ability to quantify the effectiveness of making design modifications to the labyrinth seal compartments, as seen in Figure 5, to reduce the thermal stresses in turbine rotors during start-up.

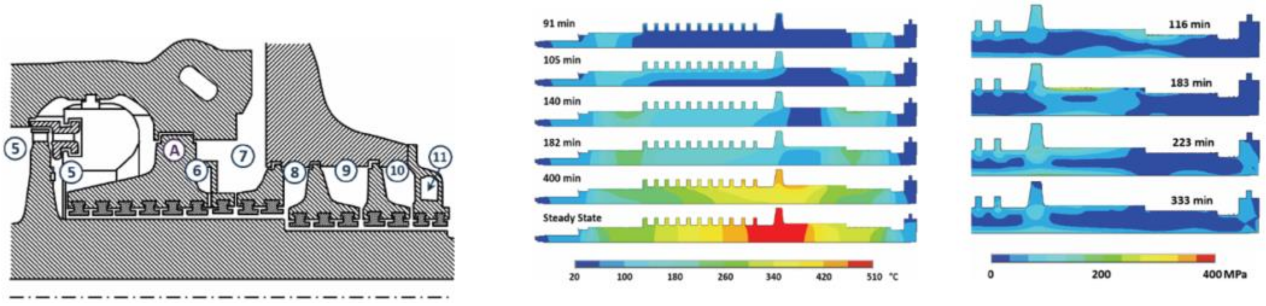

(i) (ii)

Figure 5: Seal configuration with rotor (i) temperature and (ii) Von Mises stress distribution [10]

In this work, it was evident that an understanding of the thermal behaviour of turbine components and the ability to simulate possible design modifications can result in the achievement of more efficient operations. The study further highlighted the sensitivity of turbine components during start-up, a sensitivity shown additionally in the work of Moroz [11] in the study of heat transfer between steam and rotors during cold start-up.

A review of the literature suggests that a comprehensive thermal analysis of the entire turbine unit is highly desirable. In the work of Born [12], a Conjugate Heat Transfer (CHT) model was utilised to model the thermal behaviour of a steam turbine during natural cooling. The study formulated a Computational Fluid Dynamics (CFD) approach seeking to capture the convective and conductive heat transfer behaviours in the turbine during a transient event of natural cooling after shut-down [12]. After steady state analysis, a strong agreement between calculated and measured temperature values was found, particularly in inner casing values. The steady state validation was followed by transient modelling. This methodology, consisting of a steady state validation followed by a transient investigation appears to be an efficient and logical methodology to ensure complete validation of the final thermal model. Using thermocouple data, a strong agreement was found between the calculated and measured data [12].

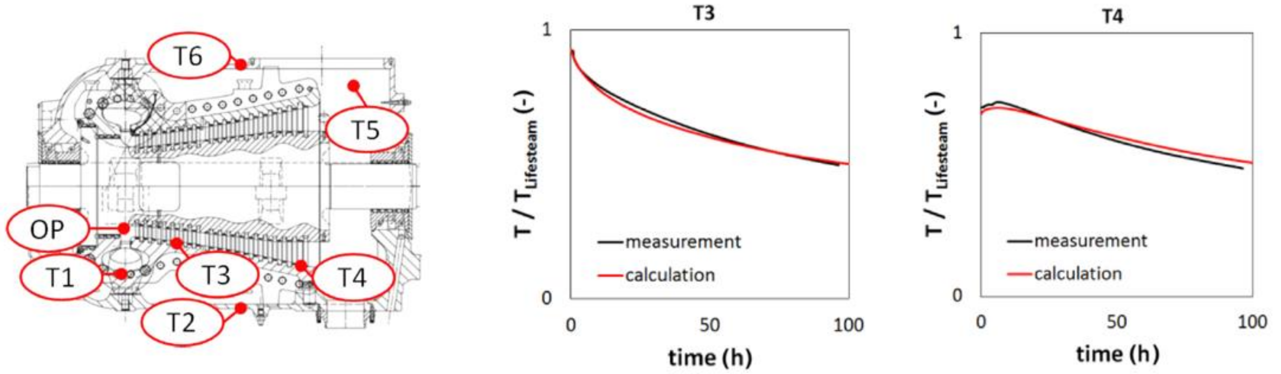

Figure 6: Thermocouple validations, from Born [12]

Born observed that the time scales between solid and fluid regions were very different and presented challenges in a pure CFD model [12], which suggests that a separately coupled model would be preferable. Born found that CFD also proved “time-consuming”, and therefore proposed the need for a simplified model. Of note was the fact that Born was privileged with significant geometric input from the turbine OEM, enabling the analysis of turbine cooling using a CFD methodology. In the work of Mukhopadhyay [13] the CFD model for the fluid field of that particular model consisted of 11.69 million nodes, and the accompanying 3D FEM model consisted of approximately 330 627 nodes. With limited computational power such a complete model would present challenges.

Thus, in simplified models, components would be geometrically simplified whilst maintaining surfaces and adjusting densities, where appropriate, in order to accurately capture component mass as well as a simplification of the fluid region of the model. Drawing from the work of

Marinescu, the concept of “over conductivity” [12][14] was identified as important. This concept visualises the fluid fields of the thermal model as a hyper-conductive solid region, representing the convective and conductive contributions of the fluid as a single scalar quantity; a linear combination of both convective and conductive heat transfer [15].

In later work, Marinescu proposed that the thermal behaviour of steam turbines is similar in both start-up and natural cooling, after unit shut down. The over-conductivity function, was used as representative in both events, and solved numerically based on reported fluid temperatures.

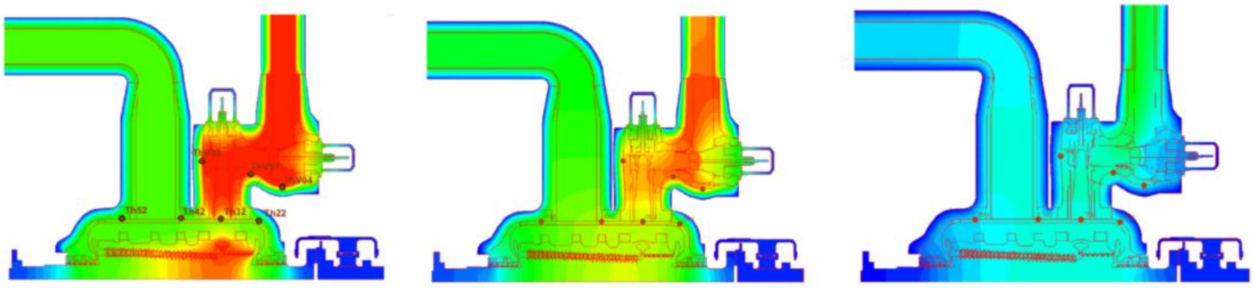

(i) *(ii)* *(iii)*

Figure 7: Alstom HP 460MW turbine temperature distribution (i) at base load (ii) 8hr (iii) 60hr after natural cooling start [15]

The concept of over-conductivity was validated through modelling of the natural cooling of an Alstom KA26-1 steam turbine, in which the turbine is modelled as a collection of solids in which the metal conductivity was a function of known metal behaviour, and the fluid being a solid of conduction given by the over-conductivity function [15]. Visual representations of the temperature progression through natural cooling is captured in Figure 7, above, in which the ability to capture the time variation of nodal temperatures and model temperature gradients is demonstrated [15], and in Figure 8, below, in which a close agreement of the calculated temperature to the measured temperature data during natural cooling for a particular nodal location, representative of a thermocouple location, is illustrated.

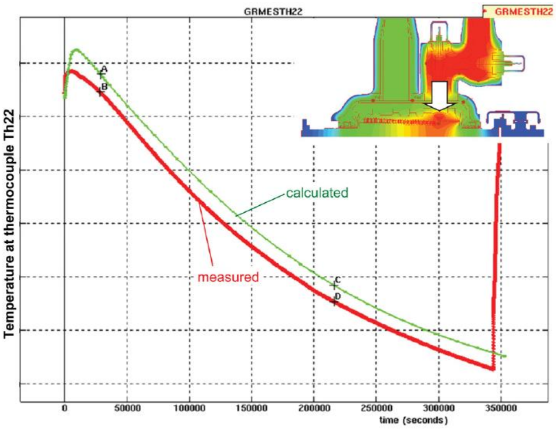

Figure 8: Calculated vs Measured Temperature variation during cool down [15]

It is worth noting that, despite the simplification of the fluid region providing closely agreeing temperature values, a limitation of the research conducted by Marinescu was the use of a two-dimensional FEM model to solve what is ultimately a three-dimensional problem. A 3D-2D equivalence is discussed by Marinescu and presents the ability of the model to maintain a reasonable simulation time by introducing a thickness scalar quantity to account for the mass discrepancies [14]. It was evident from the study that, given sufficient computational capacity, a three-dimensional model would be preferable and that such a model would capture the thermal behaviour to a greater degree. It would appear that in pursuit of increased modelling and simulation efficiency, a 2D model would be favoured when additionally paired with the simplification of over-conductivity.

However, 2D models have proved particularly successful in capturing temperature gradients in turbines during transient operations. In a study undertaken by Topel [16], a paired thermal model was presented. The model consisted of a thermodynamic steam expansion model, followed by a gland steam sealing model, both of which was generated using MATLAB software. These models were paired with a 2D FEM model of the geometries of the turbine selected in the study, using the COMSOL FEM software package [16].

As in the previous studies presented, the results of the thermal model were validated using operational data, with the objective of “predict(ing) metal temperatures and the associated thermo-mechanical properties within the turbine” [16]. Topel presents the importance of boundary conditions in the implementation of the model. He argues that it is important that the development of a thermal turbine model does not provide a direct reproduction of all of the intermediate boundary conditions [7], that boundaries are applied to the model, and for the outlet properties to be compared to the model results.

In Figure 9, below, it is evident that the boundary conditions are applied at the inlet side of each element of the model and are not a part of the model itself. This is an important observation in the context of model validation. In addition, the MATLAB program, written by Topel, allowed for the calculation of mass flow through the turbine chamber and labyrinth seals, as well as the temperature progression through these regions [16]. The FEM model simply applied these heat transfer boundary conditions to determine metal temperatures and temperature gradients in the surround metal components within the turbine.

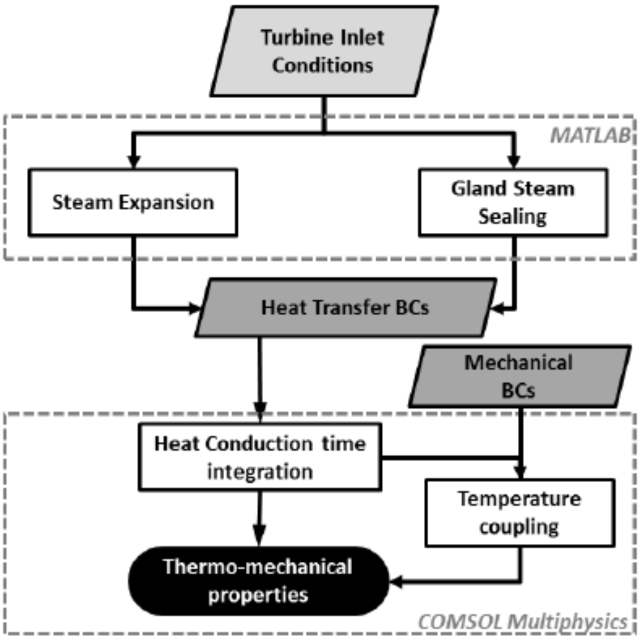

Figure 9: Thermal Turbine Model Developed by Topel [16]

Topel’s work demonstrated a 2D FEM model, and further tested modularity of turbine geometry and its validity when compared to continuous turbine geometry. This was motivated by a desire to have a versatile modelling methodology which could accommodate a large variety of turbine configurations with limited geometric data [16].

As in previous studies discussed above, steady state simulations were run first to ensure accuracy of the two model approaches, continuous vs modular, with results that suggest sufficient temperature gradients could be generated from a modular approach, as seen in Figure 10 below.

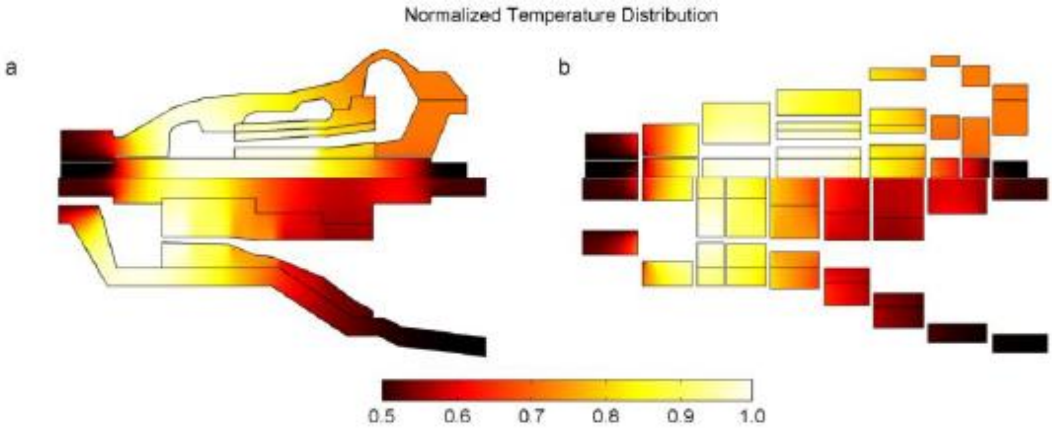

Figure 10: Continuous vs Modular Approach taken by Topel [16]

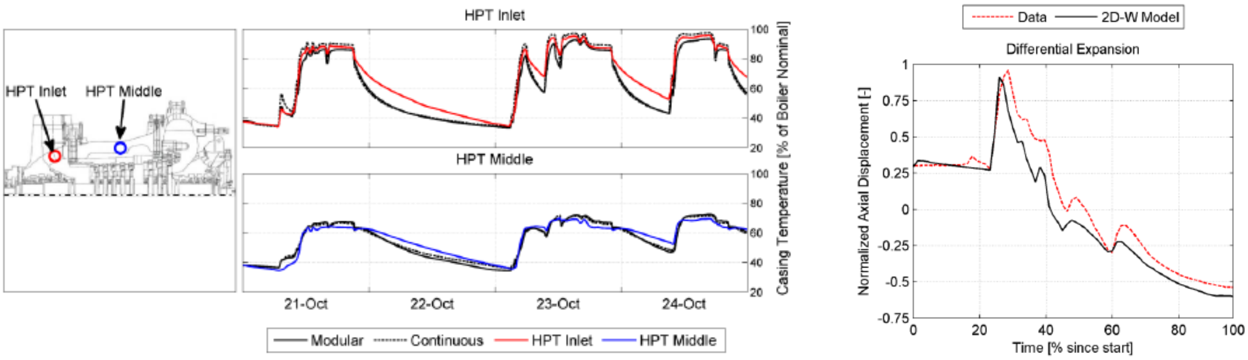

(i) *(ii)*

Figure 11: (i)Temperature Validation and (ii) Axial differential expansion during Transient Operation [16]

Transient simulations were performed, with validation presented as a function of internal temperature data extracted during operation, seen in Figure 11(i). Again, a continuous vs modular approach was analysed, with both presenting a good agreement with the continuous model appearing to replicate the temperature data more closely.

Topel further used the model to extract the predicted axial differential expansion, seen in Figure 11(ii), and investigated the effect that different turbine components had on displacement. It was found that it was more accurate to include three predominant components, inner and outer casings as well as the rotor [16], in thermal modelling that requires a prediction of a physical behaviour such as differential expansion. This complete approach is further confirmed by the work of Mukhopadhyay [13], in a study of shell deflection, as a function of thermal differential expansion of two halves of the outer turbine casing.

It is evident from the above studies that both two-dimensional and three-dimensional approaches have been used in the thermal modelling of steam turbines, however accuracy is better ensured through a three-dimensional approach. Given this approach, based upon the work of Topel [16], a paired thermal model was projected to overcome the fluid-to-solid challenges faced by Born and Marinescu, in which the thermodynamic considerations of the working fluid are considered by a computational tool such as MATLAB, the results of which are used as boundary conditions to a solid FEM model. The literature would suggest that the 3D modelling of the major components, rotor, inner and outer casing as well as seal cavities is vital for the successful prediction of differential expansion and thermal behaviour.

2.3 Turbine Nozzle Analogy

A methodology formulated by Fuls [1] visualises the stator and rotor passages as nozzles. The analogy describes a turbine stage as two nozzles, connected in series followed by a work extraction "bucket" used to represent the energy extraction for the turbine stage. The analogy stands for both reaction and impulse stages, with the ability of the latter to be modelled as a single nozzle followed by the work extraction stage, due to an assumption that the stator and rotor outlet pressure will be equal. Referring to the Mollier diagram for reaction and impulse stages in Figure 12, it is evident that the static pressure does remain constant across the rotor.

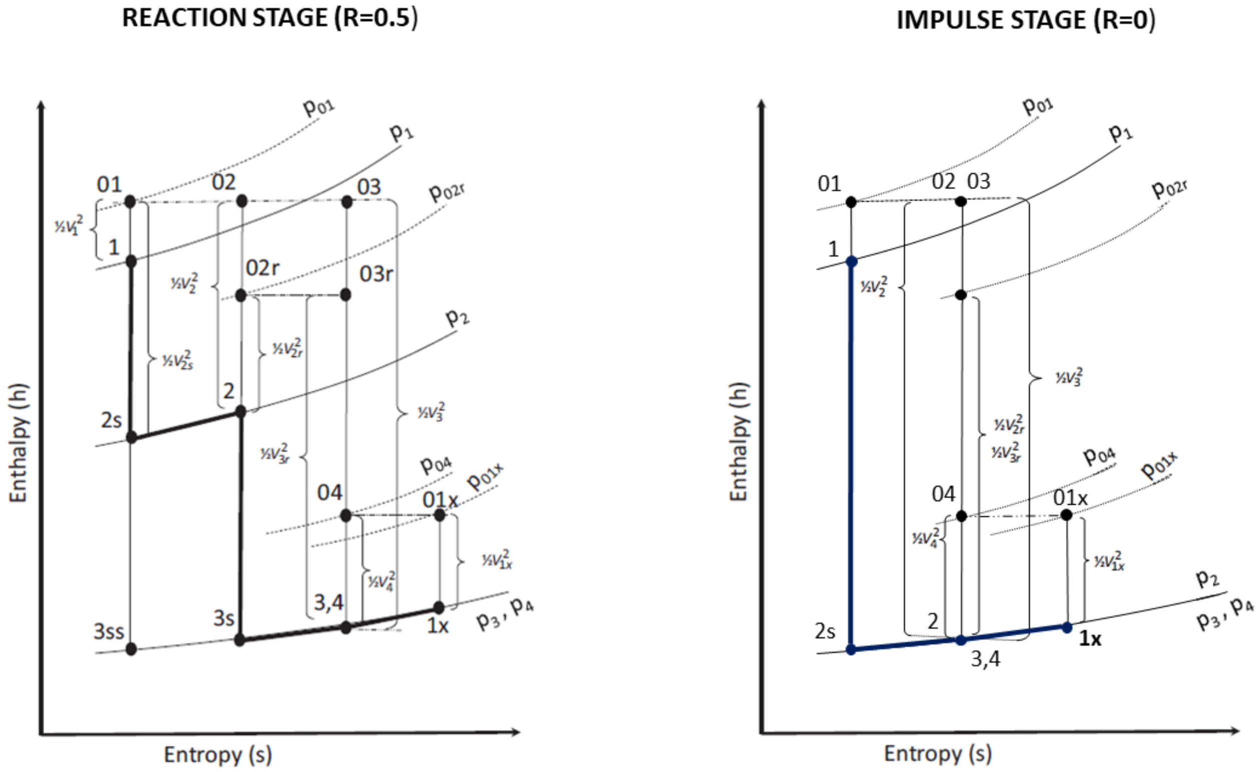

Figure 12: Mollier diagrams for reaction and impulse turbine stages

As was suggested in the review of turbine thermal modelling methodologies, such 1D approximations prove powerful in reducing the computational cost of simulating the stage-by-stage progression of thermal properties through the turbine. The power of the method by Fuls is the ability to model the stage-by-stage behaviours of turbines with minimal geometric data [1]. An integrated turbine stage component was created by Fuls et al. [2] using Flownex SE. The component adopted the nozzles connected in series with a pipe of variable diameter to represent the carry over losses of each stage. Figure 13, shows a detailed view of the developed component, which was applied to the multistage model developed in this project.

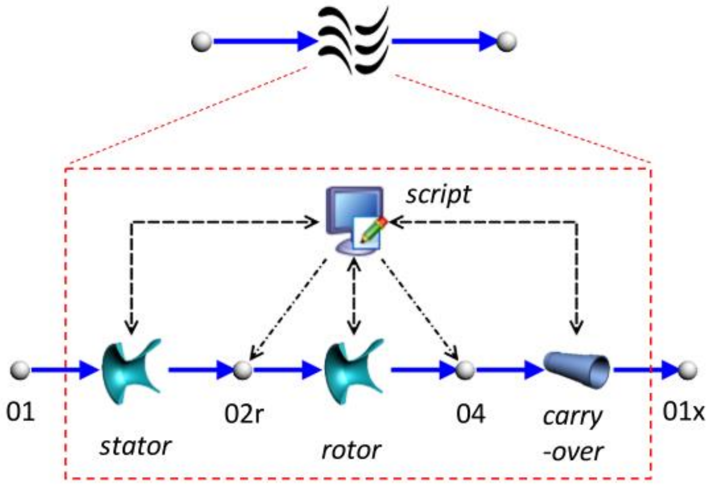

Figure 13: Turbine stage component [2]

From plant data, the enthalpy drop can be estimated across the entire unit and given the known number of stages, the enthalpy drop across each stage can also be calculated isentropically. Fuls considers first the stationary, stator stage and derives the isentropic exit velocity (v_2), with reference to the abridged Mollier Diagram in Figure 14 and assuming a relatively small stage inlet velocity (v_1) as follows:

$$v_2 = \sqrt{2 \cdot (h_1 - h_2)} = \sqrt{2 \cdot \Delta h_S} \tag{2.1}$$

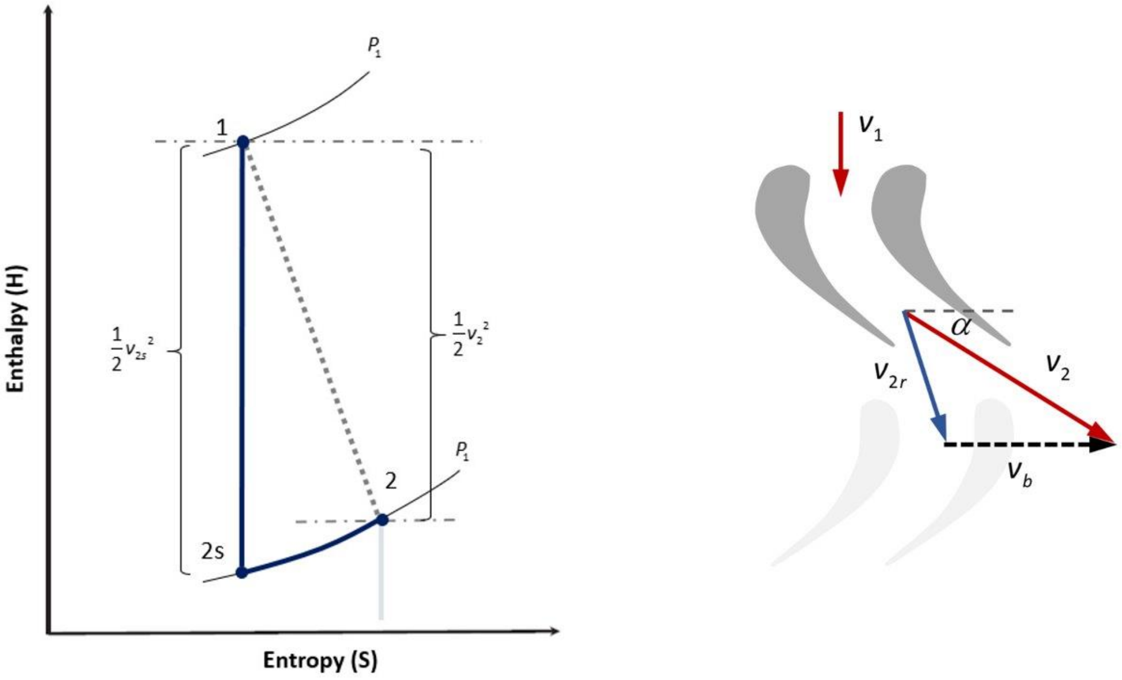

Figure 14: Stator Enthalpy-Velocity relationship and Velocity Triangle

The analogy also captures "irreversibilities" [1] in the form of an enthalpy loss coefficient (ζ) such that the absolute stator exit velocity is given by:

$$v_2 = \sqrt{\eta_s} \cdot v_{2s} \tag{2.2}$$

Where $\eta_s = \frac{1}{1-\zeta}$

An ideal assumption can be made during the nozzle sizing exercise, thus making $v_2 = v_{2s}$ and simplifying the initial sizing of the nozzle areas.

In order to calculate the nozzle area of the rotor stage, first the velocity triangle of the stator exit must be considered in order to solve for the relative inlet rotor velocity (v_{2r}). From Figure 14, the Cosine Rule is derived:

$$v_{2r} = \sqrt{{v_b}^2 + {v_2}^2 - 2 \cdot v_b \cdot v_2 \cdot \cos\alpha} \tag{2.3}$$

Considering the Mollier diagram, in Figure 15, for the rotor stage, one is able to derive the equation for the relative rotor exit velocity (v_{3r}) as a function of the isentropic enthalpy drop (Δh_s) and the relative stator exit velocity (v_{2r})

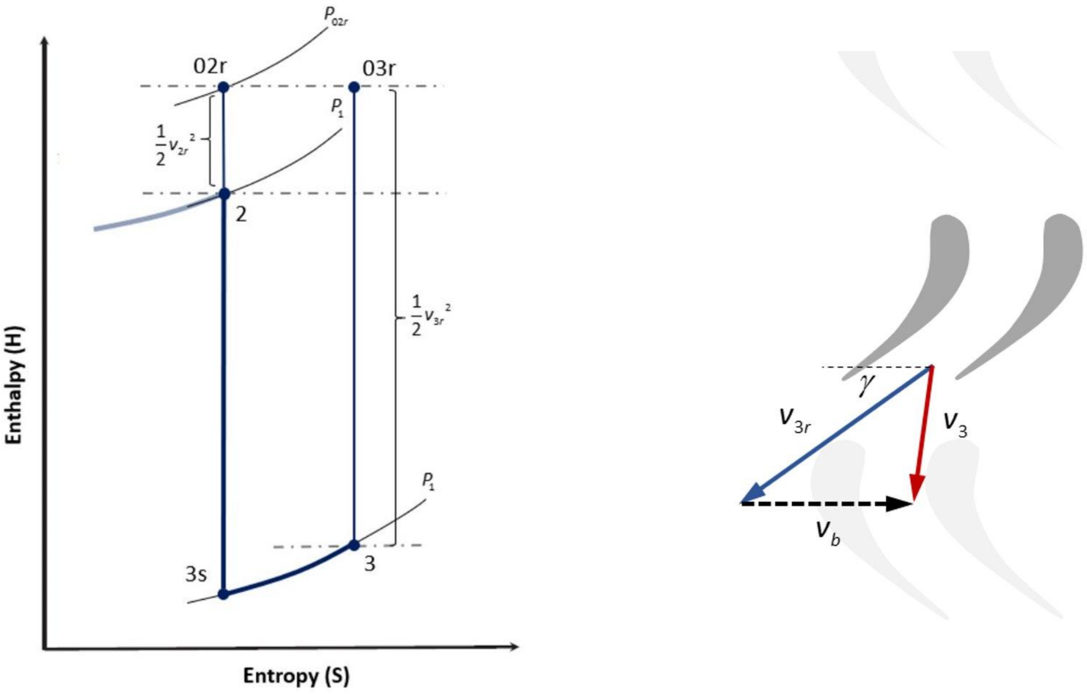

Figure 15: Mollier Diagram for Rotor Stage

From the Mollier diagram, one can derive the isentropic enthalpy drop across the rotor (R) as being equal to:

$$\Delta h_R = \frac{1}{2} v_{3r} - \frac{1}{2} v_{2r} \qquad 2.4$$

Therefore, the relative rotor exit velocity:

$$v_{3r} = \sqrt{2 \cdot \Delta h_R + {v_{2r}}^2} \qquad 2.5$$

Thus, giving the enthalpy at the rotor outlet, prior to work extraction, as the following:

$$h_3 = h_{02r} - \frac{1}{2} \cdot {v_{3r}}^2 \qquad 2.6$$

Fuls proceeds in completing the exit condition of the turbine stage as well as the remaining kinetic energy carried over to the next stage [2]. In this study, having calculated the relative and absolute velocities of both the stator and rotor it is possible to size a representative nozzle area using the mass flow equation:

$$\dot{m} = \rho A_N v_N \qquad 2.7$$

Where v_N is the velocity through the nozzle: v_2 for the stator and v_{3r} for the rotor, and ρ being the exit density of the steam at the stator or rotor exit.

2.4 Flownex SE

Flownex Simulation Environment (SE) is a software package which allows one to model thermodynamic, thermo-fluid and heat transfer applications. The capacity for Flownex SE to develop 1D dimensional system models, whilst maintaining conservation of mass and momentum equations, was of fundamental importance to the software's selection in this project. Additionally, with the desire to model two-phase steam flow, the ability of Flownex SE to accurately capture two-phase phenomenon made it a natural choice in the 1D Turbine Model development.

Flownex SE features an extensive library of heat transfer and fluid flow components allowing for the capturing of turbine component interaction with steam flows. The ability to use built-in scripting components to perform integrated calculations as well as executing the import and export of externally sourced data sets, allowing for the computationally inexpensive 1D modelling of the entire turbine operation.

The interface of Flownex SE is graphical, as seen in Figure 16, which allows for the user to drag and drop different system components into a representative 2-dimensional space.

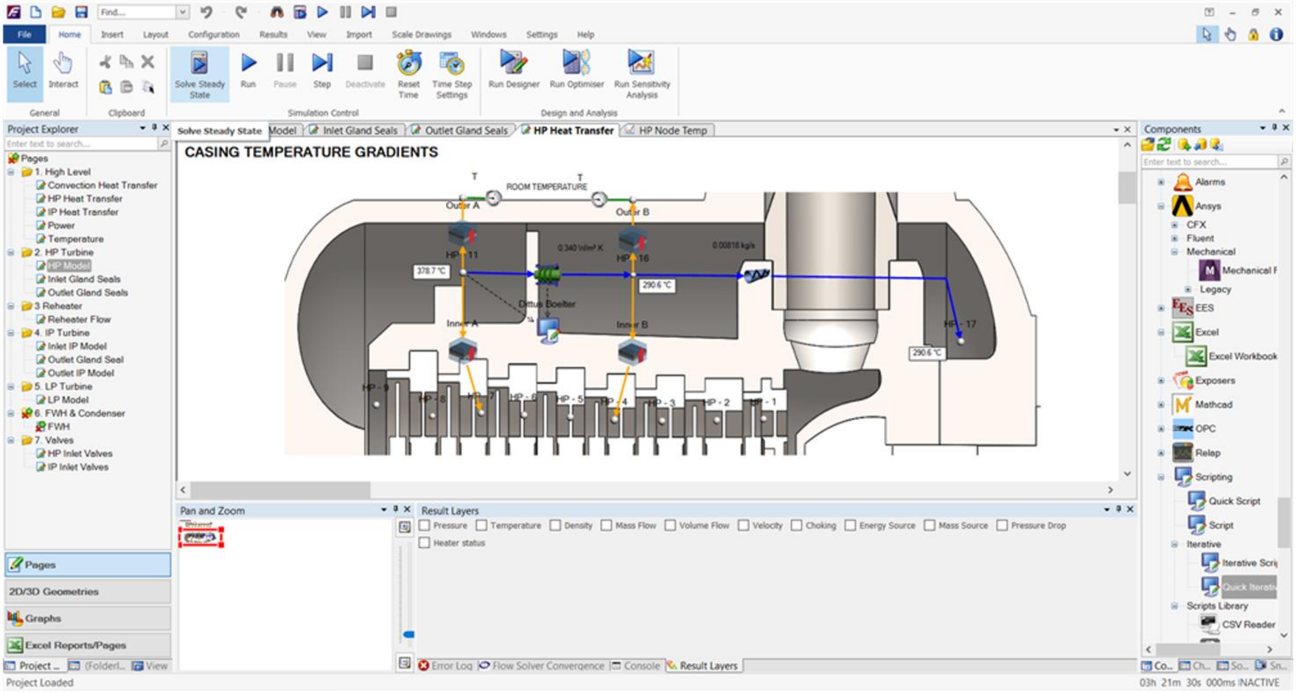

Figure 16: Flownex SE Graphical Interface

The use of Flownex SE enables one to simplify the entire turbine operation into a representative process model of both high detail, as seen in the multistage turbine models, and low details, as seen in the developed process models. A benefit of using modelling software like Flownex SE is the ability to perform off-design simulations with real-time calculation of efficiencies and losses which would be present in the actual turbine system.

This section of the report will detail the various components used within the 1D turbine model and the governing equations for these components.

2.4.1 Flow Resistance component

In order to undertake the modelling of a complex steam turbine, the modelling of steam flow paths and piping are important. A Flow Resistance component is available to use in modelling the flow and subsequent pressure drops of steam through regions of limited or unknown geometry.

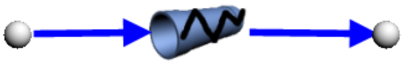

Figure 17: Flow resistance component

The implementation of this component is valid based on the assumption of Dimensional flow and that no work is done on or by the fluid except that of flow work [17]. The pressure drop across the element is given by Equation 2.8

$$\Delta p_0 = \frac{|\dot{m}|\dot{m}}{A_f \cdot A_{sf} \cdot A_o} + \rho g \Delta z \qquad 2.8$$

Where

A_f - Flow admittance (kg/m)
A_o - Geometric opening area (m^2)
A_{sf} - Admittance scaling factor (Unitless)
Δz - Change in pipe elevation (m)

Given the turbulent flow and constant density expected within the transporting pipes of the turbine unit, it is appropriate to model the flow resistors as exhibiting quadratic resistance behaviour. The quadratic behaviour is given by Equation 2.9.

$$\frac{1}{A_f \cdot A_{sf} \cdot A_o} = \frac{1}{2} \cdot \left(\frac{fL}{D} \right) \cdot \frac{1}{A^2} \qquad 2.9$$

Where

f - Friction factor
D - Inner pipe diameter
L - Pipe Length

The capabilities of the flow resistor component also features other resistance behaviours such as linear behaviour, for laminar applications, and square root behaviour, for the pressure drop through a valve [17]. It is possible to reduce the pressure drop to an approximately zero value through the selection of a significantly large flow admittance value (A_f). With a high flow admittance, the component simply acts as a flow connector within the 1D turbine model, which is useful for regions that can be assumed not to play any pressure loss role. The use of a flow resistor with high flow admittance ensures that the model can be calibrated easily, as calibration would only need to be focused on components of significant pressure drops (i.e. turbine stage components, reheaters and valves)

2.4.2 Gland Seals

The turbine gland seals were modelled using the Labyrinth Seal component. The seal features the options for an axial straight, axial staggered and radial labyrinth seal [17].

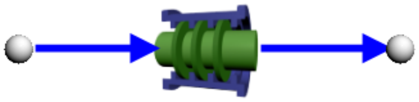

Figure 18: Labyrinth Seal component

Of most relevance to the modelling of turbine gland seals is the use of axial staggered labyrinth seals. Figure 19, features the geometric values used to define the labyrinth seal, which would be interpreted from the available turbine data.

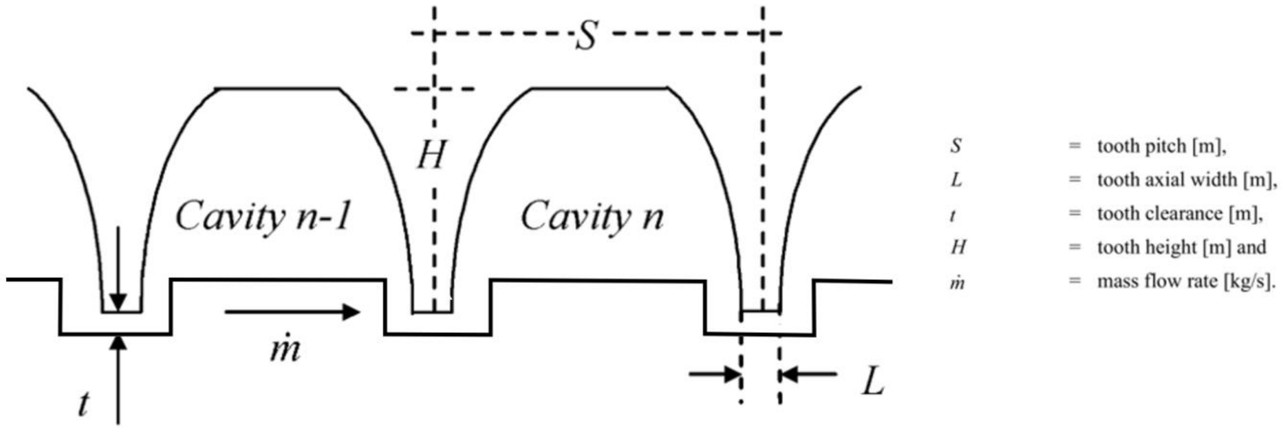

Figure 19: Labyrinth Seal Geometric Quantities [17]

The labyrinth seal provides a discretised and single element modelling methodology, with the discretised model being solved on a tooth-by-tooth basis and the single element considering the labyrinth seal as a singular entity [17]. The single element model appears sufficient in modelling the pressure drop across the entire seal as opposed to a distribution, which is beyond the scope of this study. Considering the labyrinth seal component as a single element. The governing mass flow equations used in the single element model is given by Equation 2.10. [17]

$$\dot{m} = (C_d A)\cdot C_{ke}\cdot \frac{p_{01}}{\sqrt{RT_{01}}}\cdot\sqrt{\frac{1-\left({}^{p_{02}}\!/\!_{p_{01}}\right)^2}{z-\frac{2}{\gamma}\ln\left({}^{p_{02}}\!/\!_{p_{01}}\right)}} \qquad 2.10$$

The inlet steam conditions to the seal are denoted by (T_{01}, p_{01}) and the exit pressure is denoted by p_{02} . Given the use of a staggered axial seal , a total kinetic energy transfer assumption is made such that $C_{ke} = 0$ [17], where C_{ke} is the kinetic energy carry-over coefficient. The discharge coefficient (C_d) for compressible flow through the single element model is user defined and can be used to model the expected pressure drops across the turbine seals. This would be the value to calibrate during model setup.

2.4.3 Heat Transfer Components

In the work of Topel [16], when modelling the transient operation of steam turbines in a two-dimensional sense, a “thickness” parameter was used to ensure the capturing of thermal inertia within the model [16]. Topel correctly states that the transient temperature gradients observed during a start-up procedure is a function of the overall thickness [16] or mass of the turbine components. In this study, given the desire to model transient thermal behaviour of steam turbine components, it was necessary to capture the thermal mass contribution of the major turbine components. Flownex SE features a Composite Heat Transfer Component.

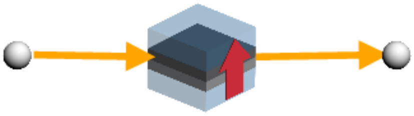

Figure 20: Composite Heat Transfer component

This component allows the user to define a convective boundary on the outer surface of the defined volume and model the subsequent conduction heat transfer through the volume.

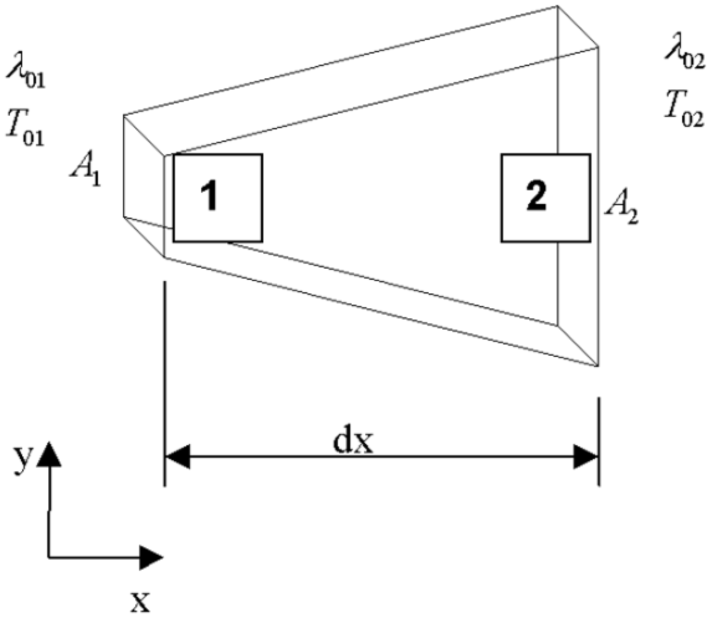

Figure 21: Composite Heat Transfer component volume, adopted from [17]

Considering the conservation of energy, as shown in Equation 2.11, the heat transfer of the considered volume (V) can be captured through the composite heat transfer component.

$$\frac{\partial\left(\rho V c_p T_0\right)}{\partial t}=\sum\left(\dot{Q}_{conv}+\dot{Q}_{cond}+\dot{Q}_{rad}\right)_{in}-\sum\left(\dot{Q}_{conv}+\dot{Q}_{cond}+\dot{Q}_{rad}\right)_{out}+\sum S_d \quad 2.11$$

The component allows for the capturing of three heat transfer methods, convective, conductive and radiation heat transfer. Each heat transfer is solved using the first principle characteristic equations.

For the conductive heat transfer terms, the user can defines one's own or select the appropriate material from a built-in library to define the conductive heat transfer coefficient (k).

For considering the convective terms, similarly, the user is able to define the convective coefficients (λ_{01} and λ_{02}) or utilise a built-in Dittus-Boelter Correlation if particular coefficients are needed [17].

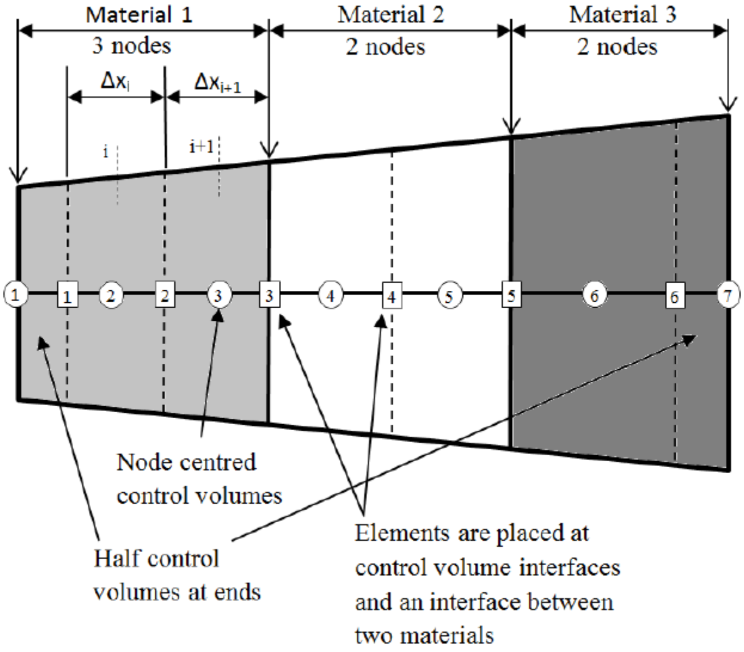

Figure 22: Discretised, composite material heat transfer model [17]

The composite heat transfer component allows for the modelling of a component which features multiple material compositions along its length (dx). One can also further discretise the material volume to more accurately capture the temperature gradients through the material as shown in Figure 22, above.

Whilst temperature gradients can also be captured in FEM models, undertaking this modelling is important, particularly in the transient modelling, as the heat transfer between fluid and material impacts the computed temperature changes to the steam itself. The Composite Heat Transfer component can account for the transient change in energy transfer between the working fluid and material through the following energy balance.

The node volume (V) is calculated as half of the solid element connected to the node [17]. The Sources Term (S_d), representative of the internal heat generation within the solid, was not applicable to the steam turbine application. Whilst Flownex SE has the ability to perform a fully discretised heat transfer analysis, similar to that performed by ANSYS, such an analysis would involve significantly more modelling effort. Additionally, the turbine components, whilst symmetrical, are complex in nature and thus difficult to simulate easily in the Flownex SE environment. The purpose of the heat transfer elements is to rather capture the interaction between solid component volumes and the surrounding steam during transients, which is explored in greater detail in later chapters.

2.4.4 Custom developed Rankine Cycle components

One very powerful feature of Flownex SE is the ability to develop one's own custom "compound components" that are made up of normal components as well as scripting features. Since Flownex is a general thermo-fluid network solver tool, does not contain a wide variety of Rankine cycle components. The ATProM research group has developed over time various compound components to simplify the modelling of a complete Rankine system, shown in Figure 23.

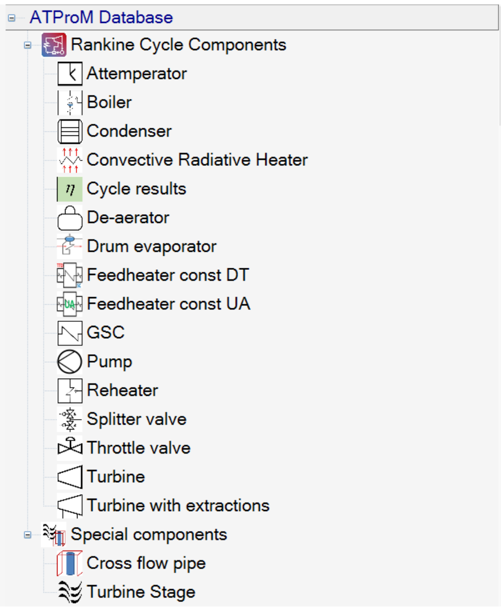

- ATProM Database
  - Rankine Cycle Components
    - Attemperator
    - Boiler
    - Condenser
    - Convective Radiative Heater
    - Cycle results
    - De-aerator
    - Drum evaporator
    - Feedheater const DT
    - Feedheater const UA
    - GSC
    - Pump
    - Reheater
    - Splitter valve
    - Throttle valve
    - Turbine
    - Turbine with extractions
  - Special components
    - Cross flow pipe
    - Turbine Stage

Figure 23: ATProM research group component library

The components emulate the behaviour found in other process modelling tools where the user is required to provide the design base operating point, which is then internally converted into the correct component parameters such that the off-design behaviour is accurately described. The specific underlying theory for these components will be expounded later where their use is shown.

2.5 ANSYS Mechanical

ANSYS Mechanical is a Finite Element Modelling (FEM) software package allowing one to perform 2-dimensional and 3-dimensional Finite Element Analysis (FEA). The use of a robust FEA package, as documented in Topel [16] and Marinescu et al. [14], is fundamental to the accurate modelling of steam turbine operation and as such was also implemented in this study.

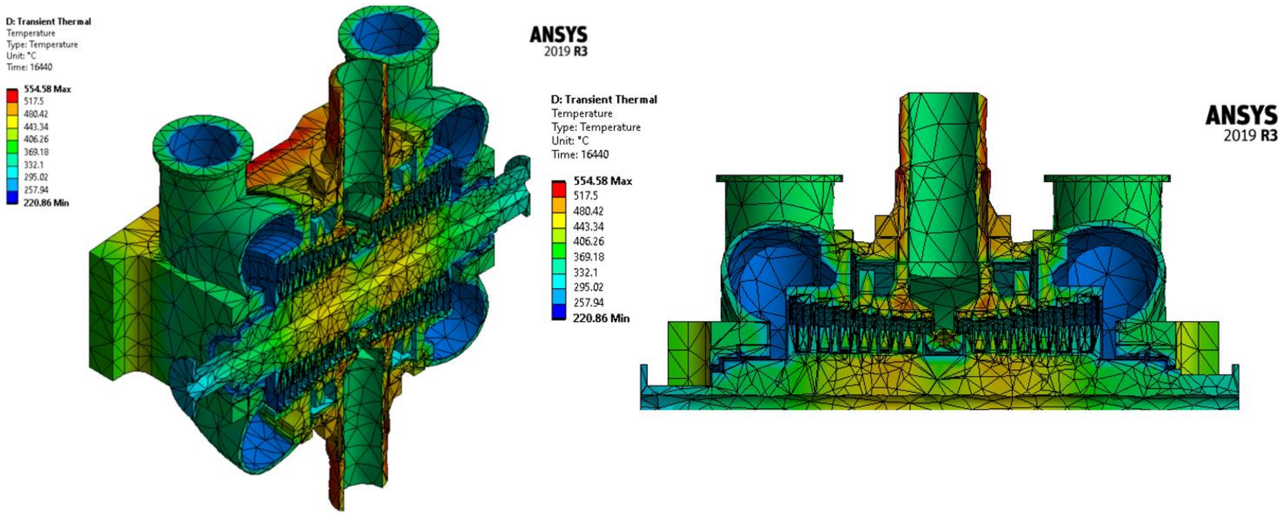

Figure 24: 3-dimensional FEA model of the Intermediate Pressure Turbine

ANSYS Mechanical is a commercial software package which enables the establishment and solving of thermal and structural matrices within a discretised volumetric mesh. The objective of this study was the analysis of both heat transfer and subsequent thermal deformation arising from the varying sizes of turbine components. This section will examine, firstly, the establishment of these thermal matrices, providing the justification for the boundary definitions chosen in this study. Secondly the structural governing equation used within the model will be examined. Looking first at the thermal matrix, of importance is the establishment of the conductive and convective matrices as a result of the thermal boundaries applied to the turbine models. Figure 25 presents a representative volume

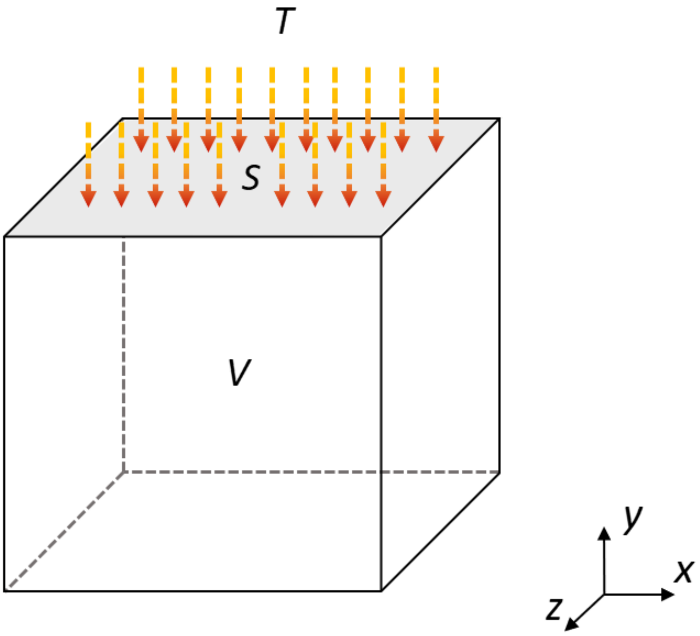

Figure 25: Heat flux from an external boundary temperature T through surface S or volume V

Given this representative volume the first law of thermodynamics is as follows:

$$\rho c\left(\frac{\partial T}{\partial t}+\{v\}^{\mathrm{T}}\{N\}T\right)+\{N\}^{\mathrm{T}}\{q\}=\ddot{q}+S \qquad 2.12$$

Where

$\{v\}$ - Velocity vector

$\{N\}$ - Vector operator

$\{q\}$ - Heat flux vector

$\ddot{q}$ - Heat generation rate per unit volume

In relation to Figure 25, the velocity vector would describe the vertical transfer of heat in the negative y-direction. Equation 2.12 constitutes the governing equation for each discretised volume, with the choice of the outer surface boundary condition affecting this governing equation as follows:

Surface Temperature boundary

Specifying a user-defined surface temperature leads to the following adjustment to Equation 2.13

$$T=T^{*} \qquad 2.13$$

where

T^{*} - Specified Temperature

The surface temperature boundary condition constitutes the simplest thermal boundary condition as it forces the outer surface to be the specified temperature at a given time step.

Convective Surface Boundary

The convective boundary condition constitutes a more complex boundary in solving Equation 2.12 in which Newton's law of cooling [18] is used.

The following equation is used for the convective boundary condition:

$$\{q\}^{\mathrm{T}}\{\eta\} = h_f\left(T_s - T_B\right) \tag{2.14}$$

Where

$\{\eta\}$ - Normal vector

h_f - Film convective coefficient

T_S - Model surface temperature

T_B - Bulk fluid temperature

Considering the surface boundary condition (S), Equation 2.12 can be written in integral form of the total energy balance, with simplification, through the representative volume as follows

$$\int_V \left[\rho c\left(\frac{\partial T}{\partial t} + \{v\}^{\mathrm{T}}\{N\}T\right) + \{N\}^{\mathrm{T}}\{q\}\right]\cdot dv = \int_S h_f\left(T_s - T_B\right)\cdot dS \tag{2.15}$$

This ability to apply various external temperature boundaries speaks to the capability of ANSYS Mechanical and the tools available in modelling complex systems as this system of equations is solved for each discretised element of the full 3-dimensional turbine. The choice of thermal boundary conditions will be explored in later chapters of this study in such a way as to be computational inexpensive.

Considering the structural response as a result of the thermal and structural loads applied to the turbine model one must consider the establishment of the total nodal strain vector below:

$$\{\varepsilon\} = \left\{\varepsilon^{th}\right\} + [D]^{-1}\{\sigma\} \tag{2.16}$$

Where

$\{\varepsilon\}$ - Total strain vector

$\{\varepsilon^{th}\}$ - Thermal strain vector

$[D]^{-1}$ - Inverse elastic stiffness matrix

$\{\sigma\}$ - Total stress vector

Within the turbine FEA model formulated in this study, the general material stresses in major turbine components were well described. The model sought to capture the overall volume of each turbine component as accurately as possible given the limited OEM data available. As a result, even though localised stress concentrations were likely not calculated in the model the derived global stiffness matrix was sufficiently captured. Due to the reasonably well-defined global stiffness matrix, it can be concluded that the overall deformative response was accurate and more than sufficient in predicting turbine component deformation. The performance of the model, and accompanying stiffness matrix was validated in later chapters of the study.

The thermal strain vector was fundamental to the turbine model, as the thermal loads are the primary focus of this study. The thermal strain vector is defined as such

$$\{\varepsilon^{th}\} = \Delta T \begin{bmatrix} \alpha_x & \alpha_y & \alpha_z & 0 & 0 & 0 \end{bmatrix}^{\mathrm{T}} \tag{2.17}$$

where

$\alpha_{x/y/z}$ - thermal expansion coefficient in the x, y and z direction

The structural response of the body is defined in the following general equation

$$[K_e]\{u\} - \{F_e^{th}\} = [M_e]\{\ddot{u}\} + \{F_e^{nd}\} \tag{2.18}$$

where

$[K_e]$ - Element stiffness matrix

$\{u\}$ - Displacement

$\{F_e^{th}\}$ - Element thermal load vector

$[M_e]$ - Element mass matrix

$\{\ddot{u}\}$ - Acceration vector (incld. gravity effects)

$\{F_e^{nd}\}$ - Nodal force vector of element

The nodal force vector is a vector which accounts for the external constraints applied to the model and is solved iteratively through the above general equation. It is evident from the general equations for both the thermal and structural response equations that the software is able to account for a variety of boundary conditions at each node within the FEA model. It is evident, particularly from the thermal load equations that the selection of the type of boundary conditions impacts the computational expense of the model and had to be considered during the implementation of the model in later chapters of this report. The complexity of these equations also speaks to the need to optimise the number of nodes used to capture both the HP and IP models, thus providing the motivation for the mesh independence study documented in later chapters.

The use of commercial FEA software, ANSYS Mechanical, in this study allowed investigators to interactively apply the representative thermal and structural boundary conditions, without the need to develop one's own FEA code.

3. Data Collection

3.1 Candidate Turbine Selection

In order to test the modelling methodology, a candidate unit had to be selected. It is known that turbines differ greatly based on manufacturer, application, and power output, and these, in turn, impact turbine geometry. The selection of a specific candidate unit will serve as a source of validation data for the eventual paired turbine model. For the purposes of this study, a candidate turbine was identified from within the Eskom turbine fleet. The initial criteria for this turbine were the following:

- Susceptibility to differential expansion and evidence of interference in turbine components, observable during maintenance inspections
- Significant and trustworthy technical data and process information available
- Additionally, a good communication link with site engineers to gain access to operational information pertaining to the candidate unit
- Reasonable similarities to other power plant turbines used within Eskom

For the purposes of confidentiality, the name of the selected Eskom Power Station is excluded from the body of this report and will henceforth be referred to as "the candidate turbine". A horizontal, disc and diaphragm closed-coupled single reheat four-cylinder turbine was selected from the current Eskom coal-fired power plant fleet, as shown below.

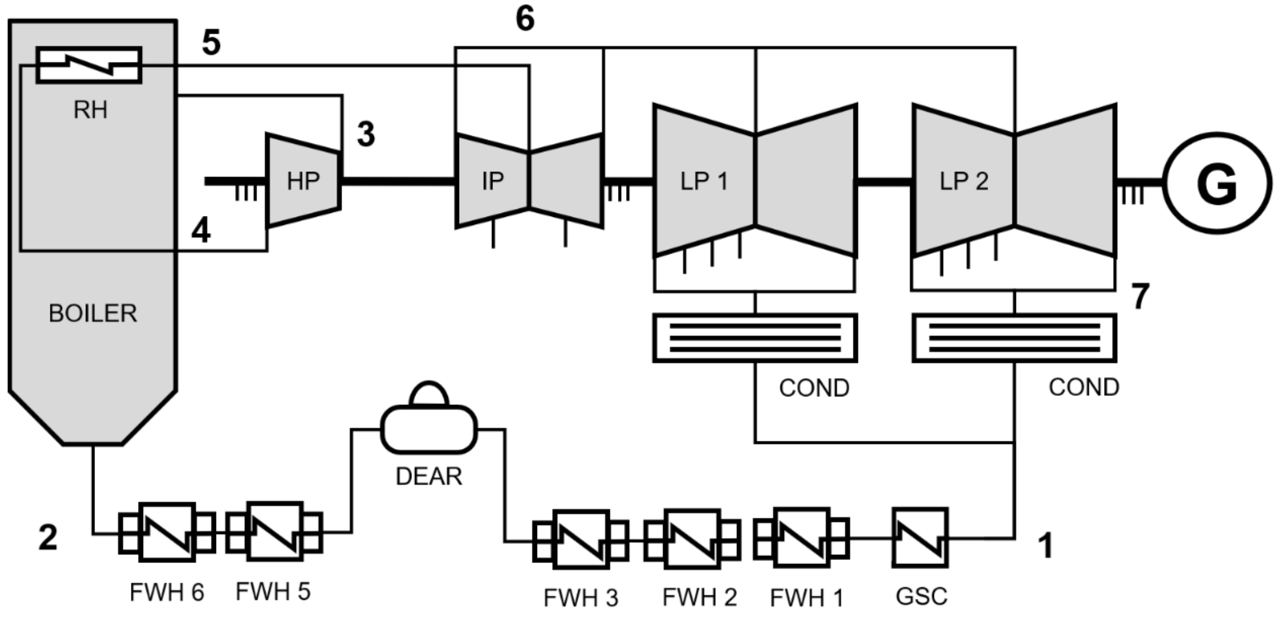

Figure 26: Process Flow Diagram of Candidate Turbine

The candidate turbine system produces 600MW of power using a high, intermediate and two low pressure turbines, using a Regenerative Rankine cycle with Reheat, as seen in the T-S diagram in Figure 27.

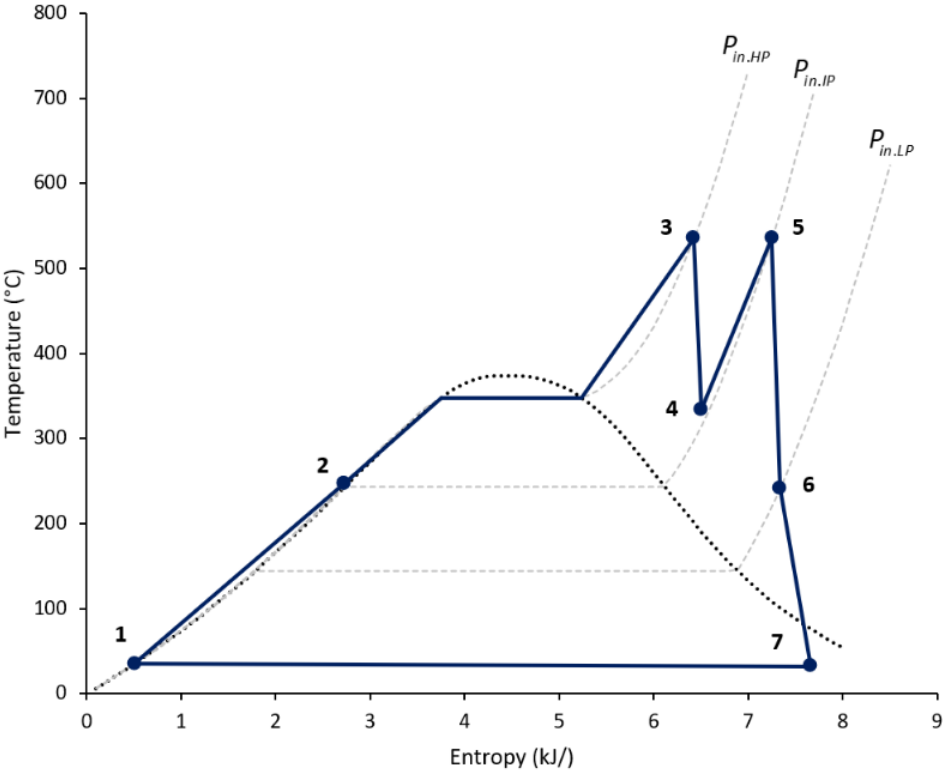

Figure 27: Rankine Cycle of Candidate Power Plant

The primary focus of this study was centred on the stage-by-stage modelling of the high pressure (HP) turbine, found between point 3-4 in Figure 27, and the intermediate pressure (IP) turbine, similarly found between point 5-6. Focus was placed on the HP and IP turbines due to the main steam flow paths of both units. The HP turbine featured a single main steam flow from the rear to the front of the unit, and the IP turbine featured a split flow progressing from the central inlet pipe.

Given that the modelling methodology would be similar in both the IP and LP units, and given the similar steam flow paths, a decision was taken to not perform detailed modelling of the LP turbine. In addition to this, from preliminary site investigations it appeared that the HP and IP units showed the most signs of component interference.

Evidence of component interference was observed on a site visit to the candidate unit, during a scheduled shut down. During this site visit, it was observed that the interstage glands on both the HP and IP units showed signs of interference, characterised by Figure 28, where the interference of the interstage glands and the IP rotor has caused the exposure of new metal on the rotor's surface. Figure 29 illustrates the interference along the outer radius of the stage diaphragm seals such that the thin glands have buckled as a result of the interference.

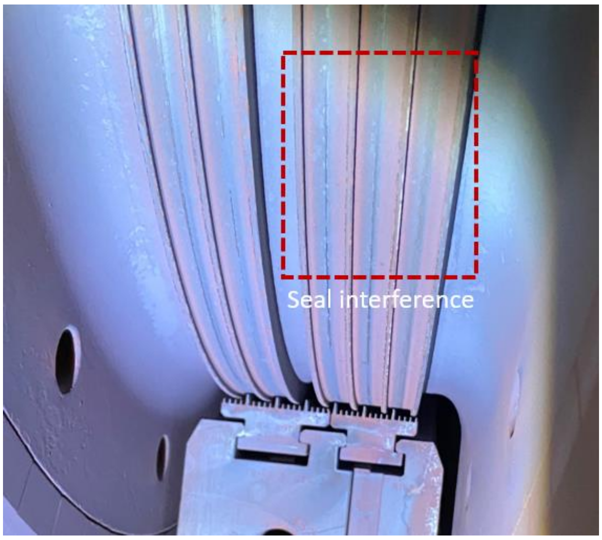

Figure 28: Evidence of metal-to-metal rubbing during site visit

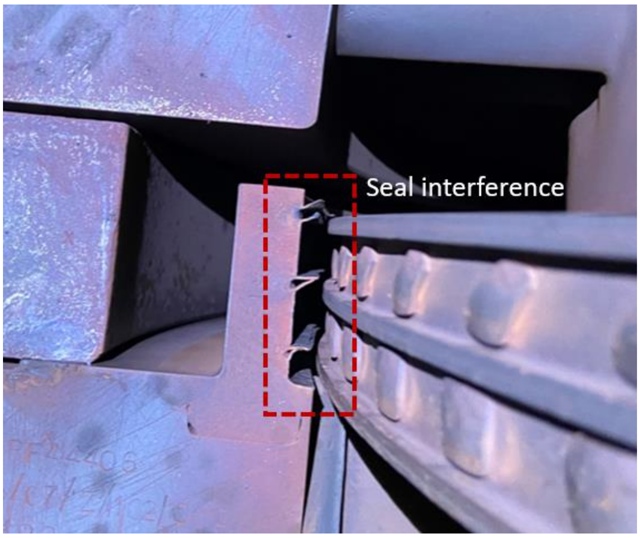

Figure 29: Evidence of radial interference between diaphragm and inner casing

It was clear from site visit observations and on-site accounts that it was the radial clearances between rotor and stator as well as the interstage flow paths that were of particular interest in this study. As such the methodology described in this study sought to nominally model the clearance behaviours at these locations through the HP and IP units.

From the candidate unit, various documentation and site data were collected as follows:

- Original Heat Balance Diagrams: detailing the designed process information for the 100%, 80%, 60% and 45% load cases
- Sectioned and Isometric Turbine diagrams: aiding in the 3D modelling of the HP and IP units
- Recorded plant data: for validation of the eventual model with the following focuses
    - **Process data**, such as superheater temperature and pressure as well as main steam mass flow, used as boundary conditions to the 1D turbine model.
    - **Thermocouple readings**
    - **Differential Expansion readings**
- Clearance measurement report during a recent rotor inspection.

The collection of this data fell under the non-disclosure agreements signed at the start of the study and constituted the probable information available to site engineers operating a steam turbine unit, akin to the candidate unit, and constituting minimal OEM input. No detail blade geometry data was obtained, and only very few reference dimensions were taken to verify the relative scale of components visible in the layout drawings.

3.2 Start-Up Procedures

The start-up procedures of steam turbine units are classified into three categories: cold, warm and hot start-ups [19]. The categorisation of these start-ups is most commonly a function of HP inner metal temperatures as well as the time that the unit has spent in "standstill" [19]. The inner metal temperatures also indicate milestones within the start-up procedure itself. In the candidate unit used in this study, operators prescribe a given start-up from the HP inner metal temperature as well as standstill time as shown in Table 1.

Table 1: Turbine Start-up Categorisation

Category	HP Inner Metal Temperatures (°C) - $T_{HP.cyl}$	Standstill Time (hrs)
Very Cold *	$T_{HP.cyl} < 160$	
Cold	$160 < T_{HP.cyl} < 320$	> 65
Warm	$320 < T_{HP.cyl} < 390$	8 - 65
Hot	$390 < T_{HP.cyl}$	0 - 8

**- Eskom prescribed condition.*

During the data collection phase of this study, an additional categorisation of a "very cold" condition is featured to capture the start-up procedure following an extended standstill, such as in the case of extensive maintenance. During the start-up procedure, operators monitor the "mismatch" or temperature difference between the main steam and average inner metal temperatures. This is to ensure that no dramatic temperature differences are created in the metal during start-up, which could lead to differential expansion leading to possible component interference [19].

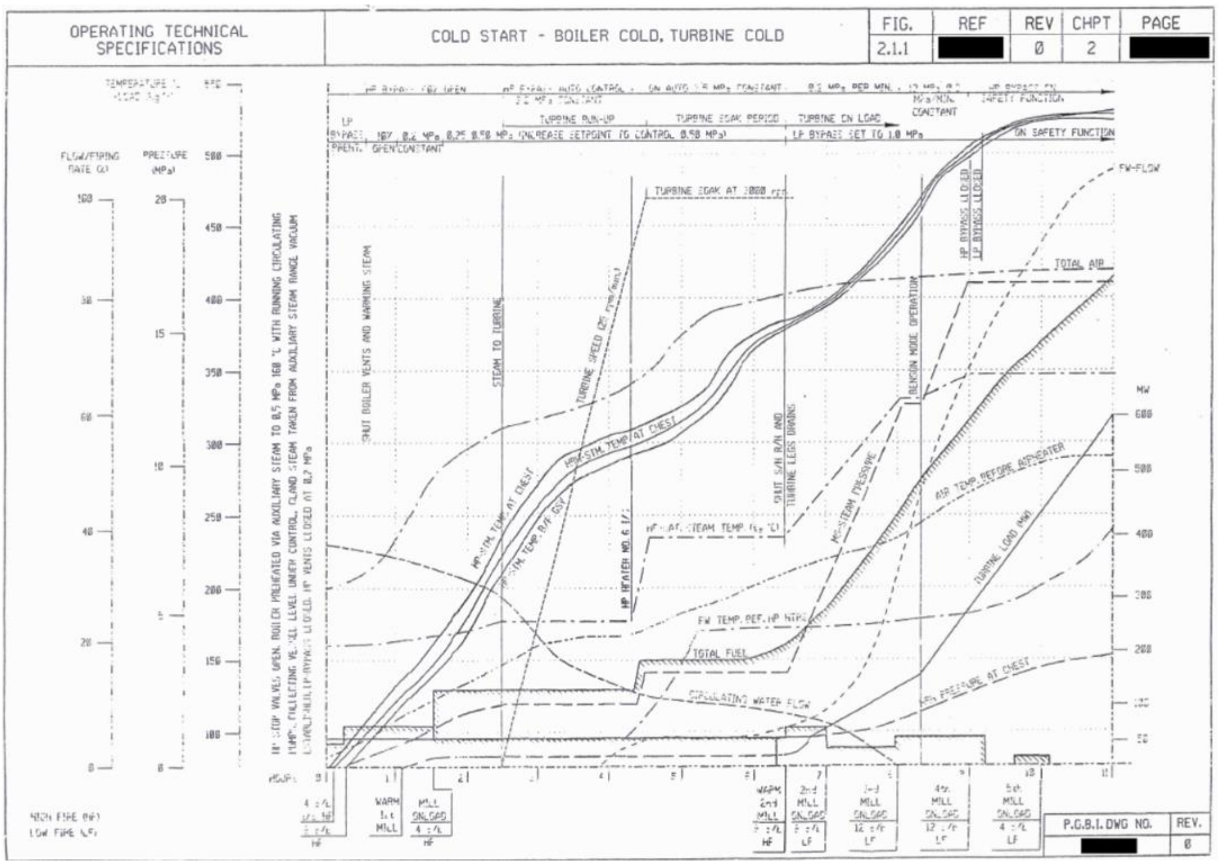

Figure 30: Theoretical Cold Start-up sequence for candidate unit (reduced quality for confidentiality purpose)

The start-up procedure is documented in detail for operators, but is also represented in graphical form in unit manuals (as shown in Figure 30) as a representation of the ideal start-up process. The diagram demonstrates the gradual increase in inlet pressure and temperature over the course of the start-up and the relevant ramp ups of rotor speed at designated points. For this study, reported data were collected from the candidate unit for a recent Cold Start-Up. The access to reported parameters such as inlet steam pressure and temperature, total boiler mass flow and rotor speed allowed for the establishment of a representative cold start-up sequence which could be used as boundary conditions to the 1D turbine model. The representative start-up is shown in Figure 31.

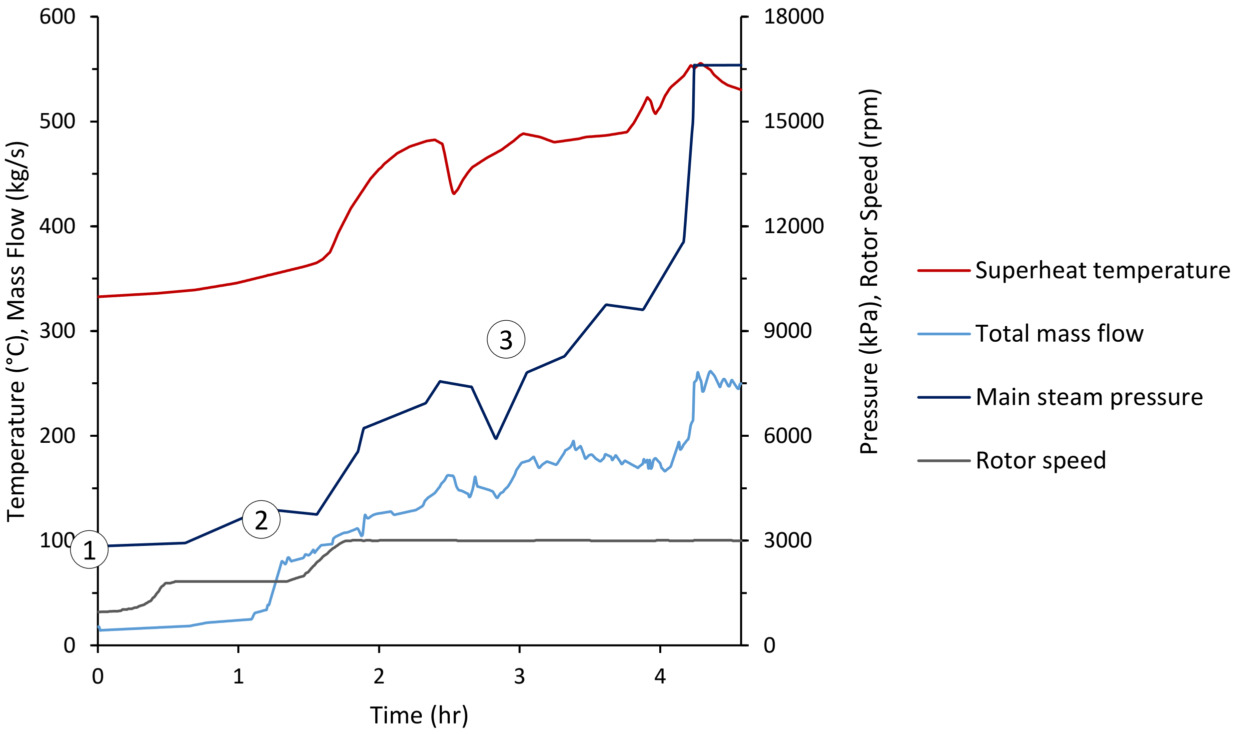

Figure 31: Full Cold Start Boundary Conditions

In modelling the initial start-up time step, given that the stage component cannot run at very low conditions, an initial condition was chosen with a significant mass flow. The entire start-up accounts for approximately 4 hours and 43 minutes of the 48 hours of data collected from the candidate unit.

Using the theoretical start-up graph and the reported data, three distinct stages were identified through the start-up to best represent what the turbine unit would experience during this operation. It is worth noting that this was a particularly difficult stage of the study as assumptions had to be made by looking at the data and an element of reverse engineering had to be used to develop the representative start-up.

Stage 1: Steam is admitted to the Turbine unit after initial heating of the casing, through flange heating. The HP By-Pass Valve is in the fully open position, with all steam flowing through to the IP and LP cylinders. All Feedwater Heaters are off.

Stage 2: Approximately 72 minutes after initial steam admission, turbine rotor speed is held at approximately 1830 rpm to account for differential expansion and Benson Conditions being met in Boiler. HP ESV is opened allowing steam into the HP cylinder. HP By-Pass Valve is fully closed. Final turbine rotor run-up ends once 3000 rpm is reached.

Stage 3: Feedwater Heaters are put into service prior to turbine synchronisation to the National Grid.

The cold start used also features a period of “steady state” operation, constituting the last 30 minutes, in order to demonstrate the capabilities of the turbine model stage components and process model in comprehensively simulating turbine operation.

The data collection ‘phase’ of the study was a continuous exercise through the study as one gained clarity as to the necessary plant data needed to develop such a turbine model with the above constituting what was found to be the most useful information collected over the course of the study

4. 1D Thermofluid Modelling

4.1 Multistage Turbine Development

The 1D Turbine Model was developed using Flownex SE software. The modelling methodology was separated into two parts; the sizing of the turbine stage components and the development of a process model to simulate the external plant boundary conditions for the detailed turbine model.

4.1.1 Nozzle Analogy Sizing

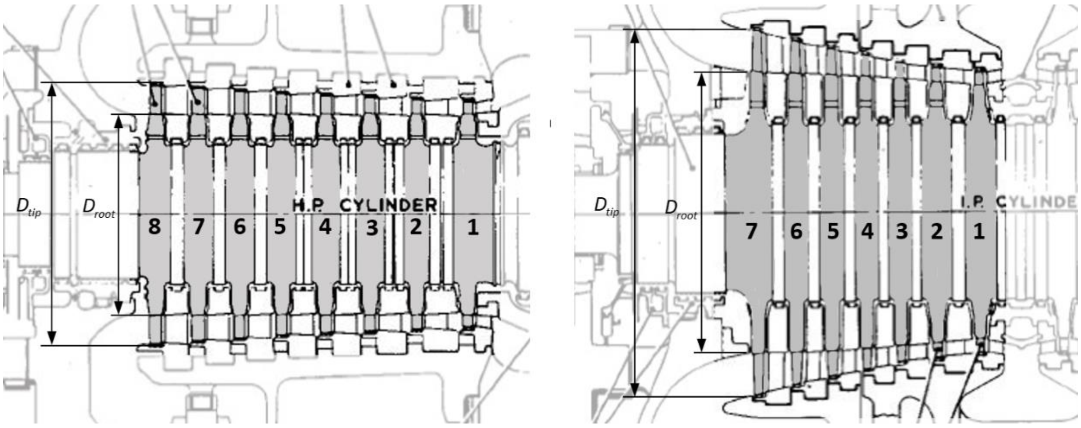

(i) (ii)

Figure 32: (i) HP and (ii) IP Turbine cross-section stage drawings

The Nozzle Analogy used to model each turbine stage is centred on the correct sizing of each nozzle area, shown in Figure 14 and Figure 15. The respective areas links the mass flow and pressure drop over each blade row, and consequently the enthalpy drop and flow velocities. The heat balance diagram was used to extract the pressure and temperature at the inlet and outlet of both units, as shown in Table 2.

Table 2: Assumed Blading Variables for Initial Sizing

Quantity	**Value**	
	HP	**IP**
Number of stages	8	7
Inlet Pressure (MPa)	16.1	3.55
Inlet Temperature (°C)	535	535
Outlet Pressure (MPa)	4.1	0.407
Outlet Temperature (°C)	334	241

Using these known conditions, the isentropic and actual enthalpy drops ($\Delta h_{s.unit}$ and $\Delta h_{act.unit}$) across each unit could be determined from Equation 4.1 and 4.1:

$$\Delta h_{s.unit} = h_{in} - h_{s.out}\left(P_{out}, s_{in}\right) \qquad 4.2$$

$$\Delta h_{act.unit} = h_{in} - h_{out}\left(P_{out}, T_{out}\right) \qquad 4.3$$

Assuming an equal enthalpy drop per stage, the isentropic and actual enthalpy drop could be calculated as:

$$\Delta h_{s.stage} = \frac{\Delta h_{s.unit}}{N_{stage}} \quad and \quad \Delta h_{act.stage} = \frac{\Delta h_{act.unit}}{N_{stage}} \qquad 4.4$$

The sectioned turbine diagrams allowed for the rotor tip and root diameters to be determined with verification from more detailed inspection documents from installation and maintenance records, obtained from past maintenance conducted on the unit. The primary reason for this geometric input was the extraction of the mean diameter (D_m) which was determined from the following equation:

$$D_m = \frac{D_{tip} + D_{root}}{2} \qquad 4.5$$

In this study, the true blade dimensions could only be sourced for the IP turbine blades, with the HP turbine blades being estimated from the high level, sectioned turbine diagram, as seen in Figure 32. During a site visit to the candidate unit, the first stage of the HP turbine was measured manually, with the remaining diameters scaled relative to a measured difference found between the high level and manual measurements for the first stage. The mean diameter results for both the HP and IP turbine can be found in Appendix A.

For the initial blade sizing procedure, an average mean diameter was determined using the mean diameters determined for each stage. This average blade diameter allowed for an average blade velocity to be determined using

$$v_{b.av} = \frac{\pi \cdot D_m \cdot N}{60} \qquad 4.6$$

The actual enthalpy drop across each stage was used to solve for the probable stage loading using Equation 4.7

$$\psi = \frac{\Delta h_{unit.act}}{{v_{b.av_i}}^2} \qquad 4.7$$

Assuming the turbine operates at its maximum blade efficiency the reaction ratio can be solved from

$$\psi = 2 \cdot (1 - R) \tag{4.8}$$

The result of this process produced blading with virtually the same reaction ratio across the HP and IP units, as shown below:

Table 3: Reaction Ratios

Reaction Ratio	Value
HP Turbine	0.245
IP Turbine	0.237

From inspection of the cross-section drawings, it appears as-if there are balancing holes in the rotor discs indicating an impulse turbine. The author had the opportunity to view the turbine rotor during a maintenance outing, and the blades did appear to be similar to typical impulse blades, but with a slight reaction component visible as narrowing blade passages. The reaction ratios calculated are therefore realistic.

Mean line blade theory provides an optimum ratio of blade speed vs nozzle velocity, which can be used to calculate the possible stator exit angle (α) from

$$\Delta h_{s.isen_i} = \psi \cdot \left(\frac{v_{b_i}}{\cos\alpha} \right)^2 \tag{4.9}$$

The following stator exit angles were obtained:

Table 4: Stator Exit Angles

Stator Exit angle	Angle ($^\circ$)
HP Turbine	19.8
IP Turbine	15.1

The above exit angles and reaction ratios fall within industrial norms. From this point onwards, it will be assumed that the nozzle angle for each stage stays the same for the HP and IP turbine.

The process as described thus far is depicted in the flow chart of Figure 33

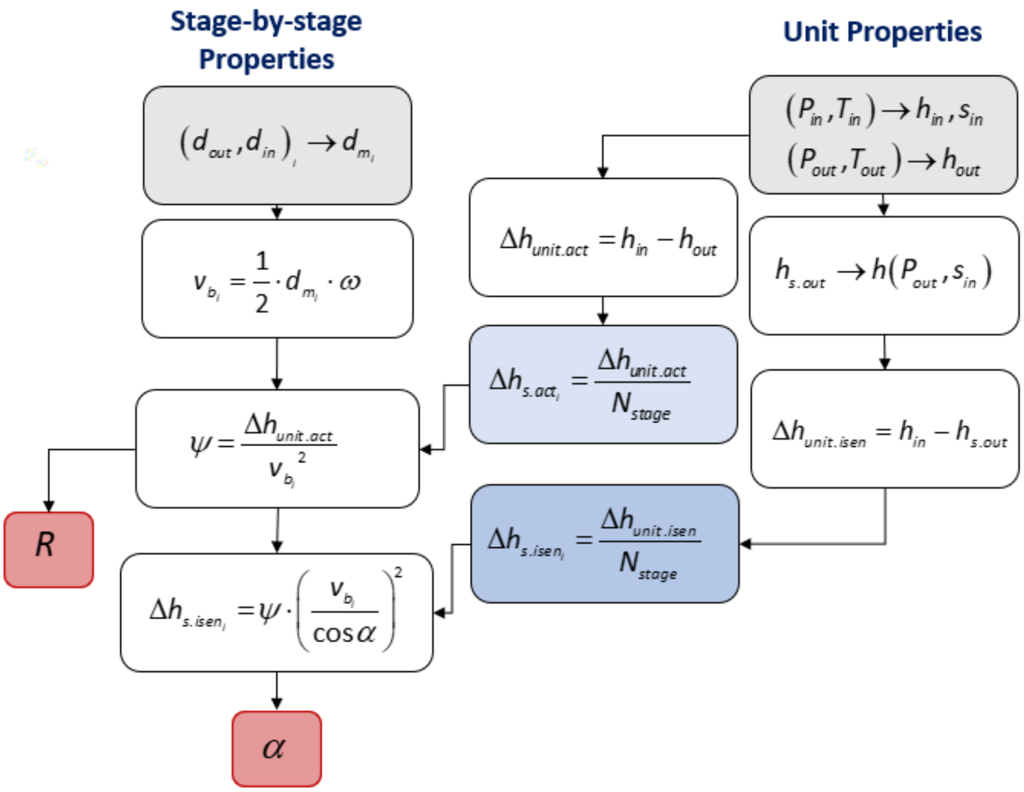

Figure 33: Reaction Ratio & Stator Exit Angle Process diagram

Equation 4.9 was re-used to calculate the actual enthalpy drop per stage considering the change in mean blade diameter. The sum of all the enthalpy drops was compared to the expected total enthalpy drop taken from the heat balance diagram. The results of this are shown in Table 5, which further confirms the method of establishing the reaction ratio and nozzle angle using an average mean diameter.

Table 5: Total unit enthalpy drop

	Expected	**Sum of stages**	**Error**
HP Turbine	346.98	347.23	0.07%
IP Turbine	630.24	631.89	0.26%

The next step is to determine the exit velocity of the stator and rotor of each stage. This is driven by the enthalpy drop over each blade, which can be obtained from the identified reaction ratio:

$$\Delta h_S = \Delta h_{s.stage} \cdot (1 - R) \tag{4.10}$$

$$\Delta h_R = \Delta h_{s.stage} \cdot (R) \tag{4.11}$$

Using the velocity triangles as derived by Fuls [1], the absolute stator exit velocity (v_2) and relative rotor exit velocity (v_{3r}) can be calculated using Equations 2.4 and Equation 2.5 respectively.

Starting from the inlet, the pressure and enthalpy at the stator and rotor outlet can be calculated, which enables one to determine the exit density. Using conservation of mass, the nozzle areas are:

Stator Nozzle Area:
$$A_S = \frac{\dot{m}}{\rho_{i,s} \cdot v_2} \tag{4.12}$$

Rotor Nozzle Area:
$$A_R = \frac{\dot{m}}{\rho_{i,r} \cdot v_{3r}} \tag{4.13}$$

The Nozzle Areas were calculated for both units. An example of the results for the HP Turbine is represented in Table 6, below.

Table 6: Initial Isentropic HPT Nozzle Areas

Stage	Enthalpy/Stage (kJ/kg)	V_2 (m/s)	V_{3r} (m/s)	Stator Nozzle (m^2)	Rotor Nozzle (m^2)
1	39.93	245.4	176.5	**0.044**	**0.062**
2	40.93	248.5	178.7	**0.046**	**0.066**
3	42.07	251.9	181.2	**0.049**	**0.070**
4	42.86	254.3	182.9	**0.052**	**0.074**
5	43.73	256.8	184.7	**0.056**	**0.079**
6	44.79	259.9	186.9	**0.060**	**0.085**
7	45.72	262.6	188.9	**0.064**	**0.091**
8	47.19	266.8	191.9	**0.069**	**0.098**

The above process is represented in Figure 34 below. The complete process allows for the computational inexpensive capturing of both turbine stage geometries, with little OEM input, as well as the enthalpy drop characteristics of the unit, using basic heat balance diagrams.

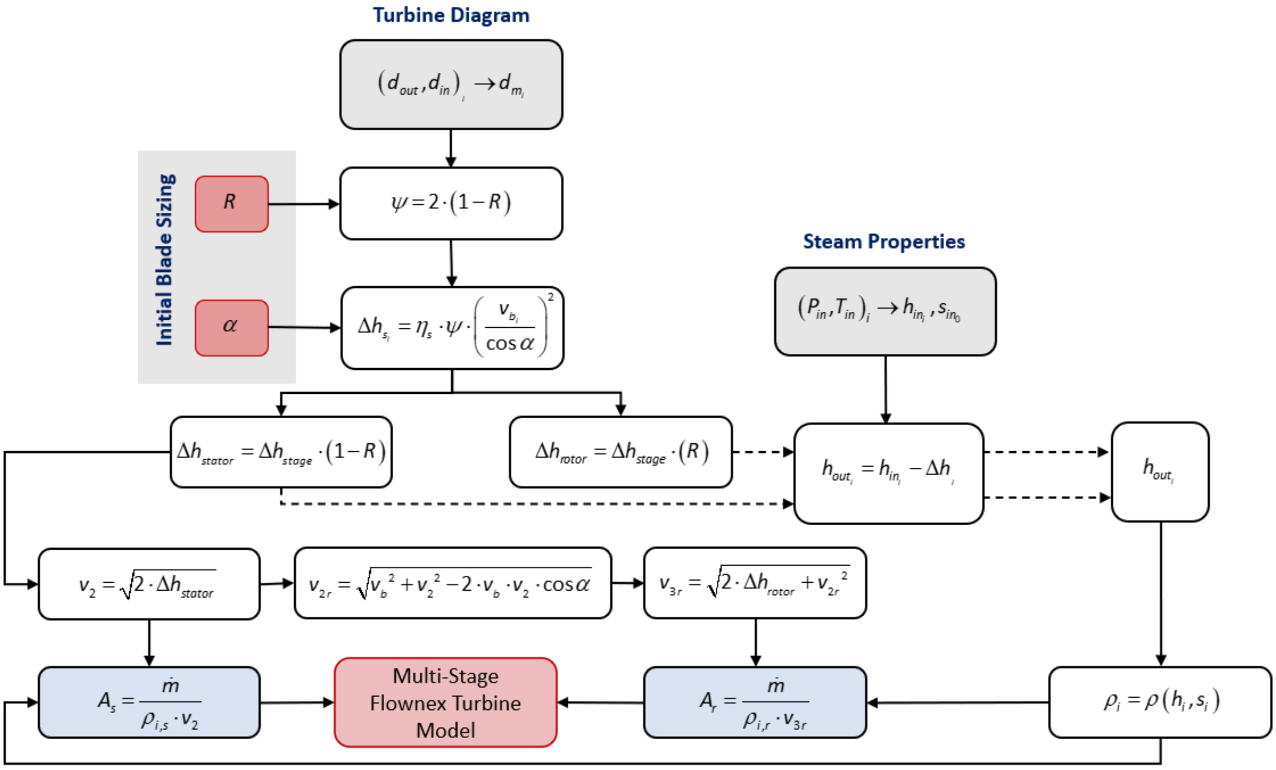

Figure 34: Nozzle Sizing Process Calculation

Whilst this process was first formulated using the HP turbine from the candidate unit, the process was repeated for the IP turbine. However, an additional consideration had to be made for the IP turbine due to the extraction flow between the fourth and fifth stage.

According the to the turbine modelling methodology developed by Fuls [1], the presence of the extraction flow calls for the IP Turbine to be considered as two turbine units connected in series. With two representative turbines formed, extraction flow was accounted for in the interface of these representative turbines.

Additionally, the IP turbine featured two halves of seven stages each, receiving half the total mass flow of the unit. Whilst it is possible to model both halves of the IP turbine, it was found to be more efficient to simply model one half of the unit, which received the full unit mass flow and having double-sized nozzle areas.

Figure 35 demonstrates the isolation of one half of the IP turbine as well as the development of two representative turbines in order to account for the extraction flow to the relevant feedwater heater.

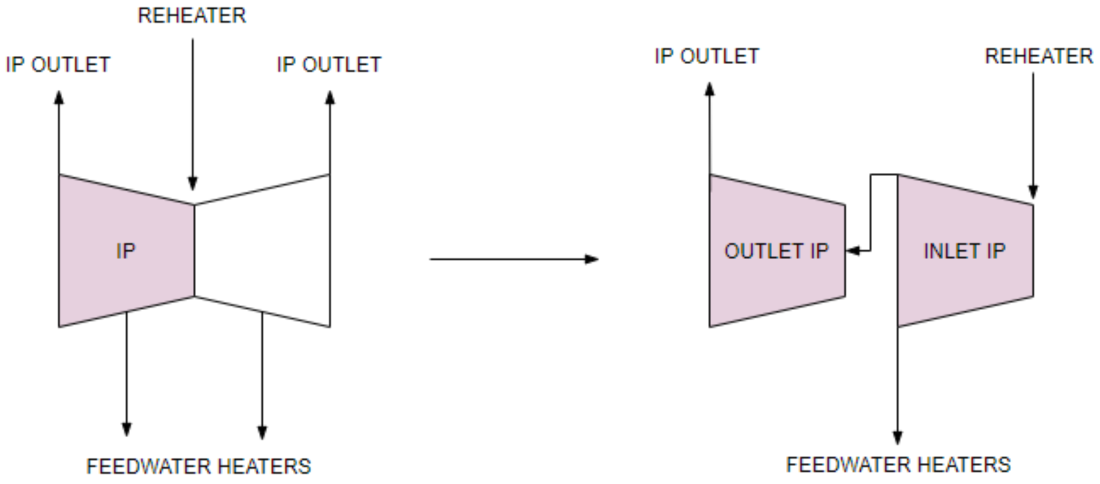

Figure 35: Nozzle Analogy Steam Extraction methodology

4.1.2 Multi-Stage Turbine Calibration

The approach undertaken in the preceding section serves as a “first-pass” of each stage of the HP and IP turbines which can then be transferred to the Flownex 1D Turbine Model. Of primary focus during this phase of model establishment was the inclusion of stage losses. The inclusion of stage losses results in changes to the initial nozzle areas as those were determined using isentropic conditions. The adjustments are achieved through various calibration steps. An example of the stage parameters imported from the initial nozzle sizing, for the first stage of the HP turbine, is shown below, with the quantities which needed calibration marked in red.

Table 7: Turbine Stage Component Parameters from Nozzle Sizing for HP 1st Stage

Conditions	Excel Result
Stator Nozzle Area (m^2)	0.044
Rotor Nozzle Area (m^2)	0.066
Stator Loss Coefficient	0.1
Rotor Loss Coefficient	0.001
Carry Over Efficiency	0.9
Mean Blade Diameter (m)	0.8820
Stator Exit Angle (°)	19.8

Notable quantities included in this phase are the definition of a constant carry over efficiency of 90% for all stages, except for the last stage. The last stage loss coefficient of less than 1% (chosen to be nominally 0.001) was assumed. This is similar to what is proposed by Fuls [1].

A key parameter used during the calibration of the multi-stage turbine is the respective loss coefficients of the stator and rotor. Due to the impulse blading found in both units, an initial loss coefficient was assumed to be 10% (0.1) for the stator and a loss coefficient of less than 1% (chosen to be nominally 0.001) was assumed for the rotor. This assumed that the stator would make a substantially greater contribution to the stage losses than that of the rotor, due to the significant enthalpy drop across the stator. The selection of the loss coefficients was informed by the previous work of Fuls [1] and Clark [20]. In their work, it was assumed that typical loss coefficients could range between 10 to 20% (0.1-0.2) in the full-load, steady-state simulation of an operating boiler feed pump turbines.

Figure 36 shows the multi-stage HP turbine model. A similar but independent IP turbine model was also developed. Inlet Boundary conditions were set as a function of Superheater Outlet Pressure (P_{in}) and Temperature (T_{in}) and the outlet condition was initially prescribed as the full-load mass flow ($\dot{m}_{full}$) from the Heat Balance diagram. For the HP turbine of the candidate turbine, the following boundary conditions were prescribed as in Table 8.

Table 8: Turbine Model Calibration Initial Boundary Conditions

Boundary Condition	**Value**
Inlet Pressure (MPa)	16.1
Inlet Temperature ($^{\circ}C$)	535
HPT Mass Flow (kg/s)	500.5
Target Exit Enthalpy (kJ/kg)	3050.4
Target Exit Pressure (MPa)	4.1

The initial model only considered the main steam flow (no gland steam low), allowing for the calibration process developed during the study.

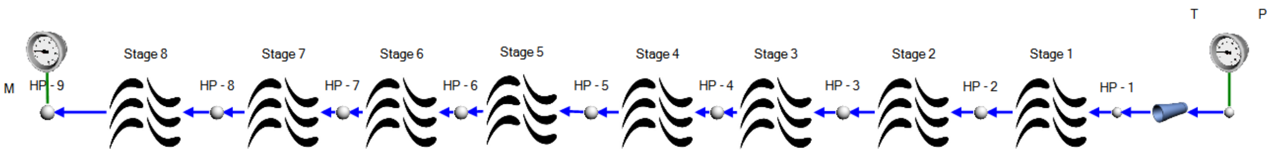

Figure 36: Multi-Stage HP turbine from Candidate Unit

The model calibration was performed manually in three stages through multiple steady state Flownex simulation runs according to the order described in Figure 37, below.

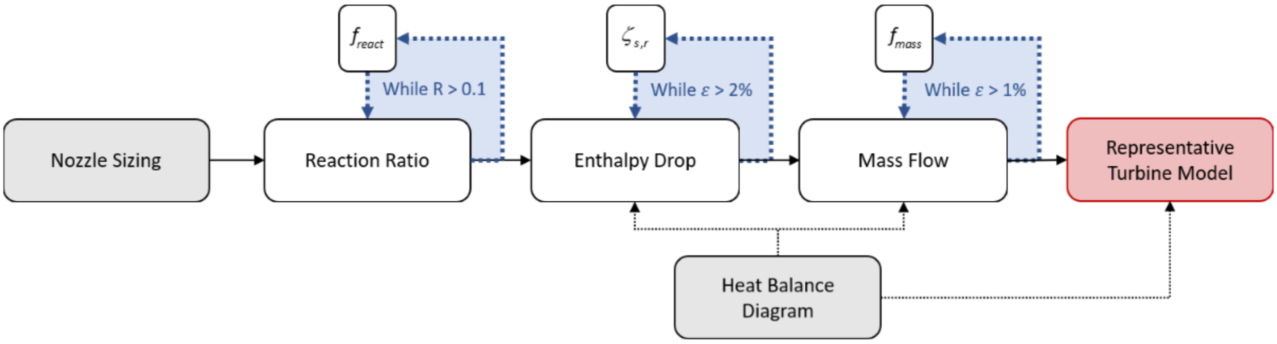

Figure 37: Multi-stage Turbine Calibration Methodology

Correction factors were used to adjust the nozzle areas and losses to achieve the expected turbine performance (i.e. consistent reaction ratios, total enthalpy and reported mass flows given pressure boundaries). These were done using Parameter tables in Flownex.

a) Reaction Ratio calibration

The reaction ratio (R) is the degree by which the stator and rotor contribute to the overall enthalpy drop across a single turbine stage. For a pure impulse turbine, a reasonable reaction ratio would be approximately 0.1. As described in the preceding chapter of this report, the reaction ratio of both units was approximately 0.24. The reaction ratio of a single turbine stage is given by Equation 4.14

$$R = \frac{\Delta h_R}{\Delta h_{stage}} \qquad 4.14$$

From the first run of the initial nozzle areas, the reaction ratio was found to be inconsistent and typically above a practical reaction ratio for an impulse stage. Given the direct relation of enthalpy drop to nozzle area, a manipulation of both stator and rotor nozzle areas was performed. The reaction ratio correction factor ($f_{react} < 1$) was formed to increase the nozzle area of the stator stage (A_S) and decrease the nozzle area of the rotor stage (A_R) in the event that the reaction ratio was too high, as was the case in this study. The manipulation is given by Equation 4.15 and 4.16.

$$A_S = \frac{1}{f_{react}} \cdot A_{S.original} \qquad 4.15$$

$$A_R = f_{react} \cdot A_{R.original} \qquad 4.16$$

A smaller adjustment factor would increase the stator nozzle area, and thus the enthalpy drop across the stator, and decrease the rotor nozzle area by the inverse ratio, thus decreasing the overall reaction ratio.

Because of the presence of balancing holes in the rotor discs, the stages are essential pure impulse stages. It was therefore decided to “push” the reaction ratio of each stage down to below 0.1 during the calibration process. Calibration of the stage reaction was performed in a “cascading” approach, starting from the first stage. Following an acceptable reaction ratio, the next stage was iterated by further decreasing the correction factor for the remaining stages until the threshold conditions were met for the next stage, continuing this process until all of the stages were calibrated.

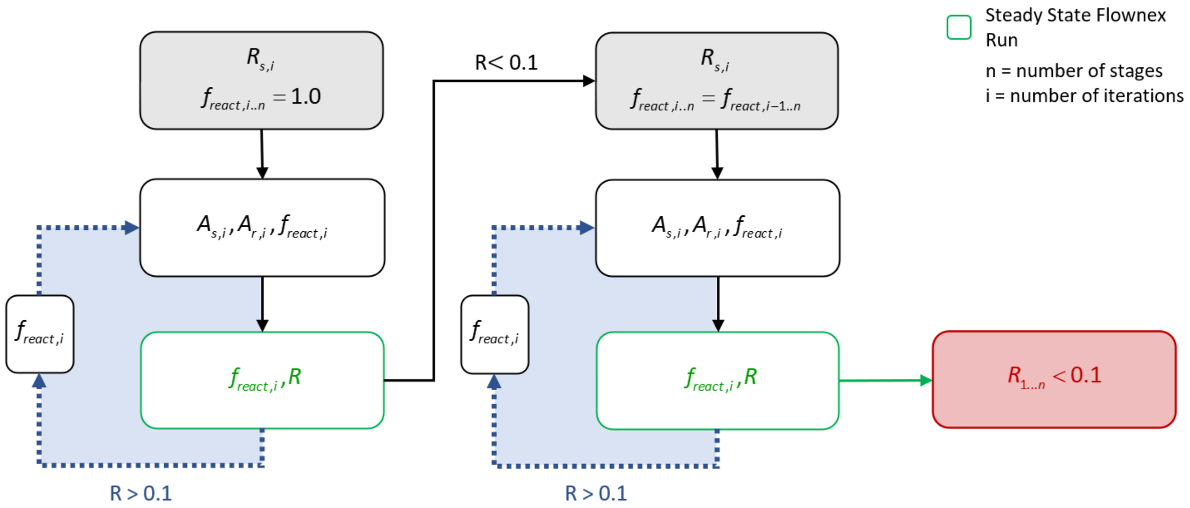

Figure 38: Manual Iteration workflow for Reaction Ratio Correction

This process can be repeated for n-stages as shown in Figure 38. In this study there were eight HP turbine stages and seven IP turbine stages. The result of the manual calibration proved successful and resulted in a consistent reaction ratio being observed across all stages of the HP and IP turbine, as is demonstrated by Figure 39.

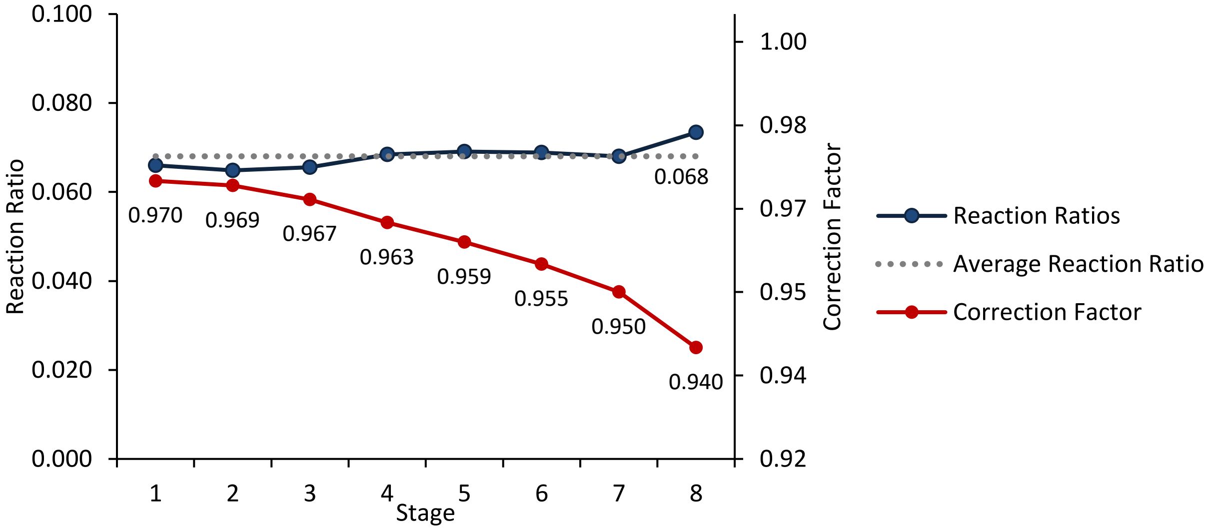

Figure 39: Reaction Ratio Calibration Results for HP Turbine

An average reaction ratio of 0.068 and 0.076 was achieved in the HP and IP turbine units respectively. Despite the seemingly independent nature of the reaction ratios of each stage, it was found to be vital that each stage be calibrated with respect to the entire unit, with all upstream stages included. The parabolic trend of the correction factor suggests that the effect of calibration is compounded in the upstream stages, therefore enforcing the need for the "cascading" approach implemented in this study.

Further development of this method may include an automated calibration approach, whether through the use of the built-in designer in Flownex SE or in an independently developed Python script.

b) Enthalpy Drop Corrections

A built-in parameter to the Turbine Stage component used in this study, as developed by Fuls [1], is the Stator and Rotor Loss Coefficients (ζ_S & ζ_R). The loss coefficients determine the useful energy extraction of each stage as a function of the geometric and flow losses. A larger loss coefficient will result in lower nozzle velocities and thus less energy available for extraction. The net effect is then an increase of the outlet enthalpy of the unit. The calibration was performed relative to the total enthalpy drop across the entire HP or IP turbine. Figure 40 shows the enthalpy calibration process which was done manually.

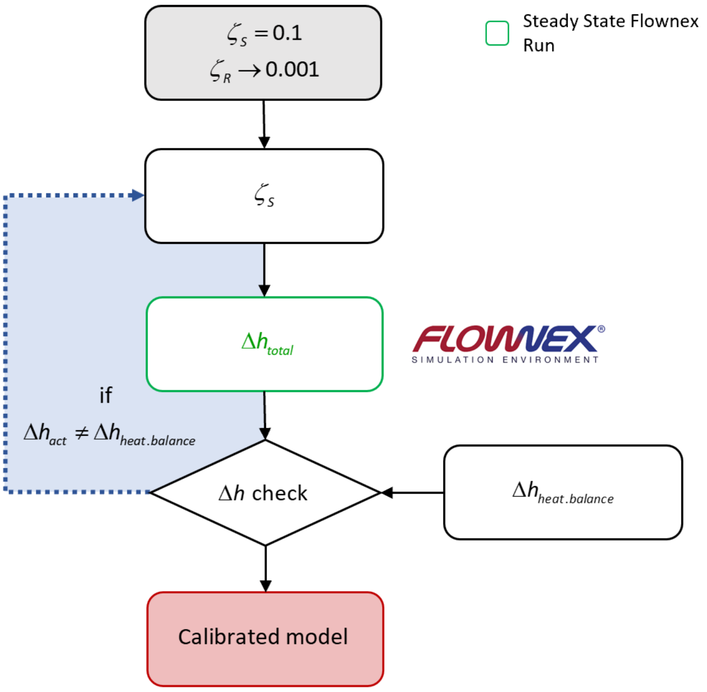

Figure 40: Enthalpy Drop Calibration for single turbine unit

As in the reaction ratio calibration, the process has the potential of being automated and features a simple loop comparing total enthalpy drop to the expected value. If the enthalpy drop was too low (i.e. too much energy extracted) a higher loss coefficient was defined and the Flownex model was run again until the enthalpy drop converged on the heat balance value. The calibration of the model towards the heat balance values was successful and yielded a stator loss coefficient 0.115 and 0.112 for the HP and IP turbines respectively.

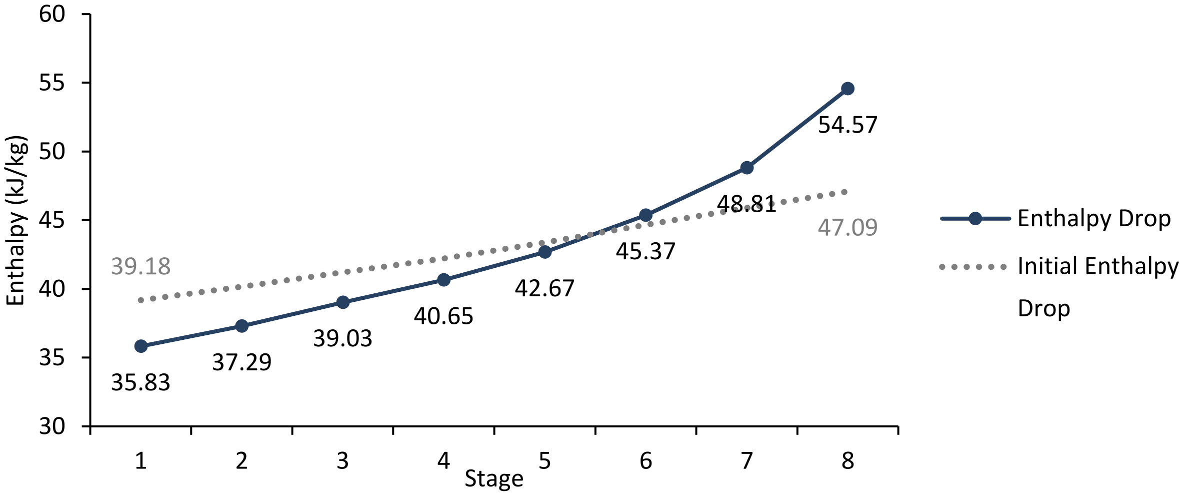

Figure 41: Comparison of modelled vs isentropic enthalpy drop across HPT

From Figure 41, it is evident that the initial isentropic assumption made for the Nozzle Area sizing is fairly accurate in comparison to the true enthalpy behaviours. This is mainly because modern turbines run at high efficiencies within the energy production process, such that an isentropic assumption could be used to approximate real world operation within a high degree of accuracy. However, despite this, given the desire to simulate low load transients such as a cold start-up, a calibration of the model considering a turbine with losses is more appropriate.

c) Mass Flow Correction

Given the previous calibration steps being performed with a full-load mass flow outlet boundary condition, a final mass flow calibration was performed. For the mass flow correction, the expected outlet pressure was prescribed to the outlet boundary and the Flownex model was run, this time solving for the total mass flow. The initial run, featuring the calibrated nozzle areas from the reaction ratio step produced a mass flow ($\dot{m}_{act}$) which deviated significantly from the expected full-load value ($\dot{m}_{\exp}$). However given the mass flow equation, in Equation 2.7, and assuming that the density and flow velocity remains constant, the desired mass flow can be achieved by scaling all the stator and rotor Nozzle Areas simultaneously by a correction factor equal to:

$$f_{mass} = \frac{\dot{m}_{\exp}}{\dot{m}_{act}} \quad 4.17$$

The mass flow correction factor was applied to the HP and both IP turbine segments independently as a function of the modelled mass flow observed during the initial simulation runs. This process was done twice, to account for some non-linearities in the system. Table 9, below, shows the formulated correction factors and final validation the mass flow through both turbine units

Table 9: Mass Flow Correction for HP and IP turbines

Parameters	**Unit**	**HP**	**IP1**	**IP2**
Expected flow	kg/s	498.90	433.13	383.88
Modelled flow	kg/s	466.70	408.20	391.13
Correction factor	**-**	**1.0696**	**1.0611**	**0.9815**
Final flow	kg/s	498.28	434.32	390.00
Error	%	-0.12	0.27	1.59

The above table demonstrates the ability for simple calibration techniques to predict the mass flow through the HP and IP turbines within a high level of accuracy. The IP outlet mass flow showed an acceptable yet larger deviation from the expected value. A possible reason for this is presence of the extraction flow between the fourth and fifth stages. The extraction flow complicated the prescription of a uniform correction factor across both representative turbines, and was a function of the feedwater heater boundary conditions in addition to a singular outlet condition, as in the HP turbine. Although the IP turbine calibration proved tricky, the model was deemed sufficiently accurate to proceed.

The application of the Mass Flow Correction Factor marked the end of the model calibration against the full load heat balance quantities. Table 10, shows the reduction in error in the model as a result of the calibration exercise described above.

Table 10: Validation of model against Heat Balance Before and After Calibration

		Initial Nozzle Sizing			**Correction Factors applied**		
Parameters	**Unit**	**100%**	**Expected**	**Error (%)**	**100%**	**Expected**	**Error (%)**
HPT Inlet Mass Flow	kg/s	467.7	500.6	6.57	500.5	500.6	0.01
HPT Outlet Pressure	MPa	4.052	4.107	1.33	4.106	4.107	0.02
HPT Outlet Temperature	°C	331.2	334.0	0.84	334.2	334.0	0.07
HPT Outlet Enthalpy	kJ/kg	3044.1	3050.02	0.19	3050.7	3050.02	0.02
FWH Extraction Pressure	MPa	1.170	1.213	3.58	1.251	1.213	3.11
FWH Extraction Enthalpy	kJ/kg	3201.8	3213.2	0.36	3213.3	3213.2	0.00
IPT Outlet Mass Flow	kg/s	361.96	383.88	5.71	390.56	383.88	1.74
IPT Outlet Pressure	MPa	0.366	0.409	10.59	0.408	0.409	0.25
IPT Outlet Enthalpy	kJ/kg	2935.0	2946.8	0.40	2946.1	2946.8	0.03
		Average Error (%)		3.29	Average Error (%)		0.584

It is evident through the above section that it is more than possible to formulate a representative main steam turbine model using the Nozzle Analogy approach, paired with a robust and systematic calibration approach. The calibration led to the reduction in error to less that 1% (0.584%), which is considered more than sufficient in typical turbine modelling.

4.2 Peripheral Flow Modelling

Following the calibration of the main steam flow path, focus was shifted to modelling peripheral steam flows. These were defined as flow paths of interest which would contribute to the relative expansion of each turbine units as well as capture heat transfer to surrounding turbine components.

4.2.1 Gland Seals

The modelling of the gland seals was completed through the use of heat balance diagrams, turbine drawings as well as observations during a site visit to the candidate unit. The Labyrinth Seal component of Flownex SE was used to model the gland seals of both units. From the turbine diagram it was evident that each gland seal could be defined as three distinct seals of assumed inner and outer diameter, as in Figure 42.

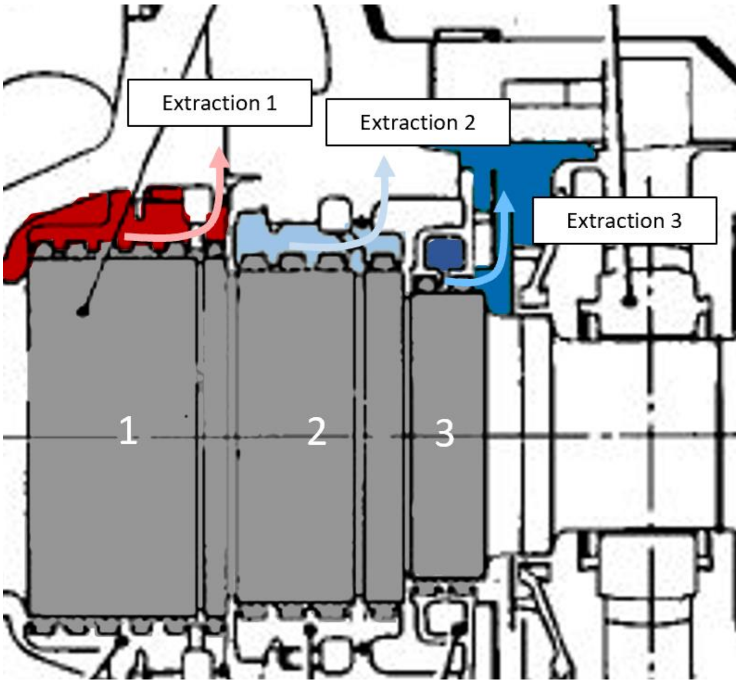

Figure 42: Gland Seal configuration in Sectioned Turbine Diagram

Whilst the finer geometries of the seals were not evident in the Turbine drawings, the actual measurements of the seals were estimated from images captured from a site visit to the candidate unit, as seen in Figure 43. This configuration was assumed for all of the gland seal stages, on both the HP and IP turbines.

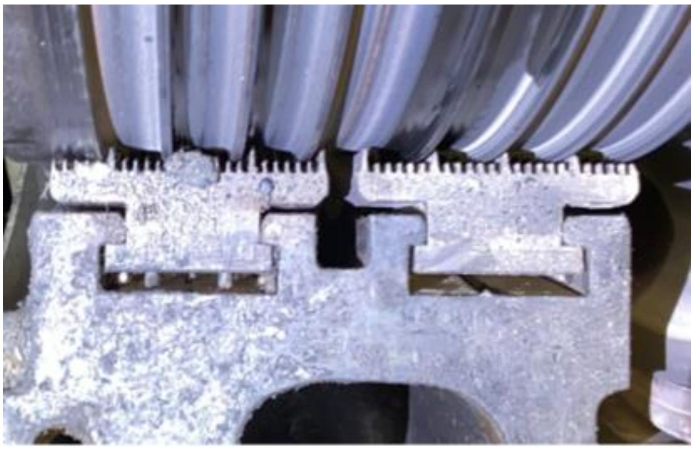

Measurement	Value
Number of diaphragms	2
Number of teeth/diaphragms	24
Tooth axial width (mm)	2
Tooth pitch (mm)	5
Tooth Clearance (mm)	3
Seal diameter	750

Figure 43: Labyrinth Seal sizing from On-Site images

In addition to the configuration of the seal teeth, the number of diaphragms were estimated by the number of "stages" observable from the sectioned turbine diagrams. Additionally, the outer seal diameter was estimated from the sectioned turbine diagram.

In the application of the seal configuration to the 1D Turbine Model, each set of gland seals is grouped into a Compound Gland Seal, as seen in Figure 44, with extraction flows at the boundaries of each seal.

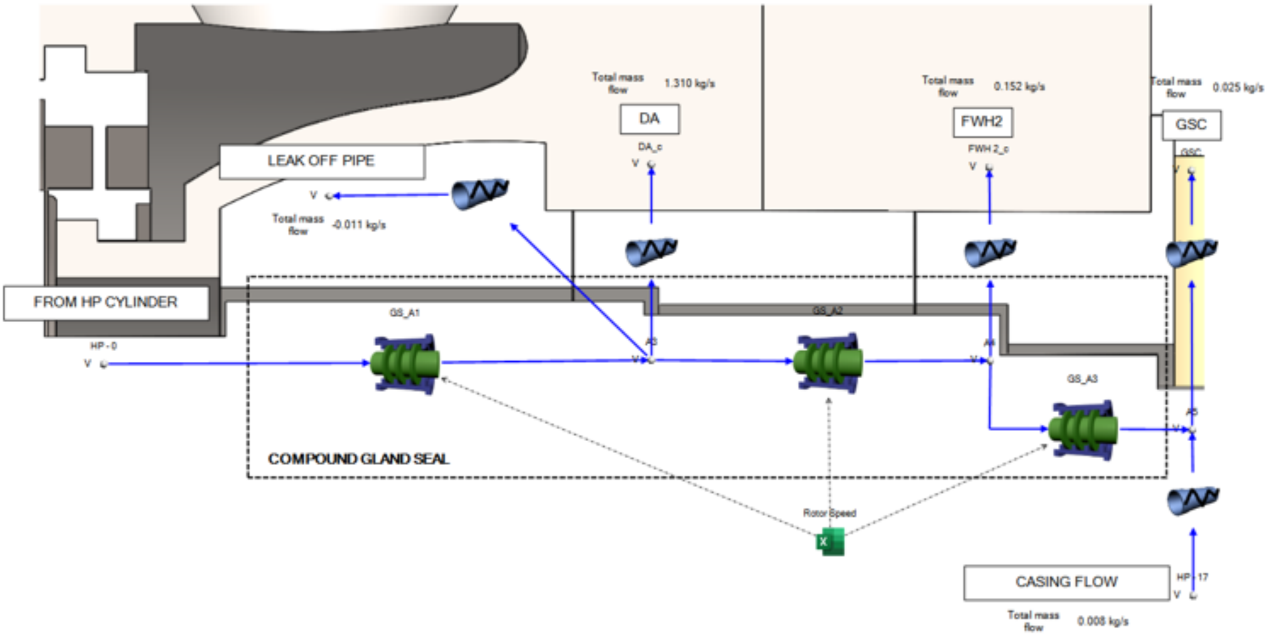

Figure 44: Gland Seal configuration in 1D Turbine Model, HP Turbine Inlet

A small calibration exercise was performed, by adjusting the Flow Admittance quantity in the Labyrinth Seal component to achieve the desired mass flow for a given extraction pressure. Whilst the extraction flow constitutes a small percentage of the overall mass flow, the temperature boundaries arising in the gland seals was of importance to the complete thermal modelling of the unit, particularly in transient operation.

In the completed model, the boundary nodes of each extraction point were connected to the Feedwater Train developed in the Process Model.

4.2.2 Internal casing space

The configuration of the particular HP turbine from the candidate unit, has a recirculating flow between the inner and outer casing. The recirculating flow is a small flow taken from the exhaust steam leaving the final stage which is eventually extracted in the Gland seal at the inlet side of the unit. The steam flow passes over a Barrier plate through a small clearance (approximately 5 mm) and across the outer surfaces of both casings, as demonstrated by Figure 45, below.

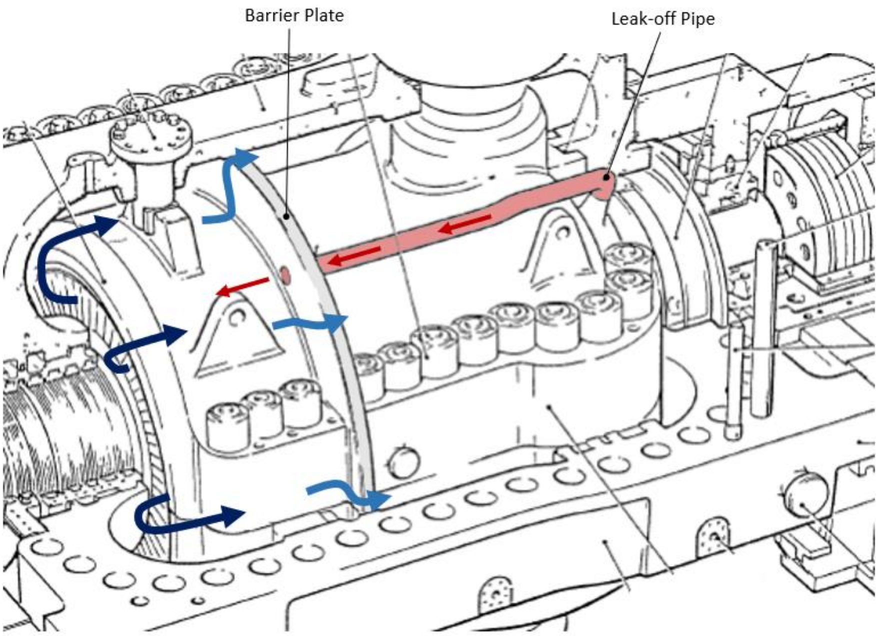

Figure 45: Return casing space flow to Inlet Gland Seals

Given the interaction of the steam with the heated inner casing, the steam was expected to exhibit a temperature gradient as a result of secondary heating/cooling. The modelling of the Leak-Off pipe was undertaken, as seen in Figure 44, where a small flow admittance was prescribed to the flow resistor used to represent this pipe. Despite the modelling, the flow through this pipe was expected to be relatively small and thus have a small effect on the temperature boundary predicted at both ends of the pipe.

Given the reduction in flow through the volume beyond the barrier plate, the model needed to predict not only the temperature at each node in the region but also a representative convection coefficient for eventual application to the FEA turbine model.

Given the complexity of modelling this region, it was separated into three phases:

- **Casing modelling:** capturing the convection and conduction within the casing components
- **Barrier Plate modelling:** capturing the expected pressure drop across the barrier plate
- **Steam modelling:** capturing the convective heat transfer coefficient of the steam as a function of flow characteristics

a) Casing Modelling

The objective of modelling the turbine case was to capture the thermal inertia presented by turbine components of significant mass, namely the turbine rotor and inner and outer casings. It was understood from literature that the capturing of the these thermal masses was fundamental to the clearance modelling of the overall steam turbine unit, as presented in work by Topel [16].

The modelling of the interaction of the recirculation steam with the surrounding casings was done using the Flownex Composite Heat Transfer component. This component allows one to discretise the conductive heat transfer flow through a mass as well as capture the convective heat transfer on the outer surfaces of the component.

In the casing model, the convective coefficient was assumed as nominal convective heat transfer coefficients for the upstream and downstream surfaces. In the case of the inner casing model, the outer surface ($T_{1.surf}$), was the recirculating steam temperature and the inner node ($T_{2.surf}$) was the main steam temperature for the connected stage.

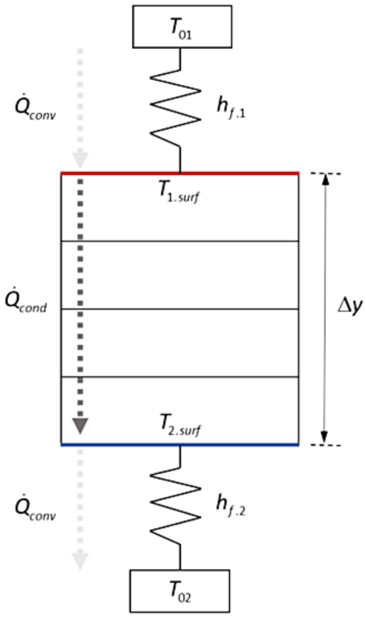

Figure 46: Composite Heat Transfer Component discretisation

The inner and outer casing was approximated as an annulus of the same nominal inner diameter as the actual casing component but an equivalent outer diameter such that the volume of the cylinder is equal to that of the relevant casing. From the 3D model developed for use in the FEA, the more accurate but complex casing volume could be determined. This was then used to solve the equivalent outer diameter, given the length is the same:

$$V_{cylinder} = \frac{\pi}{4} \cdot \left(d_{outer.eq}{}^2 - d_{inner.act}{}^2 \right) \tag{4.18}$$

Due to the different steam conditions on either side of the barrier plate, the cylinder was further divided into two sections relative to the barrier plate location, indicated by Inner A and Inner B, in Figure 47, below.

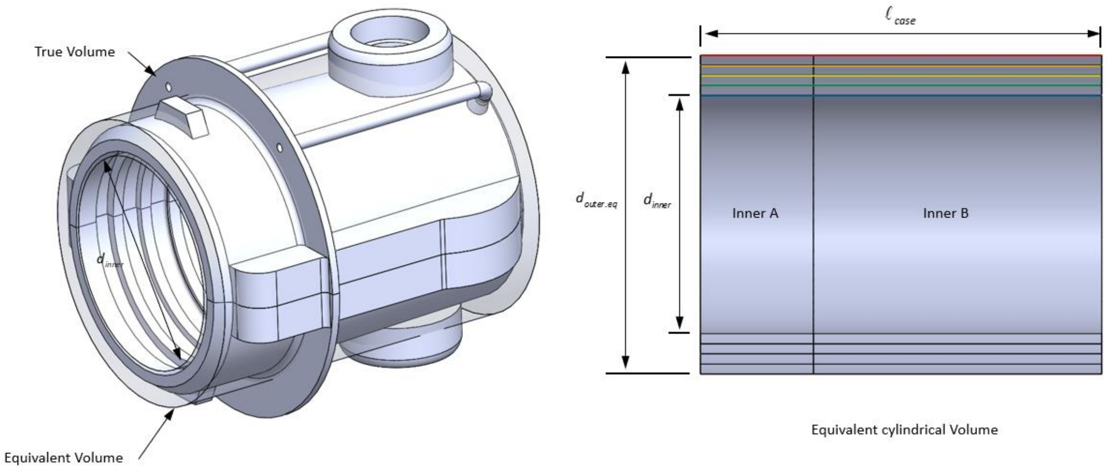

Figure 47: Inner casing volume simplification

The heat transfer element was also discretised along the radial length of the cylinder in order to monitor the heat transfer through the casing components. These temperature gradients were not to be representative of those which actually existing in the components but rather representative of the heat flux and thermal mass presented by the components. The discretised casing volumes also allowed for the confirmation of heat transfer through the volumes and is illustrated in Appendix C.

b) Barrier Plate Modelling

The Barrier Plate was modelled as a single toothed Labyrinth Seal of a given diameter and measured cold clearance taken during the site visit inspection of the unit. Below are the sizing parameters, in Table 11, and clearance measurement, in Figure 48.

Table 11: Barrier plate sizing parameters

Parameter	Value
Seal type	Straight
Seal orientation	Axial
Number of Teeth	1
Axial Width (mm)	15
Tooth Pitch (mm)	1900
Clearance (mm)	5
Seal Diameter (mm)	1910

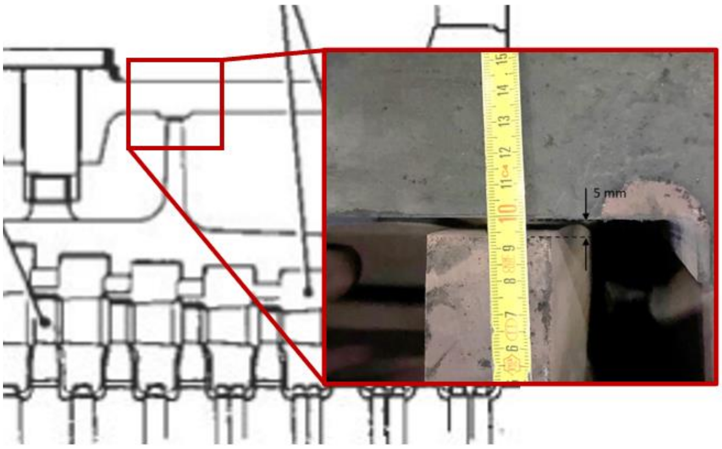

Figure 48: Barrier plate clearance measurement

The flow admittance through the barrier plate was calibrated to produce a representative mass flow to the internal casing space. This was difficult as this is not a mass flow individually recorded on site and is a component of the overall gland steam bled from the inlet gland seal. The admittance was calibrated such that a slight temperature gradient was observed in the space beyond the barrier plate whilst not significantly affecting the HP exhaust mass flow. The result of this calibration was a mass flow over the barrier plate of approximately 15 kg/s (3% of full load main steam flow). With the HP exhaust mass flow being specified by the Heat Balance diagram, this value was closely monitored during the barrier plate calibration.

c) Steam modelling

Given the quite small mass flow and large cavity space, in comparison to the flow leaving through the turbine exhaust, a significantly lower convective heat transfer coefficient can be expected in the cavity volume. As such, an appropriate correlation was selected to quantify the expected heat transfer coefficient seen in this volume.

The Dittus-Boelter equation is a well-known correlation used to derive the Nusselt number, and thus the Convective Heat Transfer Coefficient. This correlation was selected as it is widely used and is valid for turbulent flows through smooth surfaced tubes [21], conditions present in an operational steam turbine. Given the concentric cylinder simplification in modelling the casing volumes, one was able to apply the correlation for a simple annulus shape with known inner and outer diameters. As the primary objective of the modelling approach was to capture thermal mass and the loss of heat to the surrounded metal components, the quantification of convective boundary conditions was important. The following form of the Dittus-Boelter equation was used in this study.

$$Nu = \frac{h \cdot D}{k} = 0.023 \cdot \mathrm{Re}^{0.8} \cdot \mathrm{Pr}^{n} \qquad 4.19$$

Where n = 0.3 represents the case of fluid cooling, which was used to model the effect of heat loss to the surrounding turbine components.

A simple script was created, using Flownex components, to solve the Dittus-Boelter equation for the casing space. The script broadly considered the two nodes on either side of the barrier plate as well as the steam characteristics over the barrier plate. From the casing simplifications the equivalent flow area was determined using the below equation.

$$A_{space} = \frac{\pi}{4} \cdot \left(d_{sp.out}{}^{2} - d_{sp.in}{}^{2} \right) \qquad 4.20$$

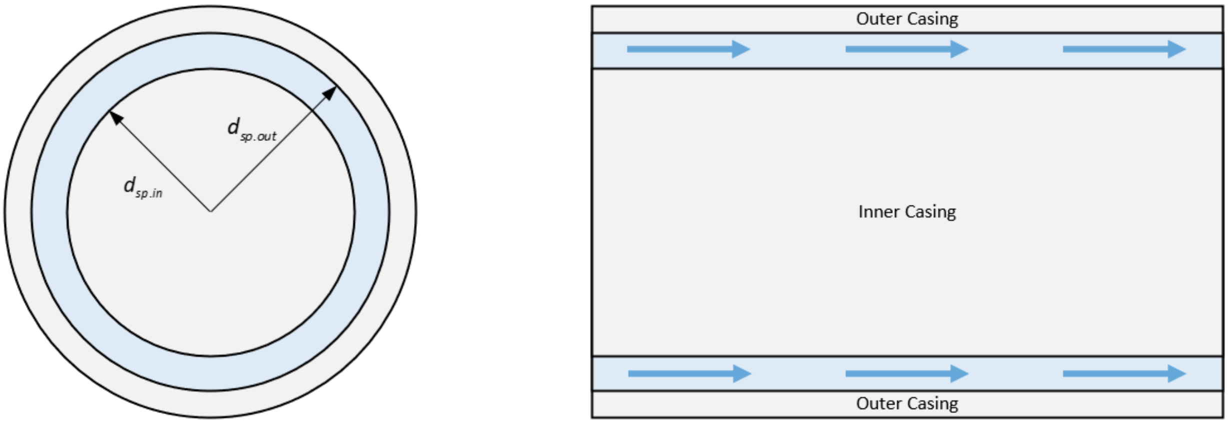

Figure 49: Casing spacing geometry

From the known cross-sectional area and the mass flow rate, one was able to calculate the steam velocity using the following equation and making a constant density assumption:

$$v_{steam} = \frac{\dot{m}}{\rho \cdot A_{space}} \tag{4.21}$$

The hydraulic diameter for an annular shape is:

$$D_{hy} = d_{sp.out} - d_{sp.in} \tag{4.22}$$

Having captured the geometric constraints of the casing space, the Reynolds Number could be solved for using the steam conditions such as dynamic viscosity and density as collected from the inlet node.

$$\mathrm{Re} = \frac{D_{hy} \cdot v_{steam} \cdot \rho}{\mu} \tag{4.23}$$

Where μ is the steam viscosity and ρ is the inlet density.

Using the same inlet conditions, the Prandtl number was solved for using the inlet steam conductivity and heat capacity applied in the below equation

$$\mathrm{Pr} = \frac{\mu \cdot C_p}{k} \tag{4.24}$$

Where C_p is the steam heat capacitance and k the thermal conductivity of the inlet steam.

From the Reynolds Number and Prandtl Number, the Nusselt Number was solved, and the Convective Heat Transfer Coefficient (*h*) can be estimated from Equation 4.19, above. A visual representation of the above process is presented in Figure 50, demonstrating the use of the inlet steam conditions and flow characteristics to predict an appropriate Convective Heat Transfer Coefficient (*h*) for the casing space.

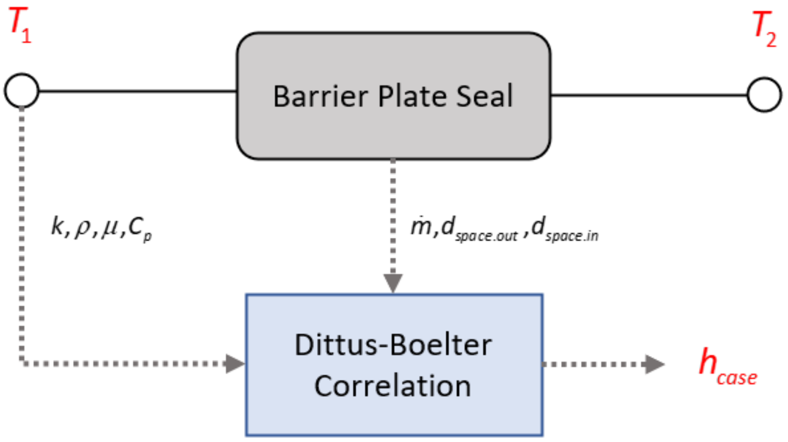

Figure 50: Dittus-Boelter solution methodology

The combination of the modelling the heat transfer between steam and surrounding casings allowed for a representative model of the internal casing space in the HP turbine. The upstream nodes of the inner casing heat transfer elements are connected to the 4th and 7th stage nodes as they are representative of the relative temperatures experienced on either side of the barrier plate, as shown in Figure 51.

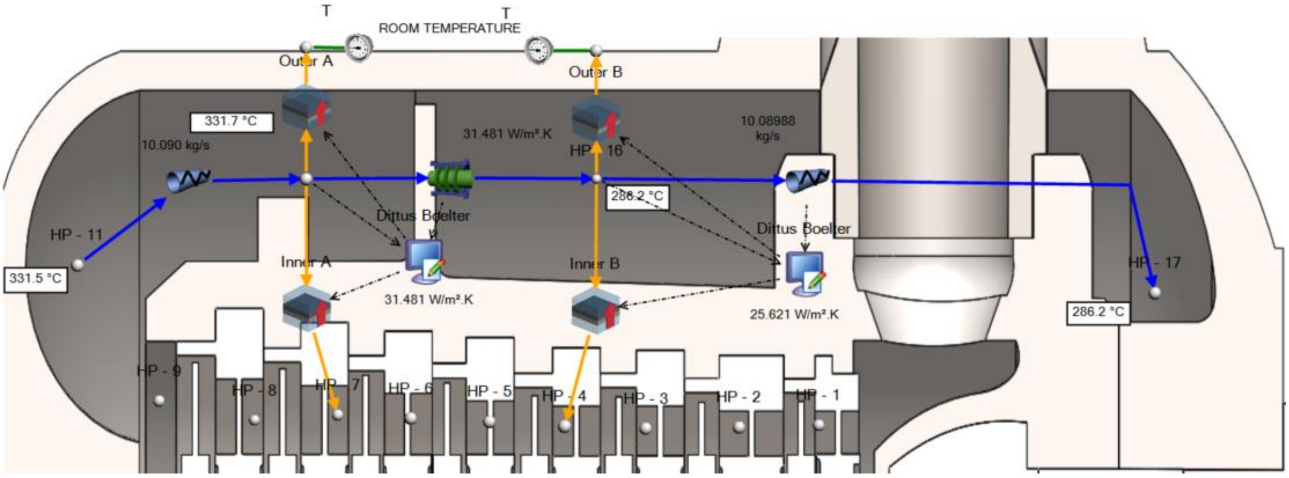

Figure 51: Casing spacing modelling

For the outer casing, a room temperature of 30°C was assumed. It was also noted that the outer turbine casing is surrounded by an insulating layer which insulates the casing from the outer atmosphere. Due to this insulating layer a small convective coefficient was selected to represent the minimal heat loss on the outer surface of the turbine unit. This insulation was simplified in the final 3D FEA model by assuming an adiabatic boundary on the outer surface.

The result, illustrated in Figure 51, shows a full load steady state case, with maximum mass flows present. From this case it is evident that the estimated convective heat transfer coefficient was approximately 30 $W/m^2{\cdot}K$, indicative of a low forced convective interaction as opposed to the high forced interaction through the blade passage. The results of the full-load validation highlighted the importance of taking a detailed convective approach in this region of the turbine.

Whilst it was initially determined that, due to the low velocity of the steam in the casing space, a greater number of discretised heat transfer elements would show no further detail than modelling the two respective spaces, it was found, during later phases of the study, that a more refined understanding of this space was important in order to accurately determine the thermal expansion of the inner and outer casing. Challenges were presented in validating the thermal response of the model relative to site data. In future work, it would be recommended that the space beyond the barrier plate be discretised into a greater number of volumes, along the axial length of the casing, to track a more accurate temperature gradient.

4.2.3 Rotor Modelling

As highlighted by Topel [16], it is important to capture the thermal inertia of the turbine rotor as it is a component of substantial mass. The rotor was approximated as a solid cylinder of constant radius, and subdivided along the length to represent each individual stage. The span of the rotor considered was the span under which the main steam interacted with the rotor, excluding gland seals. The thermal mass of the blades was assumed to be insignificant relative to the mass of the rotor.

Each division was represented by a Composite Heat Transfer component, with an assumed constant convective heat transfer of $h_{f.2} = 1000\ \text{W/m}^2\text{.K}$ for the steam side interface. The assumption was made that due to mass flow being sufficiently high in this region a convective coefficient in line with that of forced convective flow would be observed.

In a similar method to the inner and outer casing, the geometry of the rotor was simplified to a simple cylindrical solid. The simplification in Figure 52 shows a wedge slice of the approach undertaken.

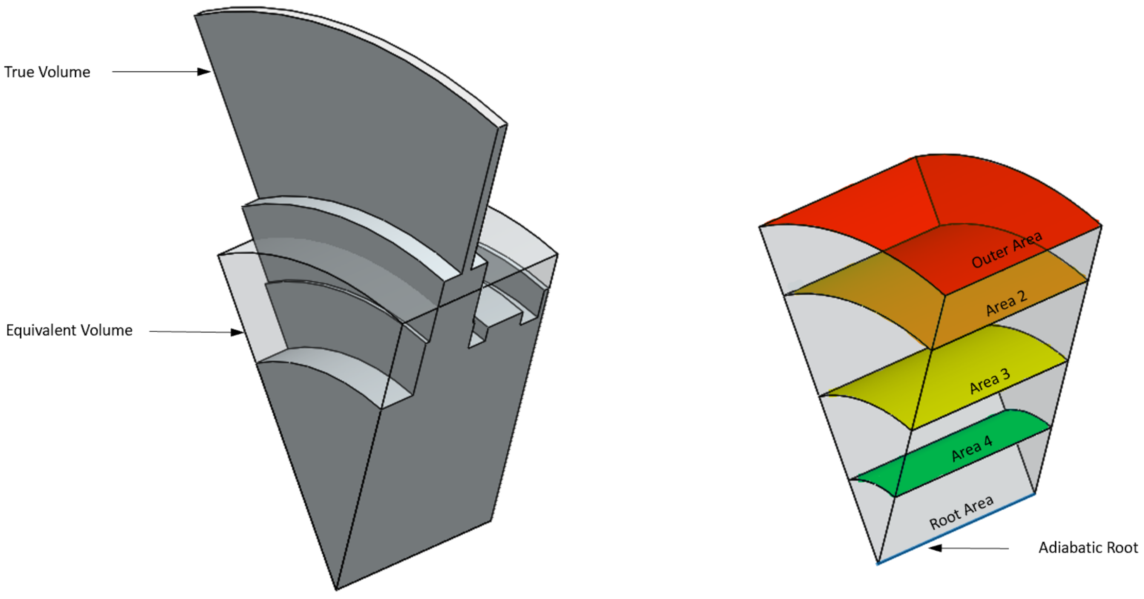

Rotor Heat Transfer Element

Equivalent Volume discretisation

Figure 52: Rotor Simplification and Discretisation

The simplification sought to maintain the known volume of the complex rotor geometry by creating a representative outer diameter, thus producing an equivalent volume. A convective boundary was prescribed to the outer cylindrical area of the rotor and an adiabatic root was prescribed at the centre. Whilst later phases of the project found a bore through the centre of the rotor, this bore was not modelled in the 1D Flownex Turbine Model.

Whilst heat transfer was primarily captured in the 3D FEA Turbine Model, the radial discretisation of the equivalent volumes was undertaken as a means of confirming heat transfer behaviours through the solid turbine components, as shown in Appendix B. Each turbined stage was represented by an equivalent Composite Heat Transfer element as in Figure 52. The final layout of the rotor heat transfer is detailed in Figure 53.

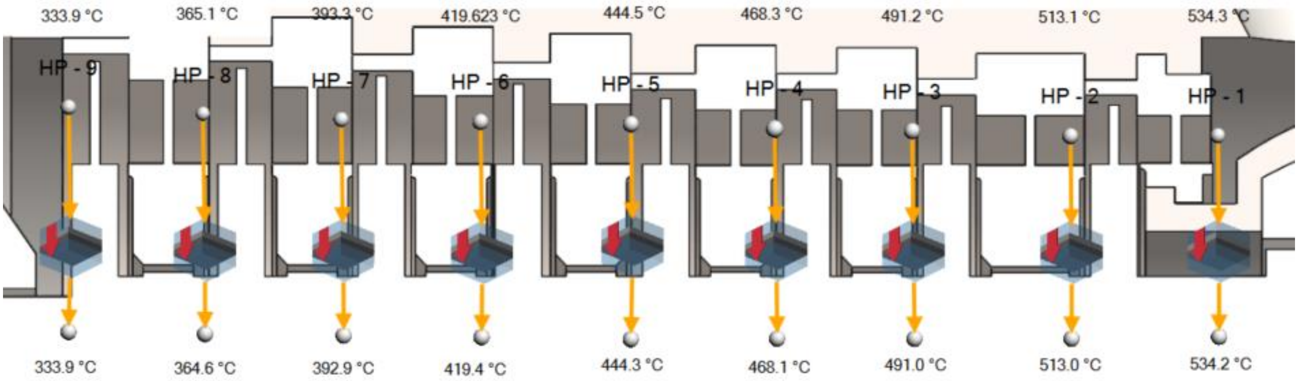

Figure 53: Rotor Heat Transfer Modelling for HP turbine

Further verification of this approach is shown in Appendix C

4.2.4 Cooling Flow Modelling

A feature of the IP turbine unit is the introduction of cooling steam flow at the root of the rotor, at the inlet of the unit. The steam admitted at this region is taken from the HP exhaust, before the steam enters the reheater flow path and is known as the IP cooling flow.

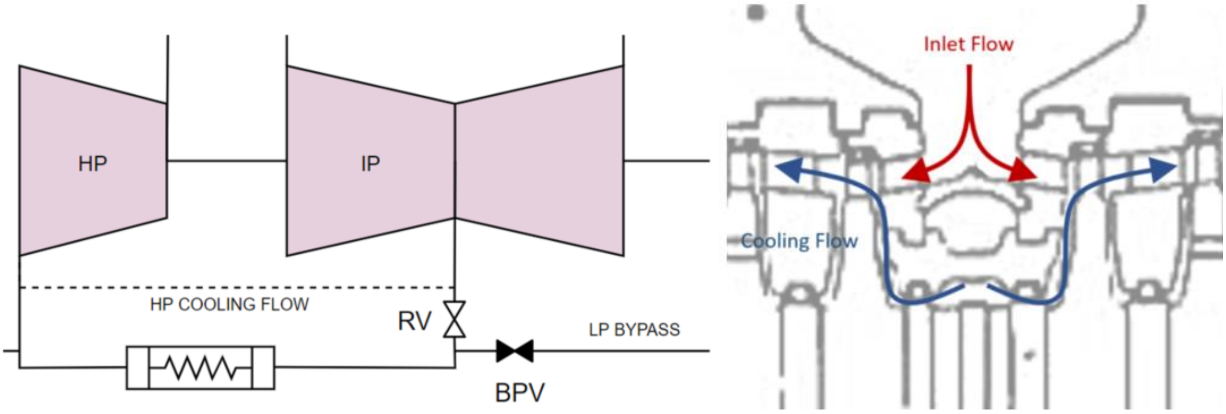

Figure 54: IP Cooling flow

The steam enters the IP cylinder through a small inlet pipe, passing over the enclosed surfaces of the first stage of the rotor. The cooling flow interacts with the heated steam leaving the first stage stator, shown in Figure 54. The result of this steam interaction serves as cooling of the enclosed rotor surfaces to prevent excessive heating of the steel, as well as the marginal lowering of the temperature of the steam entering the second turbine stage.

In modelling this cooling flow, as in the modelling of the extraction flow between the 4th and 5th stage, the establishment of an independent “turbines” connected in series was undertaken for the addition of flow. This meant that due to the additional flow introduced by the cooling flow, the first stage must be an independent “turbine” operating in series with the rest of the turbine stages. Figure 55, shows the independent first stage “turbine” in the inlet IPT schematic as well as the Flownex model of this inlet flow between the first and second stage of the IPT.

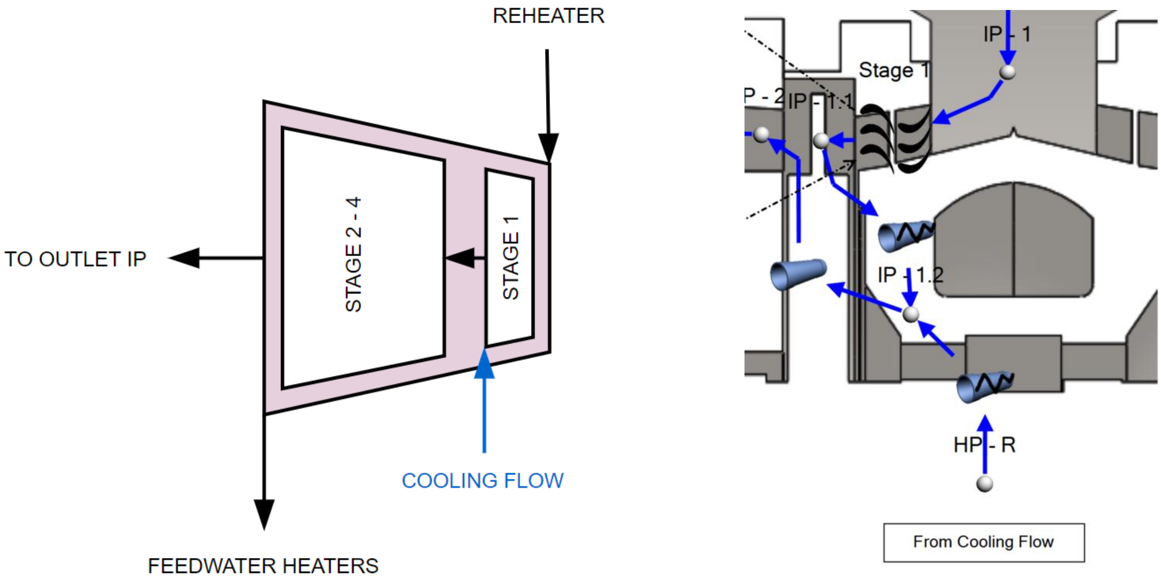

Figure 55: Inlet Turbine Cooling Flow Modelling

The flow path of the cooling flow was modelled as a series of flow resistors of nominally high flow admittances. Due to the inability to add the cooling flow between the stator and rotor of the first stage, arising from the inability to edit the Turbine Component itself, the cooling flow was modelled as entering the IP cylinder between the first and second stages. This adaptation was sound, due to the impulse blading present in the IPT such that the pressure remains constant across the rotor stage according to the Nozzle Analogy theory. This means that the upstream boundary condition of the cooling flow is the same as if defined between the stator and rotor. Despite the establishment of an independent “turbine” the first stage was still considered to be part of the inlet IP turbine during the calibration of the IP unit itself.

During the full load calibration of the IPT model the cooling flow was prescribed a zero mass flow boundary preventing flow through this passage, due to the flow being significantly smaller than the main steam flow through the turbine cylinder (approximately 2.3 kg/s). For the full load, case it was possible to calibrate the outer most flow resistor with a calibrated flow admittance of 3.026E-07 to achieve the expected full load cooling mass flow. There are no other flow control elements in the cooling flow supply line, hence the fixed flow admittance should produce the correct mass flow under off-design conditions.

4.3 Process Modelling

The detailed turbine models have quite a large amount of boundary connections to other locations in the Rankine cycle, mainly due to the inclusion of the various peripheral flows. Many of these parameters are not recorded on site, hence it is not possible to solve the detail turbine models during a full cold start transient. For this reason, a full process model of the entire Rankine cycle was developed in this study. This involved the inclusion of the reheater, a pseudo-Low-Pressure Turbine, condenser and feedwater heater train.

4.3.1 Reheater

The reheater acts as the primary interface between the HP and IP turbine, and was therefore modelled prior to the low load validation of the model. The inclusion of the reheater allowed for a comprehensive validation of both turbines, given the HP inlet temperature and pressure as well as the IP outlet pressure. The inclusion of the reheater resulted in the following configuration:

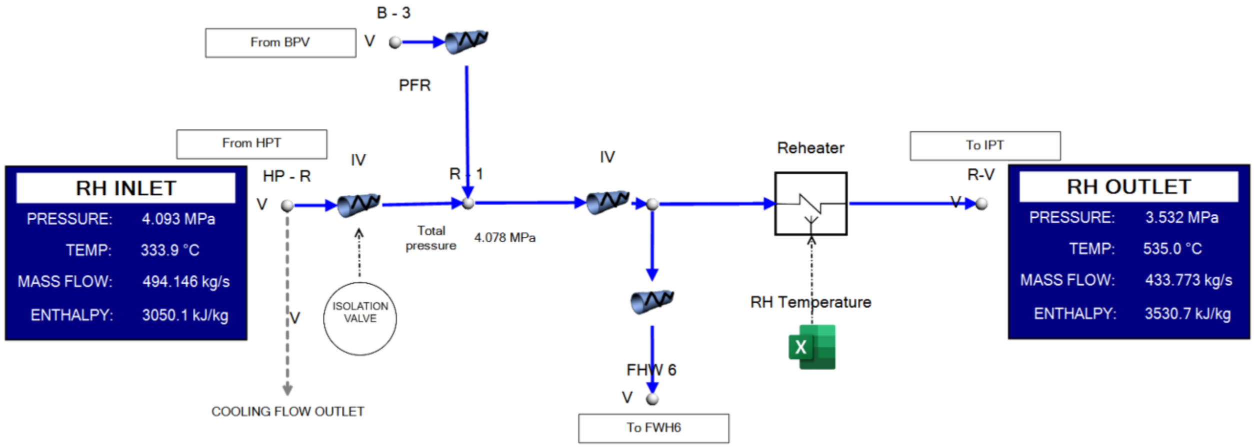

Figure 56: Reheater flow configuration

The reheater configuration features the end of the By-Pass Valve (BPV) flow, as well as a non-return valve at the HPT outlet which prevents steam reverse flow during HP By-Pass. The reheater is modelled using the ATProM Simple Reheater component.

The reheater component consists of three flow resistors: an inlet resistor which was calibrated to produce the desired pressure drop across the reheater; an outlet resister to deliver the calculated exit enthalpy in order to achieve the prescribed outlet temperature; and the spray flow inlet which was not included in this study as the spray water loads were not specified by the heat balance diagram and were assumed to be insignificant against the total mass flow through the reheater.

The exit enthalpy is achieved by the following energy equation, specifying the heat input delivered by the reheater:

$$\dot{Q}_{rh} = \dot{m}_{outlet} \cdot h_{outlet} - \left(\dot{m}_{inlet} \cdot h_{inlet} + \dot{m}_{inlet.spr} \cdot h_{inlet.spr} \right) \tag{4.25}$$

In the modelling of this component, the reported reheater exit temperature is prescribed by the CSV reader component, ensuring the correct IP Inlet steam conditions are met.

4.3.2 Low Pressure Pseudo-Turbine

Due to the absence of a value for IP exhaust pressure in the reported data from the candidate unit, it was necessary to include a Low Pressure (LP) Pseudo-Turbine with a prescribed condenser pressure. The pressure was reported in the plant data provided. The internally developed, ATProM Simple Turbine component was used to perform the role of capturing the pressure drop across the LP unit and capture the mass flow to the low-pressure Feedwater Heaters. In turn it resulted in defining the IP Exhaust pressure to enable the upstream solving of the HP and IP turbines.

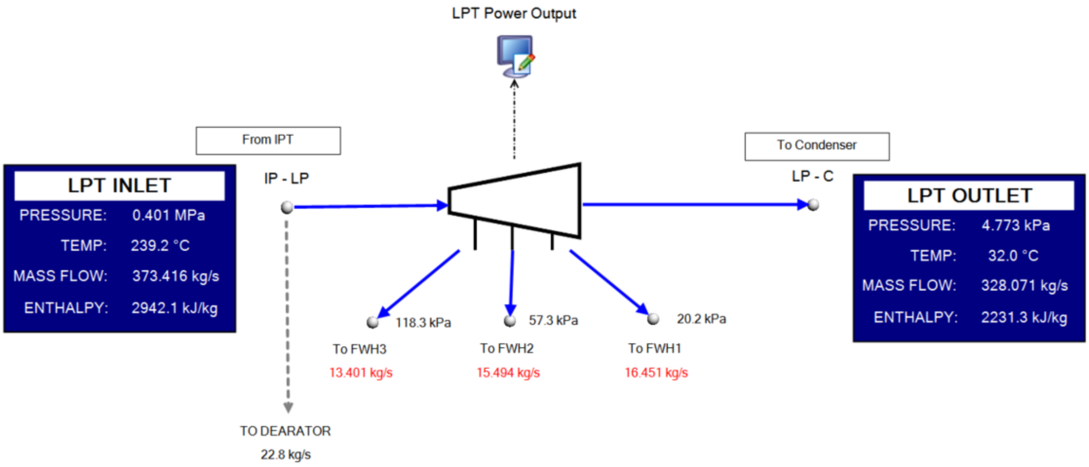

Figure 57: Low Pressure Turbine Model

The Simple Turbine component is defined by the full load characteristics of the LP turbine, allowing for the solving of load cases lower than full load relative to the sensed inlet mass flow entering the unit. In the candidate unit, as shown in Figure 27, two LP turbines are present. However, for a reduction in modelling complexity, a single pseudo-turbine was used with the condenser pressure being prescribed by a single set of on-site condenser pressures within the reported data.

The Simple Turbine components additionally allowed for the prescription of the bled steam lines leaving through the axial path of the steam with the respective full load outlet pressures and mass flows. Figure 58 shows the input window available to a user of the Simple Turbine components as well as the high level parameter set of the LP turbine used in this study.

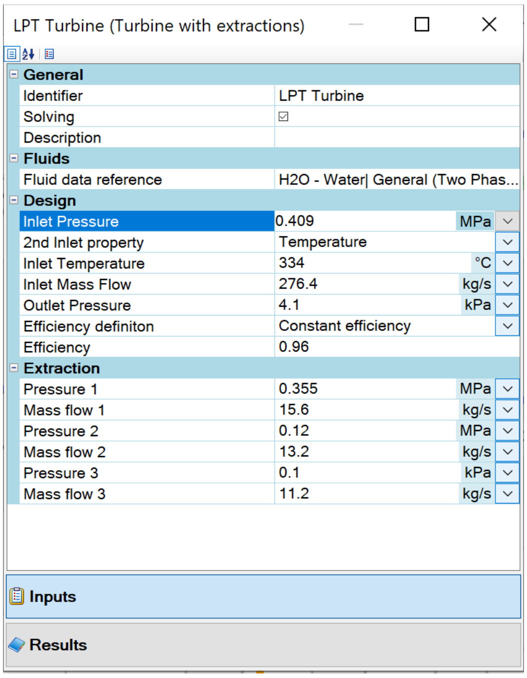
LPT Turbine (Turbine with extractions)

General		
Identifier	LPT Turbine	
Solving	☑	
Description		
Fluids		
Fluid data reference	H2O - Water| General (Two Phas...	
Design		
Inlet Pressure	0.409	MPa
2nd Inlet property	Temperature	
Inlet Temperature	334	°C
Inlet Mass Flow	276.4	kg/s
Outlet Pressure	4.1	kPa
Efficiency definiton	Constant efficiency	
Efficiency	0.96	
Extraction		
Pressure 1	0.355	MPa
Mass flow 1	15.6	kg/s
Pressure 2	0.12	MPa
Mass flow 2	13.2	kg/s
Pressure 3	0.1	kPa
Mass flow 3	11.2	kg/s

Figure 58: Input window for LP Turbine component

4.3.3 Condenser

The outlet of the low-pressure turbine is connected to the condenser, which acts as a known boundary condition for the Rankine cycle. The condenser was modelled using the Simple Condenser component from the ATProM library. The component requires a user defined pressure and, from the available mass flow, solves for the energy extracted by the condenser in cooling the steam to a saturated liquid by the following energy equation:

$$Q = \dot{m} \cdot (h_{ex} - h_{in}) \tag{4.26}$$

The condenser pressure is prescribed by a CSV reader component, as seen in Figure 59.

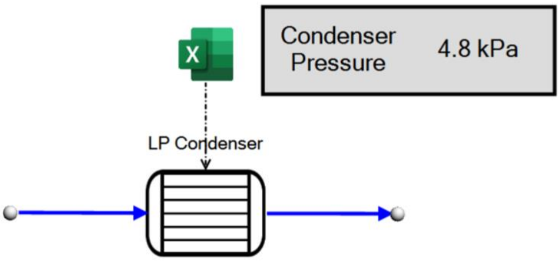

Figure 59: Condenser configuration

4.3.4 Feedwater Heaters

The modelling of the feedwater heaters is important to capture the leak flows through the gland seals of each turbine as well as the bled steam through various regions of the turbine unit itself. The development of the feedwater train chain was performed using the ATProM library components and was modelled to replicate the plant layout shown in the heat balance diagrams. Figure 60 shows a schematic of the feedwater train, which was replicated in the turbine model.

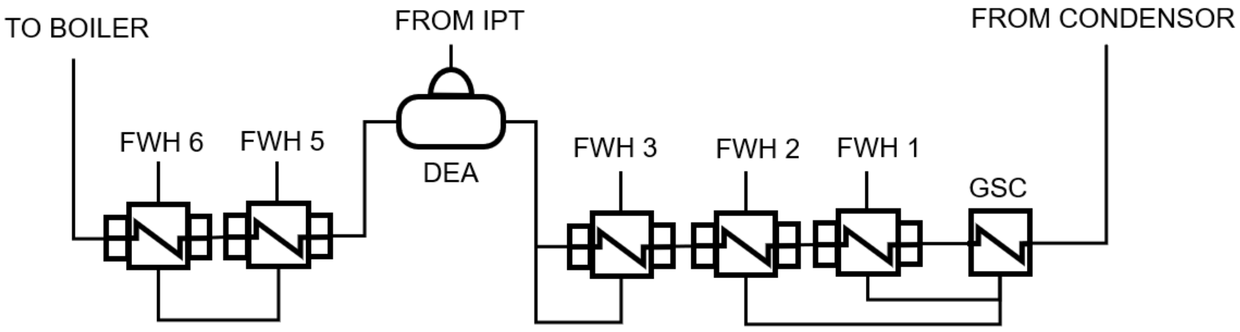

Figure 60: Feedwater train for Candidate Turbine Unit

Whilst the complete modelling and validation of the entire Feedwater Chain fell outside of the scope of this study, functionality of the Feedwater Heaters was of particular importance to define the pressure boundaries at each gland seal and extraction point. The methodology used to model a representative Feedwater Heater is presented below with one of the high-pressure Feedwater Heater 5, illustrated by Figure 61 below.

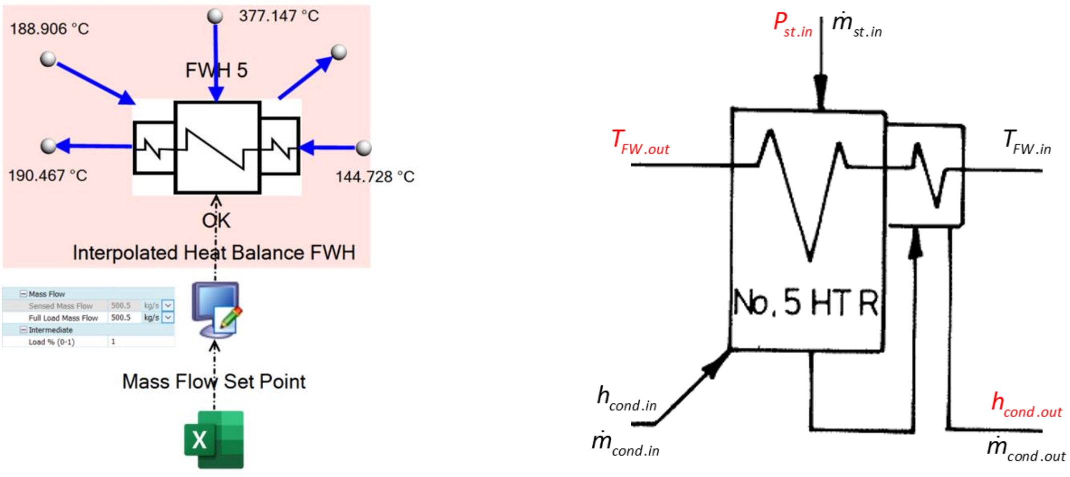

Mass Flow
Sensed Mass Flow 500.5 kg/s
Full Load Mass Flow 500.5 kg/s
Intermediate
Load % (0-1) 1

(i)

(ii)

Figure 61: (i) Feedwater Heater Train model (ii) FWH5 from Heat Balance Diagram

The feedwater train makes use of the Simple Feedheater component from the ATProM library. The Feedheater component enforces a user-specified Terminal Temperature Difference (TTD) and Sub-Cooling (SC) value on the feedwater and condensate, respectively. Given the prescribed TTD and SC values the component calculates the appropriate steam mass flow required to satisfy the energy conservation. Both the TTD and SC values change as a function of unit load (%) and therefore, from the Heat Balance diagrams, the TTD and SC values were derived.

The TTD and SC values of all of the Feedwater Heaters were determined for the 100%, 80%, 60% and 45% load cases. An interpolated FWH parameter script was developed, seen in Figure 61(i). The script accepted the prescribed mass flow of the unit and compared this mass flow to the maximum rated mass flow of the unit, returning a percentage load.

$$Load = \frac{\dot{m}_{sensed}}{\dot{m}_{\max}} \qquad 4.27$$

This percentage load was used to linearly interpolate for the representative TTD and SC values for the given load case, which were then prescribed to the Feedheater for the current time step. Figure 62 shows the interpolation of the TTD and SC values from an arbitrary load case, X.

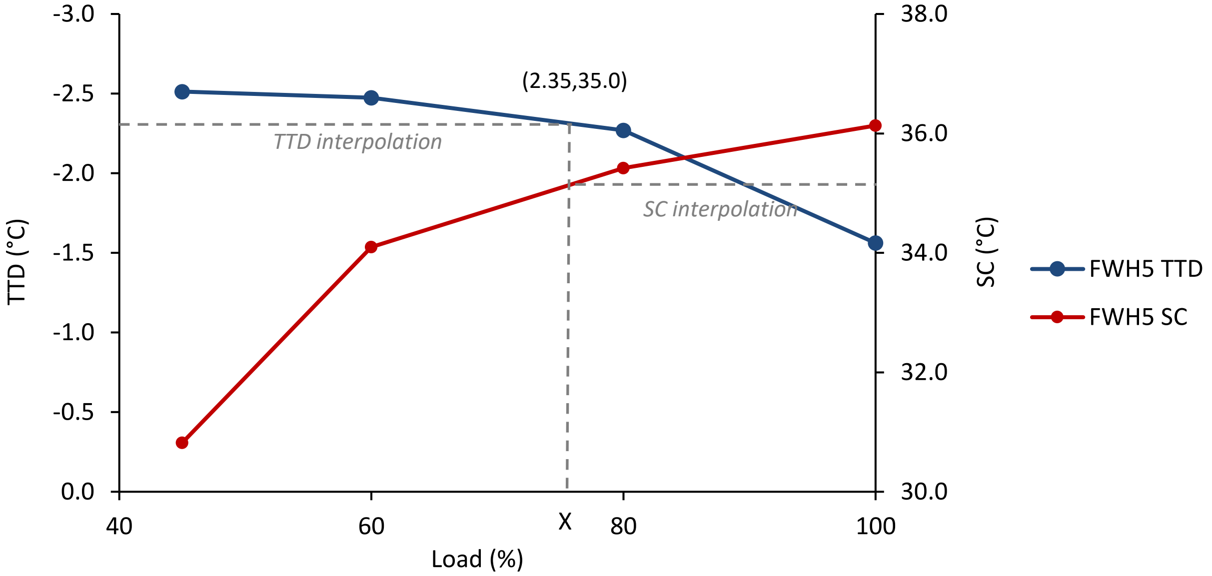

Figure 62: TTD & SC Linear Interpolation for FWH5

The predominant parameters which the component solves for are the three mass flows: Steam as well as the Inlet and Outlet Condensate flows. In order to verify the validity of the above modelling methodology, the inlet steam mass flows was recorded and compared to that of the heat balance data.

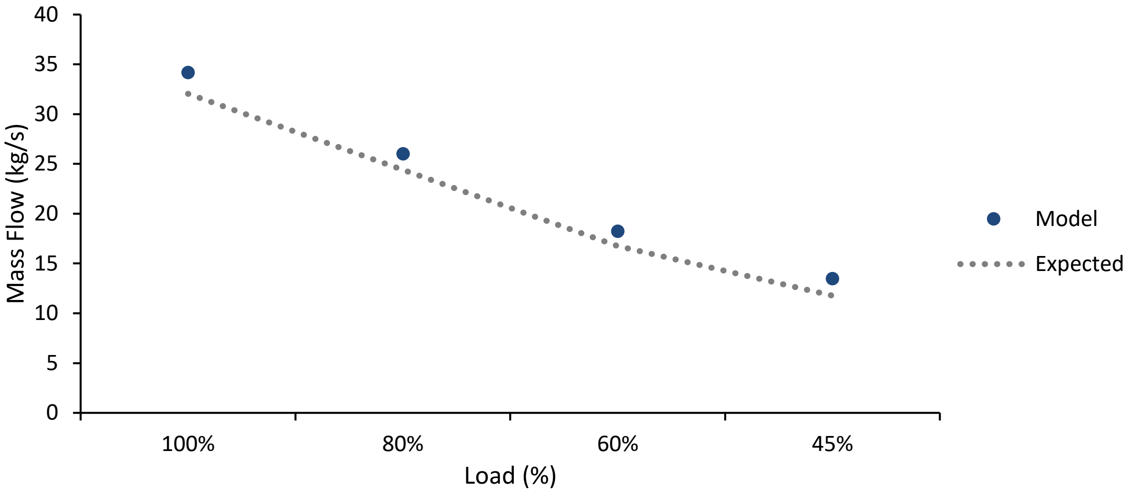

Figure 63: FWH5 Low Load Validation

The above figure shows that the approach taken properly accounts for the variable behaviour of the Feedwater Heaters at different loads. The transient validity of the interpolated approach will be discussed during the Load Change validation in later chapters.

4.4 Turbine model transient control

In view of the intention to use the Integrated turbine model in the modelling of transient operations from an operational Eskom plant, it was necessary to develop a way to apply reported conditions as boundary conditions to the model, and henceforth to allow the model to solve for the nodes between these boundary conditions. The true power of such models is the definition of as few boundary conditions as possible to increase the validity of the results and consistency of the internal boundary conditions of the established model [7]. The interface between the turbine model and the reported boundaries is shown in Figure 64.

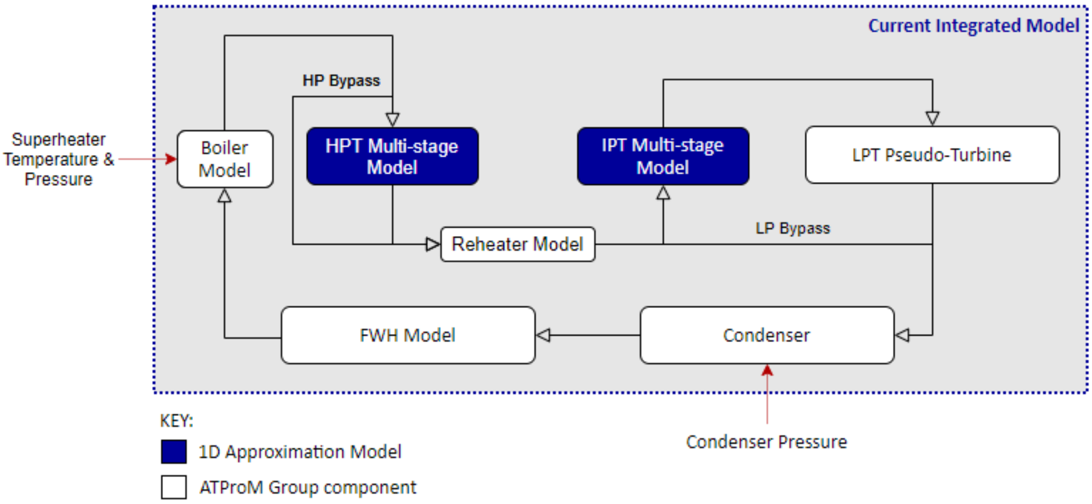

Figure 64: Reported Plant Data interface

The predominant boundary conditions of interest in controlling the model were the following:

- Superheater temperature and pressure
- Condenser Pressure
- Rotor Speed
- Reheater Exit Temperature
- Boiler Mass Flow Rate

From the plant data secured from the candidate unit a simplified CSV file was created for each of the operating procedures to act as input parameters to the model. An example of the format of this CSV file is shown in Figure 65.

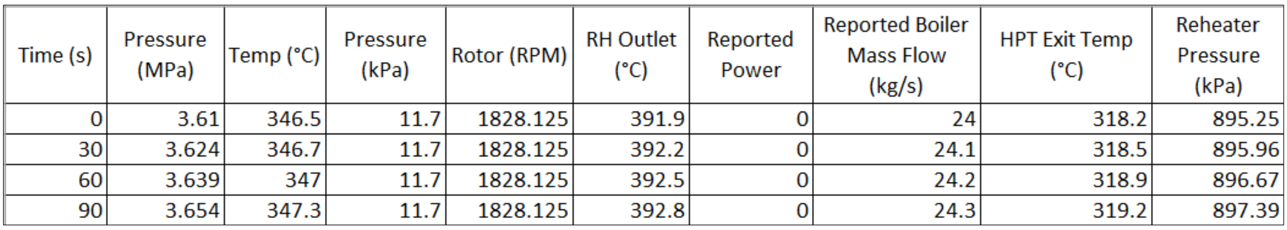

Time (s)	Pressure (MPa)	Temp (°C)	Pressure (kPa)	Rotor (RPM)	RH Outlet (°C)	Reported Power	Reported Boiler Mass Flow (kg/s)	HPT Exit Temp (°C)	Reheater Pressure (kPa)
0	3.61	346.5	11.7	1828.125	391.9	0	24	318.2	895.25
30	3.624	346.7	11.7	1828.125	392.2	0	24.1	318.5	895.96
60	3.639	347	11.7	1828.125	392.5	0	24.2	318.9	896.67
90	3.654	347.3	11.7	1828.125	392.8	0	24.3	319.2	897.39

Figure 65: Input CSV file

The boundary conditions detailed in the CSV are applied through the use of the CSV Reader component in Flownex SE. The CSV file also featured reported data from the plant which was used to validate the model outputs against measured parameters, such as Reported Power Output, HPT Exit Temperature and Reheater Pressure. The application of the Reported Boiler Mass Flow parameter was particularly important to the functioning of the model.

As seen in Figure 66, below, the output of the CSV reader component is prescribed as an input to the Steady State Controller component, marked MASS REG 01. The Steady State Controller component reads the upstream mass flow and regulates the flow to match the prescribed mass flow by adjusting the valve opening, between 0 and 1.

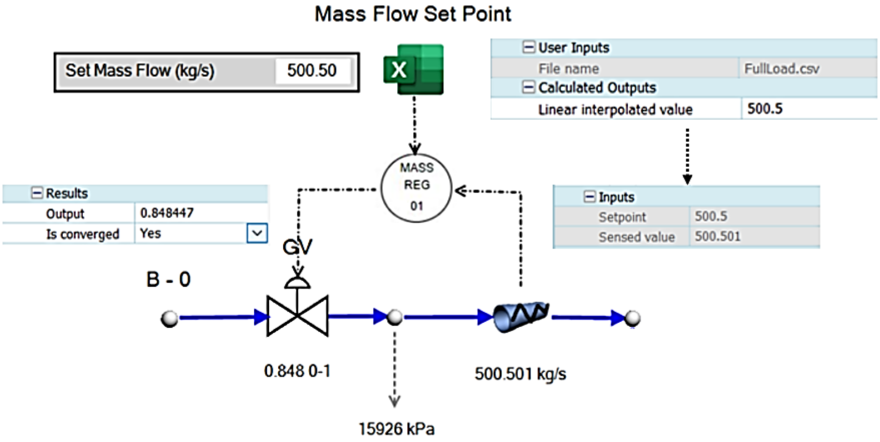

Set Mass Flow (kg/s) 500.50

User Inputs
File name FullLoad.csv
Calculated Outputs
Linear interpolated value 500.5

Results
Output 0.848447
Is converged Yes

Inputs
Setpoint 500.5
Sensed value 500.501

Figure 66: CSV Reader applied to HPT governing valve model.

In the subsequent work of producing a representative start-up transient simulation, the Flownex model was adapted to control the turning ON and OFF of the Feedwater Heater train. This was controlled by the use of the Flownex Configuration Actions, as a function of elapsed time in the start-up procedure. A control methodology is detailed below, in

Table 12, demonstrates the various means of control used within the 1D Turbine model in order to perform a representative Cold Start-Up procedure.

Table 12: Control methodology for Transient Turbine Model

Control Method	**Quantity**
CSV	Boiler Pressure (MPa) Boiler Temperature (°C) Condenser Pressure (kPa) Boiler Mass Flow (kg/s) Reheater Pressure (kPa) Rotor Speed (rpm)
Feedback Loop	Boiler Mass Flow - to match reported data (kg/s)
Flownex Configuration Actions	Feedwater Heater Operation (ON or OFF)
Flownex Parameter Table	HPT ESV Admittance (0 or 1) IPT ESV Admittance (0 or 1)

Given the number of control parameters, a single parameter table was created to control the assignment of all of the control boundary conditions. This was named the ‘Model Manager’. The parameter table allowed for the model to be controlled by user defined inputs which would execute the combination of variable changes to perform the desired operation. A refinement of this parameter table resulted in the entire model being controlled by two inputs:

1. Turbine Condition: Prescribing the loss coefficients to be applied to the turbine stages, affecting the enthalpy drop across the HP and IP units
2. Operation Sequence: Prescribing the operation, whether a full load steady state simulation or a full Cold Start-Up simulation.

The establishment of such a parameter table greatly reduced the workload of investigators and allowed for various simulations to be performed within close succession. Figure 67, shows the layout and functionality of the Model Manager used in this study.

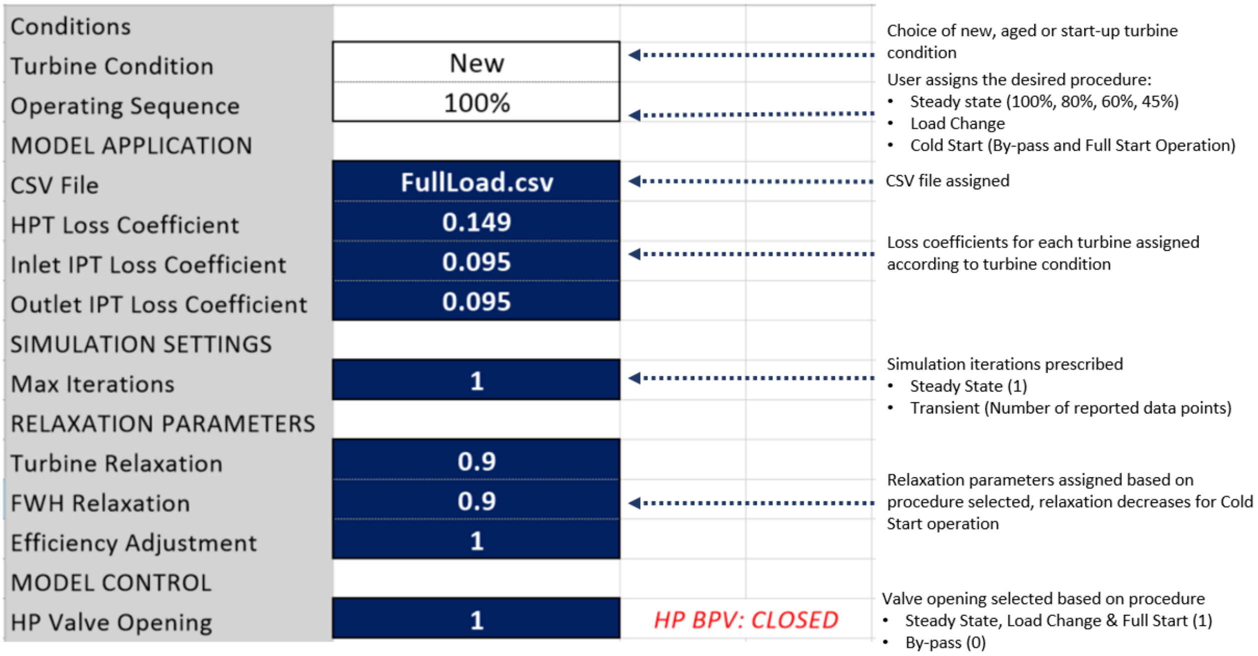

Conditions		
Turbine Condition	New	
Operating Sequence	100%	
MODEL APPLICATION		
CSV File	FullLoad.csv	
HPT Loss Coefficient	0.149	
Inlet IPT Loss Coefficient	0.095	
Outlet IPT Loss Coefficient	0.095	
SIMULATION SETTINGS		
Max Iterations	1	
RELAXATION PARAMETERS		
Turbine Relaxation	0.9	
FWH Relaxation	0.9	
Efficiency Adjustment	1	
MODEL CONTROL		
HP Valve Opening	1	HP BPV: CLOSED

Choice of new, aged or start-up turbine condition

User assigns the desired procedure:
- Steady state (100%, 80%, 60%, 45%)
- Load Change
- Cold Start (By-pass and Full Start Operation)

CSV file assigned

Loss coefficients for each turbine assigned according to turbine condition

Simulation iterations prescribed
- Steady State (1)
- Transient (Number of reported data points)

Relaxation parameters assigned based on procedure selected, relaxation decreases for Cold Start operation

Valve opening selected based on procedure
- Steady State, Load Change & Full Start (1)
- By-pass (0)

Figure 67: Model Manager Parameter Table

The assigned values, highlighted in navy blue in the Model Manager, served as input parameters to the turbine model itself. The parameters made use of IF statement coding to take the user input and define the appropriate boundary condition to the connected component parameter. From this relatively simple set of parameters, one was able to control the entire 1D Turbine Model used in this study.

4.5 Model validation

Validation of the developed 1D turbine model was done systematically from simple to more complex scenarios. The most simple is just a steady state solution at lower loads, while the most complex scenario is to see how well the model can predict the transient behaviour during a cold start. During each validation, some further refinements or adjustments had to be made in order to achieve the desired confidence in the complete model. The incremental steps will be elaborated next.

4.5.1 Low Load Validation

The full load, steady state data was used to calibrate the model. A Low Load Validation was carried out using the calibrated 1D Turbine model against the heat balance diagram values. The heat balance diagram was used to extract the designed boundary conditions needed for model operation, prescribing the parameters for the 45, 60, 80 and 100% load cases. The value of this validation was mostly academic, as in the work of Clarke [2] and Fuls [1] the use of the nozzle analogy had already confirmed the ability of such a model to accurately predict low load operation. The low load validation, however, also assisted in operational validation in the sense of testing the control methods prescribing the various boundary conditions.

Three internal locations were chosen as validation points for the model, shown in Figure 68:

- HP Turbine Outlet
- IP Turbine FWH5 Extraction Outlet
- IP Turbine Outlet

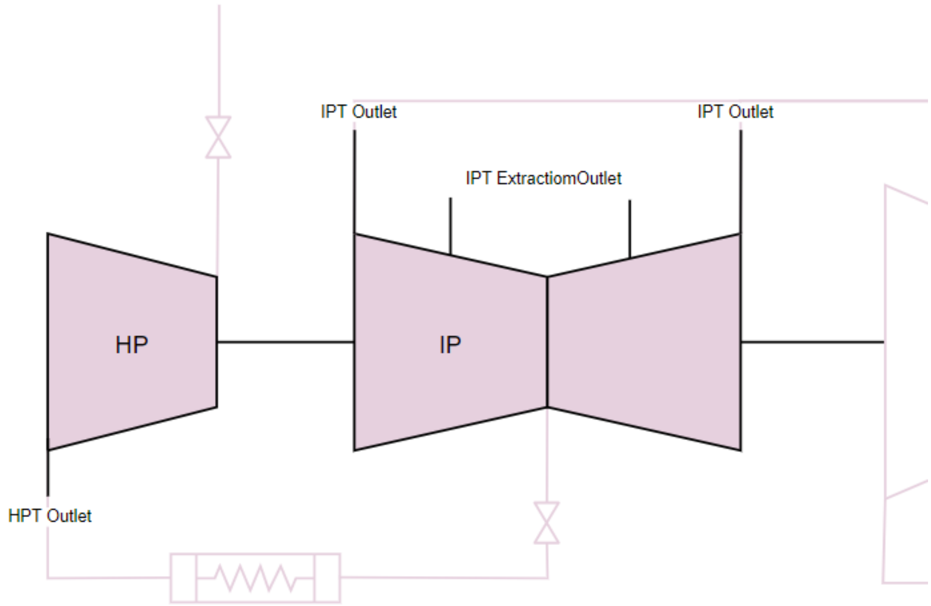

Figure 68: Validation Locations used for Model Validation

The pressure, enthalpy, temperature, and mass flows were assessed at each point and compared to the expected heat balance values. Below, Figure 69, shows the pressure validation of the model at low loads.

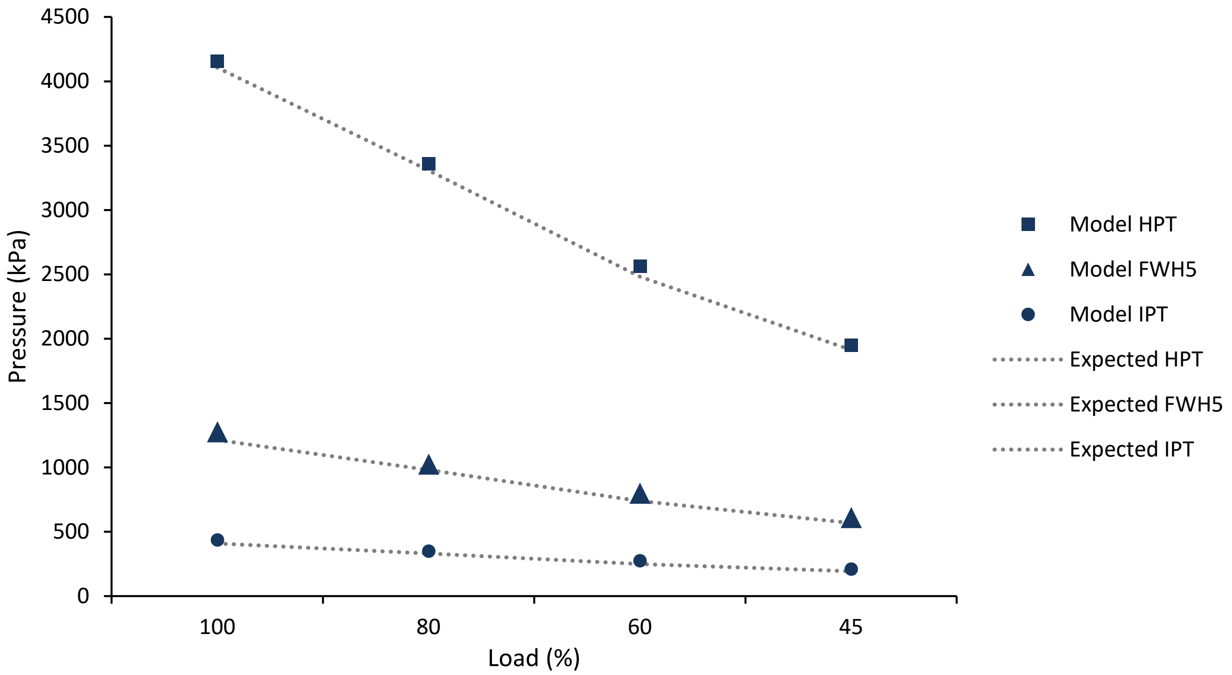

Figure 69: Pressure Results of Low Load Validation

From the above pressure validation, it was evident that there is strong agreement between the model and the expected pressure values from the heat balance. In conjunction with the pressure, the enthalpy at the validation points were also captured, shown below in Figure 70.

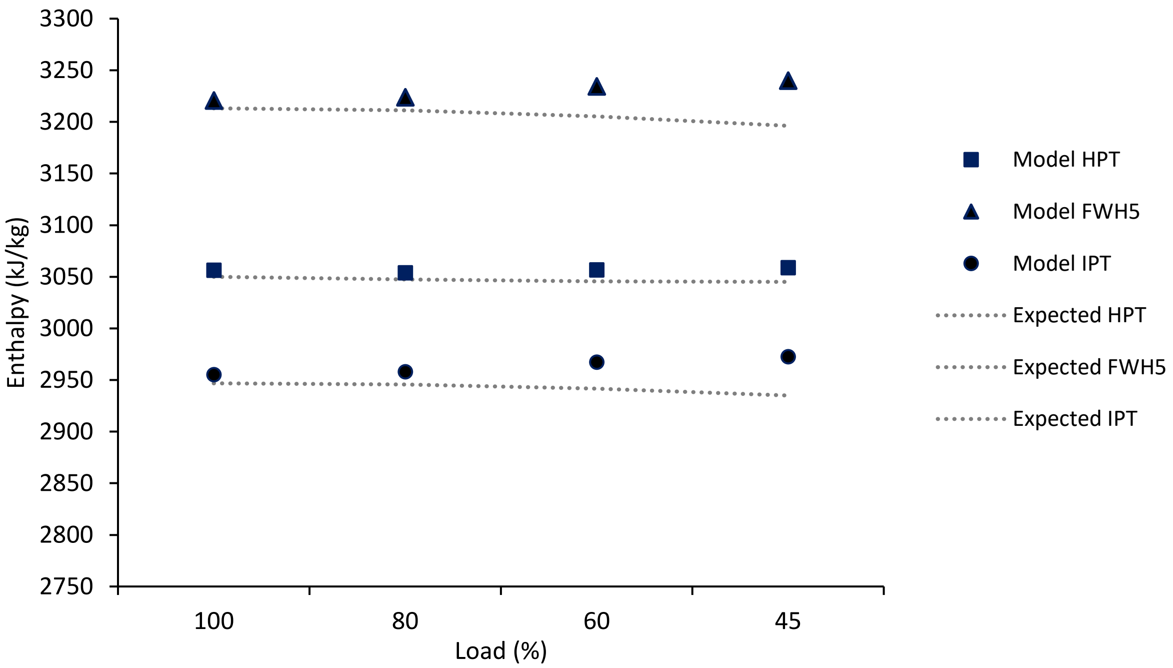

Figure 70: Enthalpy Results of Low Load Validation

The validation of the enthalpy appears to show greater deviation from the expected values, compared to the previous pressure validation. This is attributed to the difference in calculating enthalpy using 1997 steam formulation as opposed to the heat balance diagram values which were developed in the 1960's. Despite this the above validation can be deemed successful. The significance of these results is that these variables were all enclosed in the model with substantial solving taking place between the validation point and the nearest boundary condition.

In order to fully comprehend the validity of the model results, an error analysis was performed on all of the quantities, excluding boundary conditions. The best way of representing this is in an Error Box Plot, demonstrating the distribution of the errors within the model around the minimum, maximum and average. The error box plot of the model during the low load validation is captured in Figure 71, below:

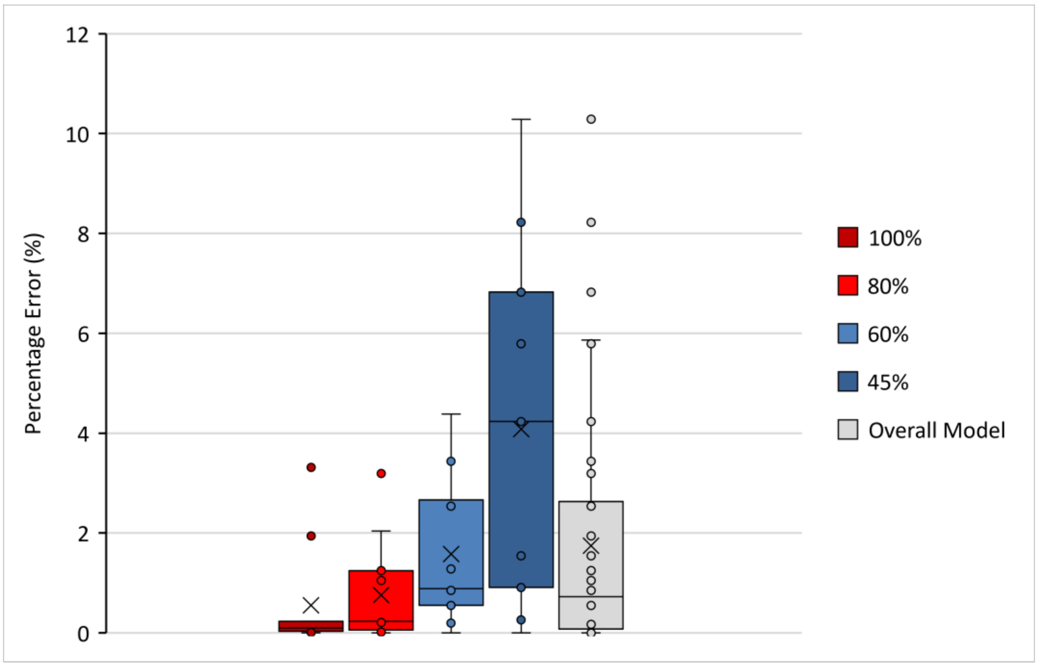

Figure 71: Box Plot showing Low Load validation errors.

The error box plot shows that the average error as well as the distribution of the error increases with decreasing load, as demonstrated in Table 13. Despite this error trend, the agreement of the model to within 90% accuracy is a substantial indication of the ability of the model to perform at the various design loads from heat balance specifications.

Table 13: Average Error vs Load for Low Load Validation

Load	**100%**	**80%**	**60%**	**45%**
Average Error (%)	0.550	0.759	1.581	4.084

Since one of the primary objectives is to achieve a computationally inexpensive method, it is worth noting that it takes approximately 150 iterations to converge to a solution, which is about 10s of solving time on a Dell G3 15 PC, running an I7 processor. One can expect a faster solution between successive time-steps during a transient simulation, as the initial condition is typically close to the new solution for small time steps.

4.5.2 Transient Load Change Validation

With reasonable confidence in the steady state solution of the model, the validation of the model turned to the application of two transient events observed on site: unit load change and a full cold start, the first of which is dealt with in this section.

In the data received from the candidate unit, a load change was observed in the unit lifting its output from nominally 400MW to 500MW in approximately 25 minutes shown in in Figure 72, below.

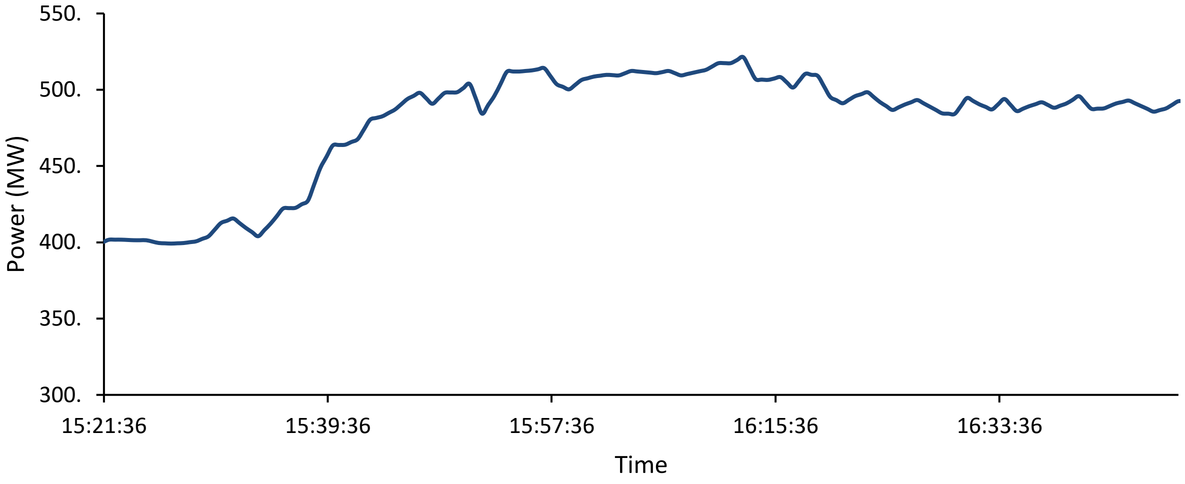

Figure 72: Gross Unit Power Output during Load Change.

The boundary conditions of the load change were applied at the boundaries of the Flownex model using the same loss coefficients from the calibrated model obtained using the heat balance diagrams. Two validation parameters were selected:

- HPT Exhaust Temperature
- Gross Unit Power Output

These values were selected due to the previous validation, according to the heat balance diagram, but also mostly due to the availability of these parameters from the reported data collected. The HPT exhaust temperature result is shown in Figure 73.

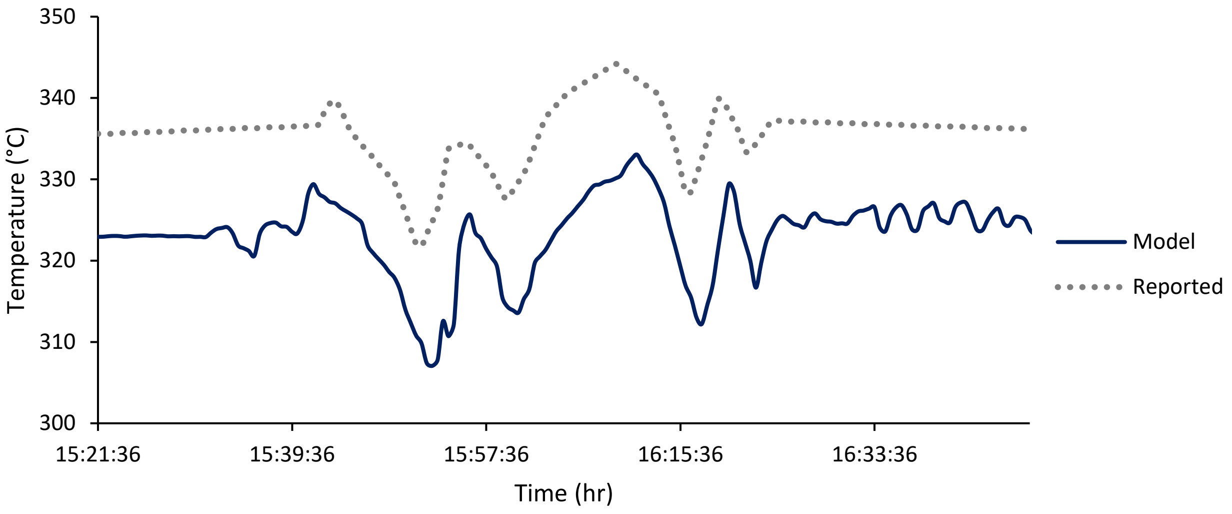

Figure 73: HPT Outlet Temperature during Load Change.

This result suggested that the modelled unit was extracting too much energy across the HPT. It was hypothesised that there were more blade losses which needed to be accounted for in the turbine stage model, due to aging of the unit after approximately 25 years of operation. The stator loss coefficients (ζ_S), were iteratively increased to represent an "aged" turbine condition which better match the recorded data.

Whereas the initial calibration of the model saw loss coefficients of approximately 0.15 and 0.10 for the HP and IP models respectively, the "aged" coefficients were approximately 0.25 and 0.18 for the HP and IP models, respectively. Using the aged loss coefficients the transient load change simulation run produced temperature and power results shown in Figure 74 and Figure 75.

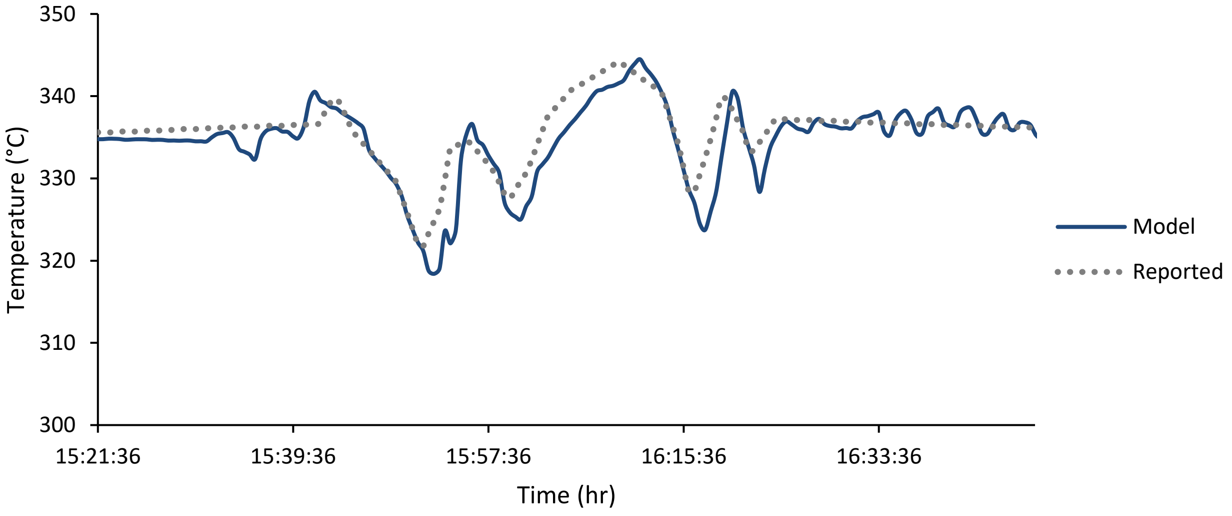

Figure 74: HPT "Aged" Outlet Temperature during Load Change

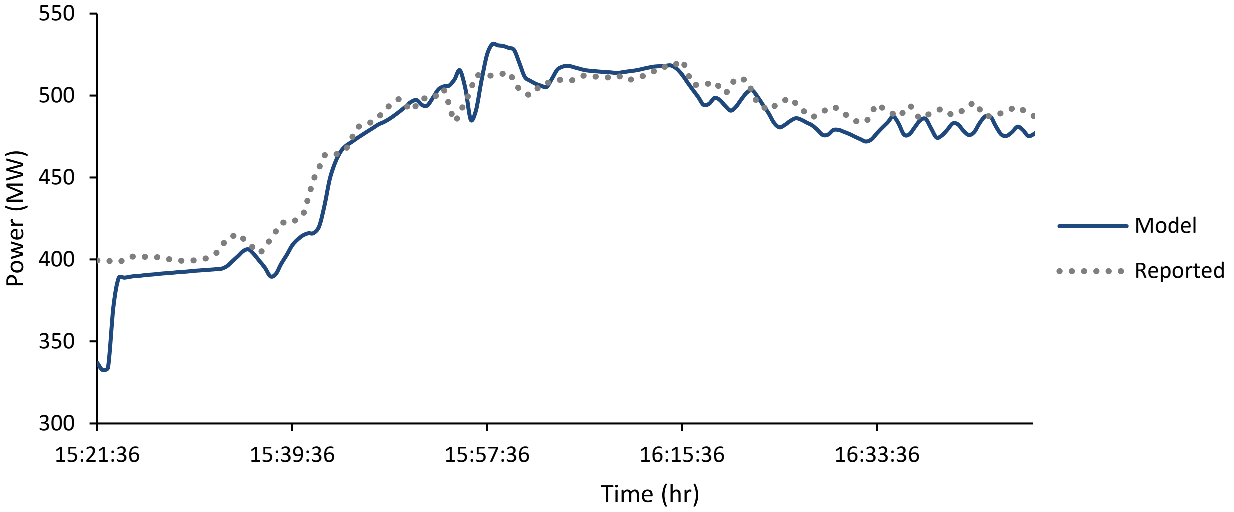

Figure 75: Gross Unit Power Output of Aged Turbine Model

As in the low load validation, the error across the two validating parameters was captured in an error box plot. It is important to consider that the load change simulation was a purely off-design simulation as the model was performing a simulation for load conditions falling outside of those defined by the heat balance diagram, thus this simulation also tested the validity of the linear interpolation assumptions made in certain components within the Turbine Process model.

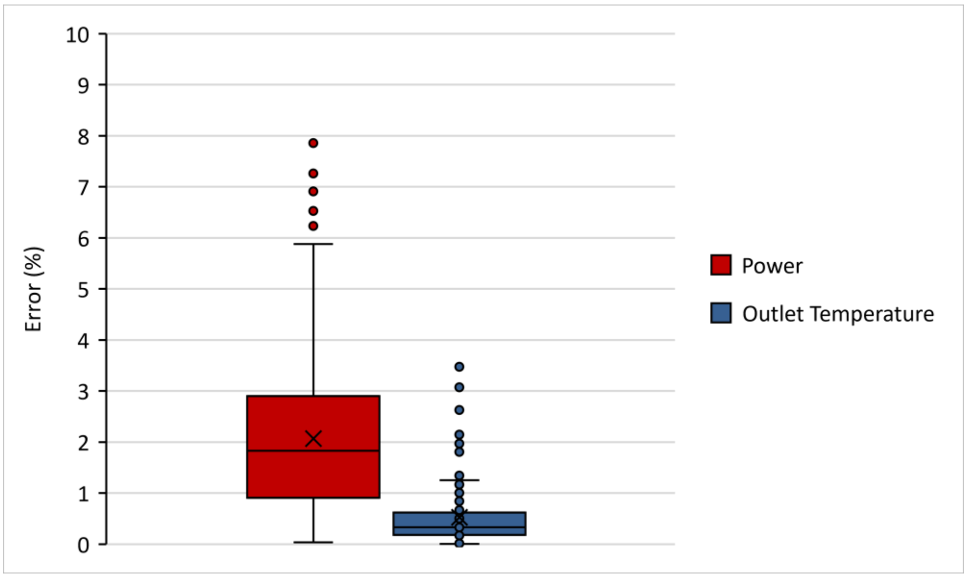

Figure 76: Error Box Plot for transient load change

Despite these assumptions, the error box plot indicates a strong agreement of the modelled data against the reported data, with the error present in the power output prediction within 90% accurate and the outlet temperature within 98% accurate. Of greater significance, given that the 1D Turbine model is to provide the thermal boundary conditions to the 3D FEA model, the high accuracy in the outlet temperature adds confidence in the thermal boundaries produced by the 1D model. If one were to quantify the maximum error, the error for both quantities amounts to 4.36°C and 35.1 MW respectively, which, given the level of simplification applied in the model, is more than acceptable.

Once again, considering the computational expense of the model, the model was found to perform at approximately 1.5 times faster than real time using a sampling time equal to that measured on site (30s). The ability to generate accurate thermal boundary conditions, in a significantly shorter amount of time than that of real-time was a substantial finding during this study and marked the successful development of a feasible modelling methodology. Whilst larger time steps of greater than 30s could be selected to increase solving time, as illustrated in Figure 77, one would see a reduction in the computational accuracy of the model compared to the reported data with arguably a marginal improvement in the overall solving time. Figure 77, shows the boiler outlet steam temperature boundary condition for increasing time step sizes and the resulting reduction in accuracy against the reported plant data.

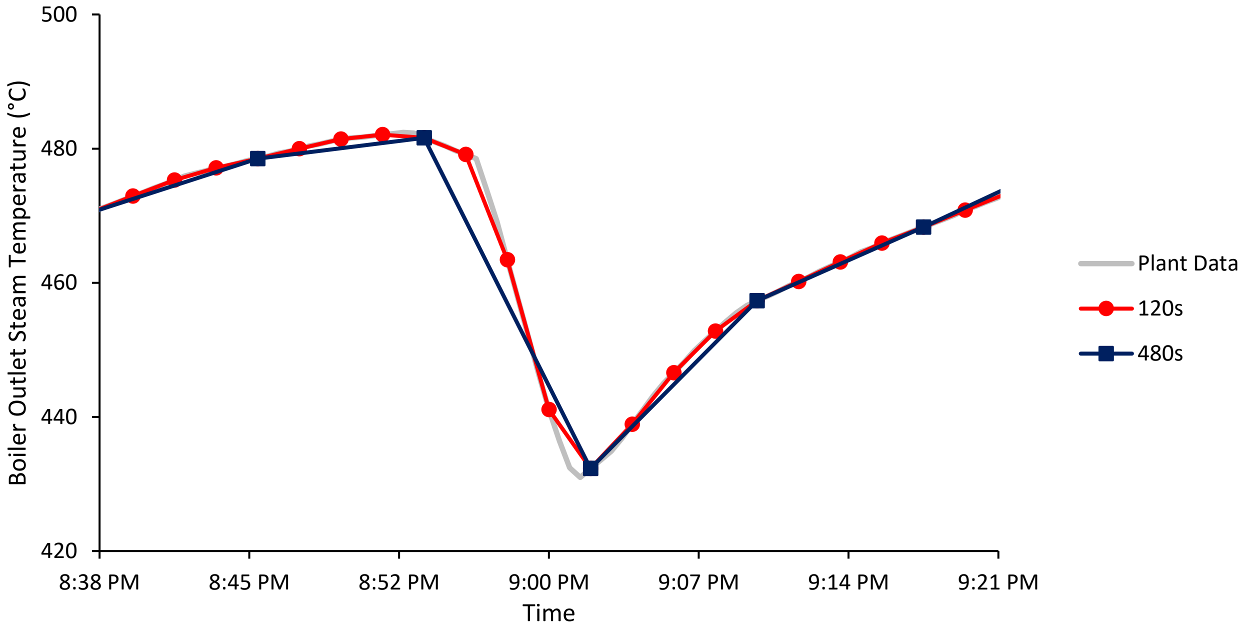

Figure 77: Reduction in boundary condition accuracy due to increased time step size

A concluding remark from Figure 77, is that the reduction in computational expense, as in choosing larger time steps, should always be balanced against the unavoidable reduction in boundary condition accuracy. In the context of this study, in which the transient inertial response of turbine components is of importance, such a reduction in accuracy could jeopardize the possible findings of such a modelling methodology. As such the time step size, close to that of the reported plant data (30s) was used during this study.

4.5.3 Cold Start-up Validation

Following the steady state and transient validation of the 1D Turbine model against both heat balance and reported data, a full Cold Start-Up was attempted. Using the boundary conditions of the representative Cold Start-Up profile, in Figure 31, an initial validation was carried out.

As in the load change validation, the two parameters monitored was the HPT exhaust temperature and unit gross power output. Based on the results of the load change simulation some further adjustments to the loss coefficients were expected. It was expected that as the turbine unit operated at an increasingly lower load condition that the flow characteristics through the turbine stages would change as well. With the reduced mass flow through both the HP and IP units, the effects of blade vortex effect, blade leakage and incidence losses would change – all impacting the loss coefficients meant to represent the collective effect of all these losses. The degree to which these losses change is difficult to quantify and fell outside of the scope of this study. It was therefore decided to identify suitable loss coefficients that would reasonably represent the complete transient.

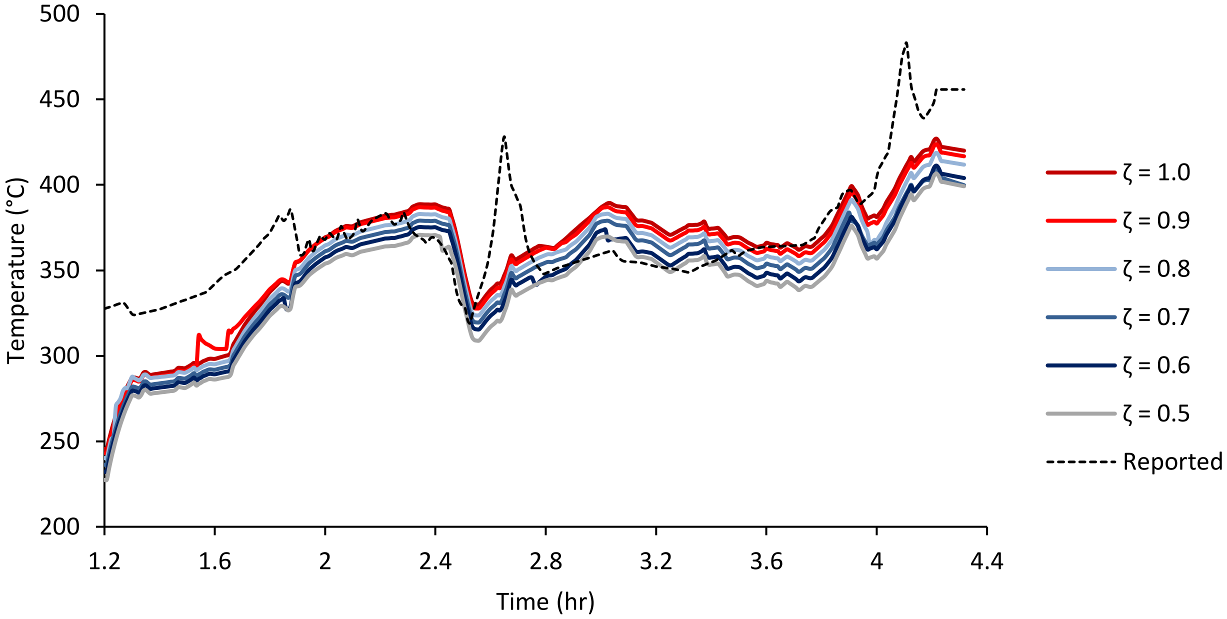

Figure 78: Varying Loss Coefficient values for Cold Start Procedure

Figure 78 compares a range of loss coefficients with the plant data. The graph shows that a loss coefficient of between 0.8 and 0.9 shows the greatest agreement to the reported values between 1.9 and 2.4 hours and again between 3.25 and 3.75 hours. However, an agreement can be found at a loss coefficient of 0.5 between 1.5 and 2.25 hours.

A hybrid solution was proposed whereby the loss coefficients would change as a function of time in the start-up boundary conditions. However, this greatly compromised elegance of the turbine modelling methodology as it would presume that the outlet conditions, like the HPT exhaust temperature, would be known when modelling – which is not always the case, especially in extreme off design scenarios. This could be considered as excessive tuning to achieve a desired output. Therefore, it was rather decided that a loss coefficient that showed the smallest error across the entire start-up procedure would be selected for the final cold start-up simulation. This loss coefficient was such that $\zeta = 0.9$, meaning that most of the kinetic energy available for work extraction is lost. This may not be entirely invalid, as no significant power is expected from the turbine during the startup.

Using the selected representative loss coefficient, the HPT Exhaust Temperatures against the reported data is shown in Figure 79 below.

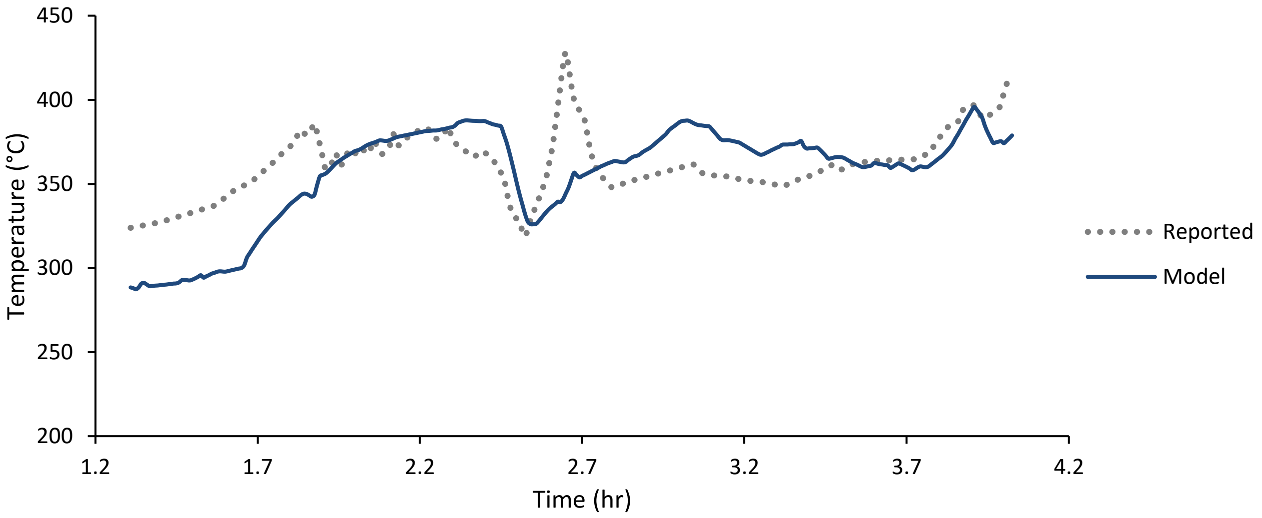

Figure 79: Modelled HPT Exhaust Temperature during Cold Start-up

From the above graph one can deduce that the model produces a satisfactory result in parts of the cold start-up. The deviation of the model from the reported values can be attributed to a number of factors. Firstly, the deviation in the first 45 minutes of the simulation is a period which proved difficult to model in a one-dimensional sense, as it marks the period during which steam flow is first transferred from the HP by-pass system to the HP cylinder. It would stand to reason that there will be a period where both the main throttle valve and the by-pass valve will be in partially open positions. This operational state results in exhaust steam temperatures observed which are a function of both the predicted main steam exhaust temperature as well as the inlet steam temperature. Secondly, an added limitation of the modelling approach taken is the ability to assign a single loss coefficient within the turbine stage model when in fact it is far more likely that each turbine stage will experience a different array of loss coefficient values during the course of a start-up. As demonstrated in the initial validation of the modelling approach in earlier chapters, it would be possible to argue that a linear combination of different loss coefficient conditions would likely yield a result which replicates the reported exhaust steam temperatures more closely. Despite this the majority of the start-up procedure is accounted for by the loss coefficient ($\zeta = 0.9$). The last observation made in Figure 79, is in the period between 2.5 to 2.9 hours where a sharp temperature increase is observed in the reported data. This is attributed to a potentially faulty reading in the thermocouple at this location. The proximity of warmer auxiliary flows could cause some additional heating of the thermocouple itself, independently of the exhaust steam behaviour itself. It is therefore likely the result of an on-site anomaly which would fall out of the scope of this turbine modelling methodology study. Despite this apparent anomaly, there is evidence that the model did predict a slight increase in temperature at the same time that the peak temperature was observed in the reported data.

The gross power output of the unit was also predicted over the course of the start-up simulation, with the results of this validation shown in Figure 80.

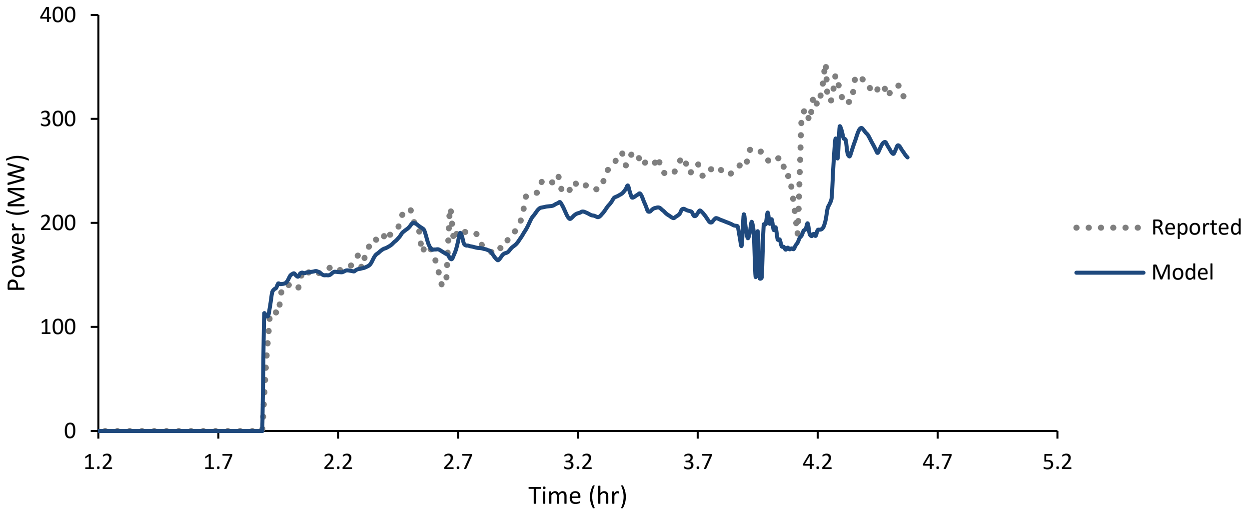

Figure 80: Modelled Unit Gross Power Output during Cold Start-up

The results of this validation are good in the context of the complexities which exist in simulating a full Cold Start-Up. One of the challenges which existed was determining when the feedwater heaters are brought into operation and whether they are brought online sequentially or collectively at a point in the start-up. This unknown saw the assumption of the feedwater heaters being brought online shortly after full rotor run up (approx. 3.5 hours into the start-up). The impact that this would have is that more steam would be extracted from the turbines in the model as compared to the actual start-up, thus reducing the predicted power output of the unit. Additionally, the constant loss coefficient assumption probably resulted in an excessive reduction of power output in phases of the start-up where ζ = 0.9 was really not appropriate. This is illustrated in accurate outlet temperature from the HPT unit between hours 1.8 and 2.8 which was also characterised by a power output also closely agreed with the reported value; suggesting an accurate lose coefficient.

In conclusion, the validation of the model in performing a full cold start-up was successful. The validation showed a relatively good agreement of the predicted values against the reported values from site. The shortcomings experienced during the validation could be attributed to added understanding of the turbine stage components itself and in the improved understanding of complex operational procedures not readily available to this academic study.

With the validation of the 1D Turbine model complete, the steam temperature evolution through both the HP and IP turbine units could be extracted from the model to be used as boundary conditions in the 3D FEA model. The temperatures for the HPT are shown in Figure 81.

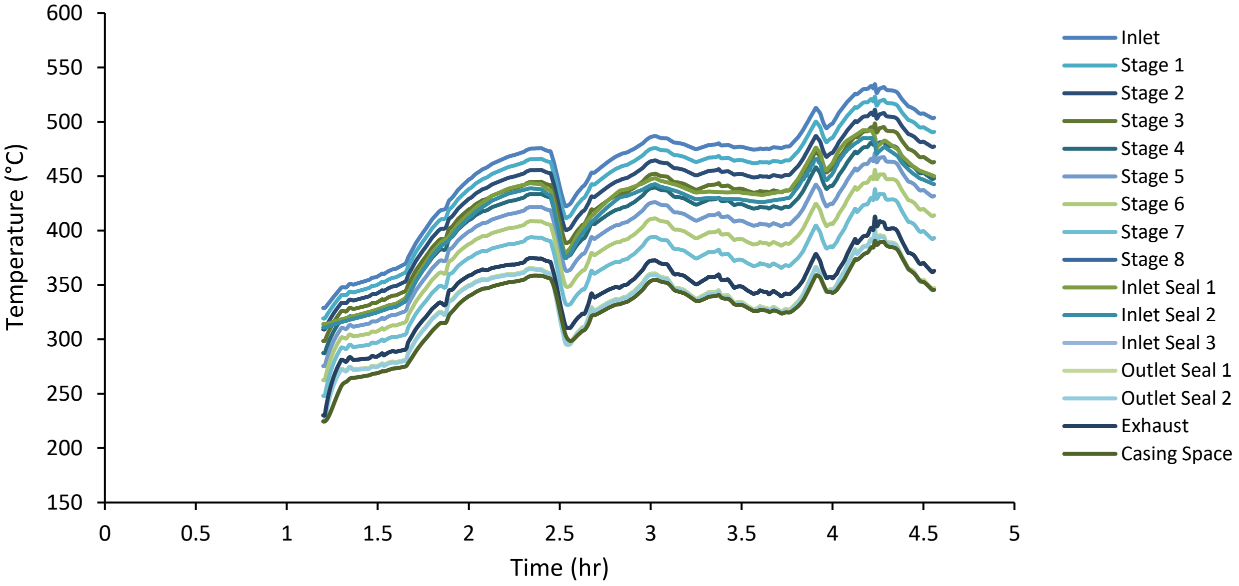

Figure 81: Modelled HPT Temperature Gradient during Cold Start-up

An overarching conclusion of this phase of the study is the necessity of a thorough understanding of the turbine process in the context of transient plant operation. Despite challenges experienced in gaining this understanding, this chapter demonstrates that given the minimal geometric input that was available, it was possible to generate a 1D Turbine Model to extract steam temperatures through both an HP and IP turbine within a reasonable level of accuracy.

5. 3D FEA Modelling

The development of the 3D Turbine Model was undertaken with minimal information from the Original Equipment Manufacturer (OEM). In past studies of this magnitude, such as in the work of Marinescu [15] and Topel [16] OEM support was central to the ability to generate the 2D models used in the respective study. The modelling of the 3D FEA model was performed using the following basic turbine documents:

- Sectioned Turbine Layout Diagrams (also used in the basic Nozzle Sizing procedure)
- Partially sectioned Isometric Diagrams (from the operator manual)

Using these diagrams is was possible to gain an overall picture of the turbine geometry of the HP and IP units, the modelling of which is documented in detail in this chapter.

5.1 Turbine Geometric Modelling

The modelling of both units was performed using Solidworks® CAD modelling software. The familiarity with the software allowed for the efficient creation of representative 3D solid models of both units. The ability to transfer the developed geometry to the ANSYS Mechanical environment was also another motivation for the use of Solidworks® during this phase of the study.

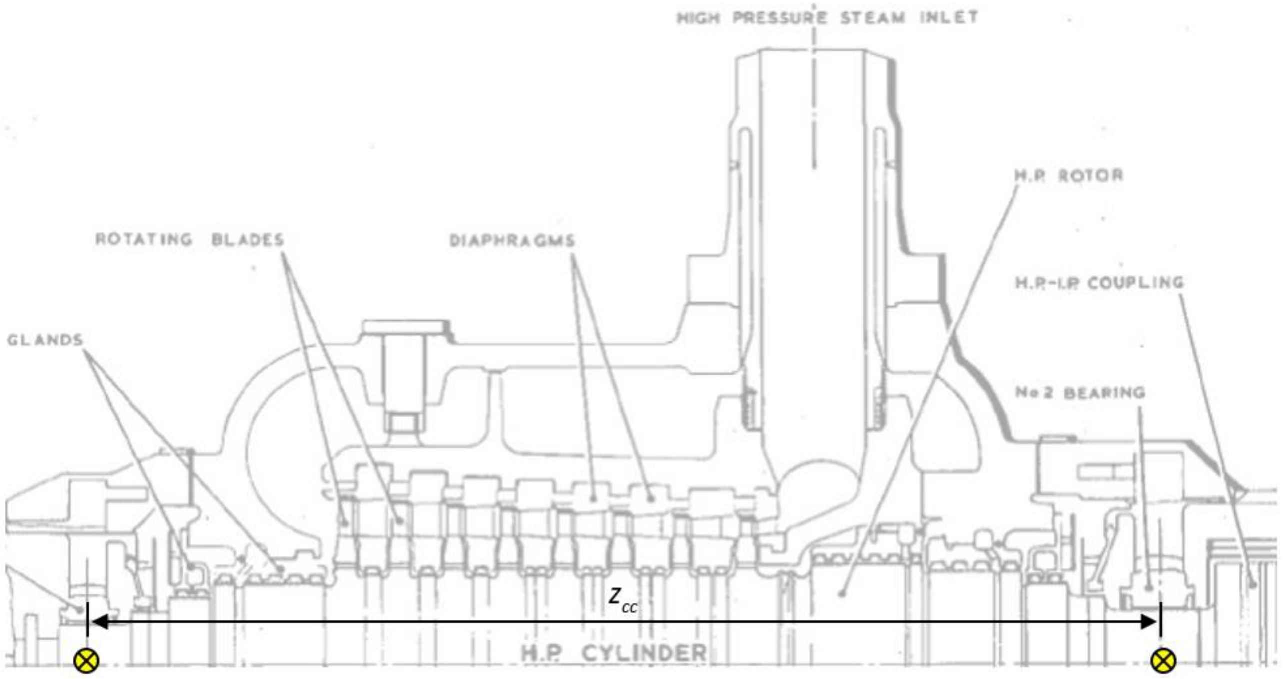

Figure 82: Sectioned and Isometric Sectioned diagrams showing candidate HP turbine.

The sectioned turbine diagram was the primary reference used during the initial modelling of the units, with the Centre-to-Centre distance between the supporting bearings (z_{cc}) as is shown in Figure 82, above. Using the Sketch feature, and by pasting the sectioned diagram onto the vertical plane, one was able to uses this initial axial measurement to scale the entire image by the appropriate measure, maintaining the image's aspect ratio. Each component was then traced and re-created using solid modelling features.

The turbine is made up of cylindrical (revolved) and planar features. The cylindrical features were predominantly modelled using the sectioned diagram, and included those features which are constrained along the axial direction such as the rotor, inner and outer casing cylinders, and gland seals. The planar features were inferred from the sectioned isometric diagram, representing the regions of substantial mass which would contribute to the thermal inertia of the unit. These planar features included the flanges and pedestal interfaces.

The modelling of cylindrical features was created using the Revolved Boss feature in a relatively short time due to the components' symmetry around the centre axis. The revolved modelling of the HPT rotor is shown in Figure 83.

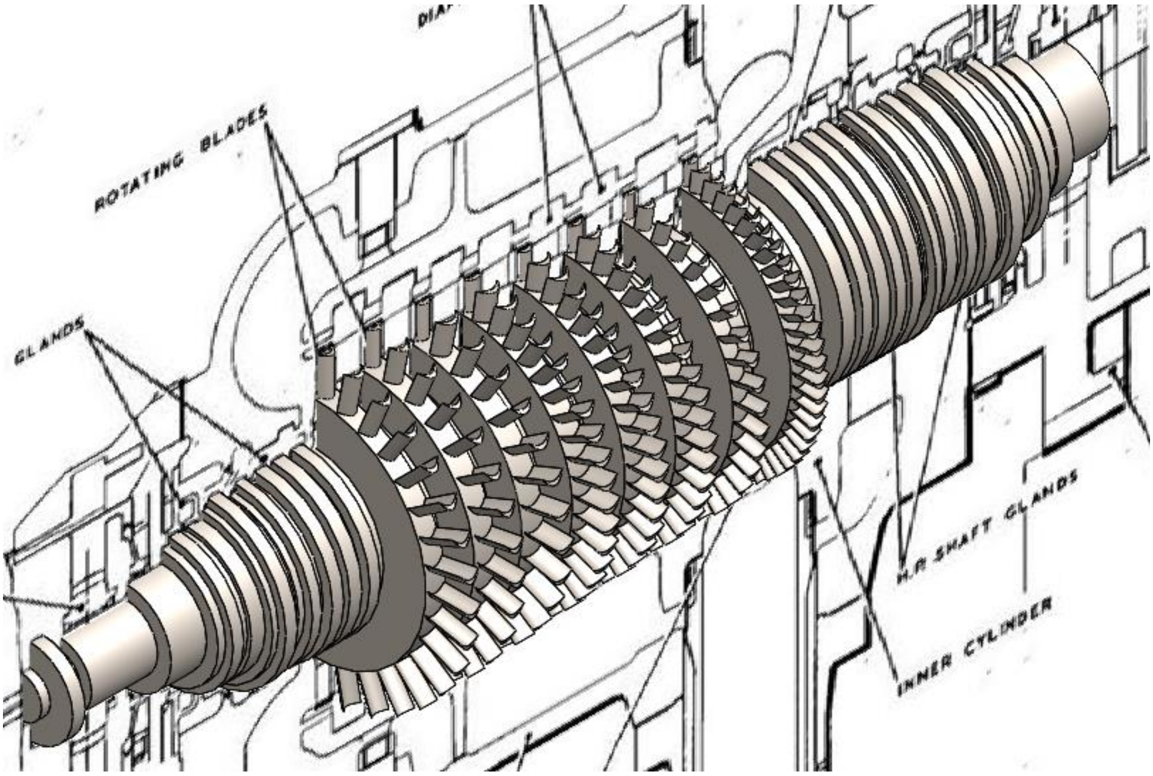

Figure 83: Revolved Boss of HPT rotor from sectioned view

Figure 83 also shows a very detailed approach in the initial stages of modelling. In particular was the development of representative individual blades based on typical blade geometries as well as detailed seal geometry. From the detailed approach, some simplifications were made, driven primarily by the reduction of computational complexity in the FEA phase of the study as well as to reduce the time spent modelling both HP and IP units.

The perspective drawings also aided in creating the other non-symmetric geometries, such as the inlet pipe connection and leak-off pipe.

5.1.1 Rotor and stator simplifications

A concern around the intricate shape of the rotor and stator blading was the significant increase in the mesh density required to capture the blade and stage nozzle geometry. The FEA model is only concerned with the radial thermal expansion, not the detail blade expansion. Given that the Flownex SE model captured the flow dynamics of the steam flowing through these channels, the rotor and stator blades were simplified as disks perpendicularly orientated to the steam flow. Figure 84 demonstrates the simplification of the rotor and stator for the HPT main cylinder configuration.

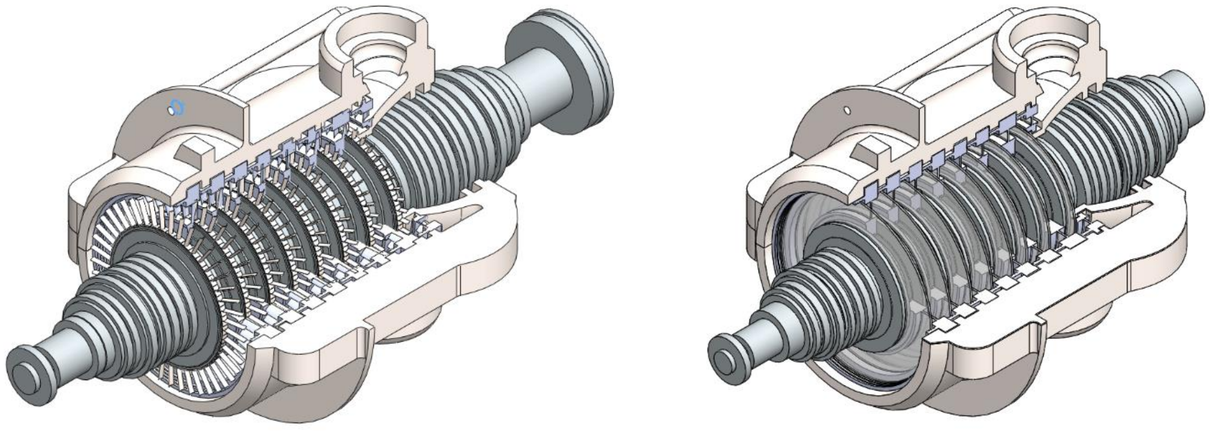

Figure 84: Simplified Turbine Model

The resulting rotor "blades" were of the same outer diameters as the actual unit, however the blades differed in thickness to create an equivalent thermal mass despite the simplified geometry. This is different to what was done by Topel [16], where the blades were removed entirely to achieve the geometric simplification. Given that the motivating factor of this study was to predict the internal clearances within operational turbine units, particular focus needed to be placed on the rotor tip clearance. In order to extract this value, a representative rotor with correct outer diameter had to be modelled.

Further rotor simplification can be seen in Figure 85, below, where the complex rotor-blade interface was replaced by a continuous revolved geometry with equivalent blade thickness.

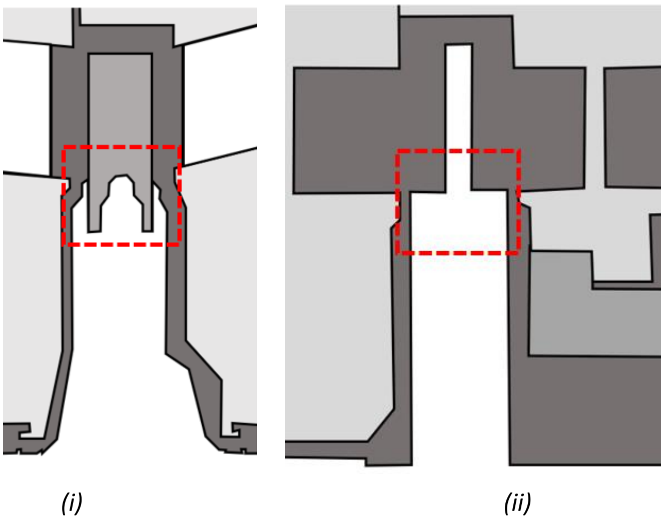
(i) *(ii)*

Figure 85: (i) Detailed rotor and (ii) continuous rotor geometries

The continuous modelling approach of the rotor and stator components led to quicker and simplified modelling of the overall turbine units, allowing for a complex system such as a turbine to be modelled with relative ease.

5.1.2 Gland Seal Simplification

The gland seal surfaces found at extreme ends of the HP and IP presented significant modelling complexity in the FEA application. A volumetric approach was taken in making this simplification. It was assumed that the seal surfaces extending from the rotor were so thermally insignificant in comparison to the gland seal and rotor that they could be included as an equivalent bulk volume on the gland seal itself, giving the simplified seal in Figure 86.

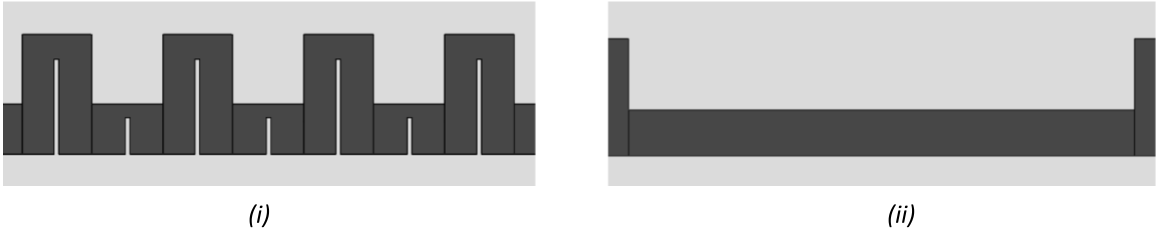
(i) *(ii)*

Figure 86: (i) Detailed and (ii) simplified gland seal configurations.

Furthermore, given that the configuration of the gland seals is determined by the fluid mechanics of slowing leak flow and producing a pressure drop without a loss of energy, as opposed to thermodynamic cooling, as in a heat exchanger, it was assumed that this simplification would not negatively impact the accuracy of the 3D turbine model.

Considering the seal stages in Figure 86 alone, the simplification sees a reduction in surfaces from 40 to 2, greatly reducing the computational expense in capturing the clearance behaviour of these regions. Given the size of these seals, in Figure 43, the surface area loss is minimal within the context of larger rotor and casing components.

5.1.3 Flange heating geometry

Due to the significant thermal mass of the flanges, additional heating, beyond that delivered by the main steam within the outer cylinder, is required to the outer casing flanges. Figure 87, shows the typical flange heating flow path observed when the flange heating system is in operation.

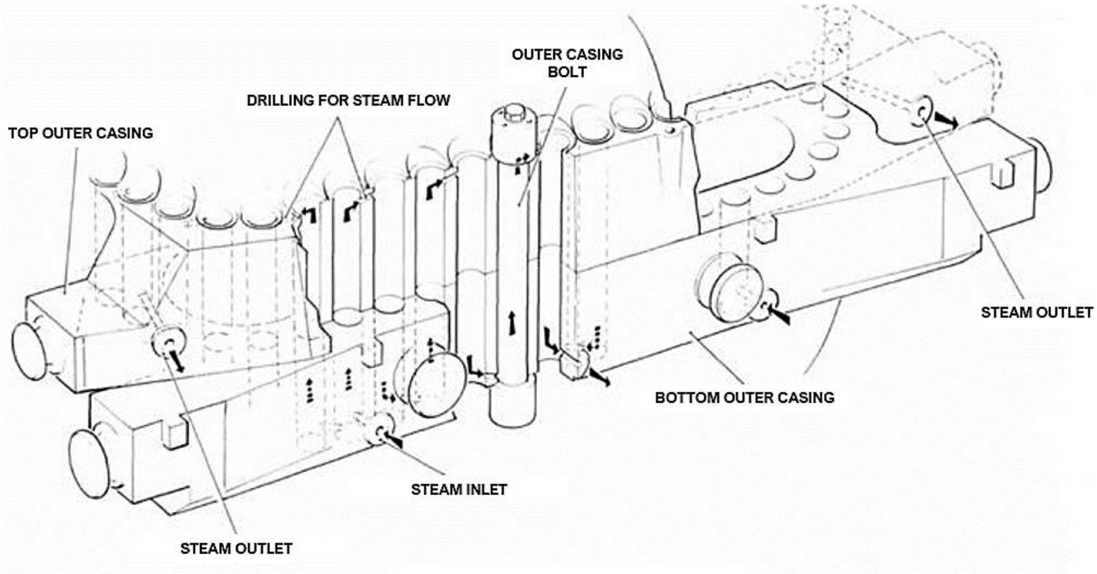

Figure 87: Typical Flange Heating Configuration [25]

The operating principle of this system is the movement of steam, taken from the inlet throttle valve of the unit, through passages that exist in the clearance between the flange and the Outer Casing bolts. This flow heats both the flange and the casing bolts, allowing for a more controlled expansion of the outer flange regions. A simplification was made to the inner and outer flange with the exclusion of the bolts which fasten the two casing halves together. Given, that the bolts would fill the respective holes, the thermal expansion behaviour of a simplified solid without the bolt was found to be sufficient in this study. The decision to model the bolts and cavities as continuous solids was taken to reduce the complexity of the turbine model whilst ensuring the integrity of the turbine casing's Thermostructural response.

Given the simplification to this region when considering the flange heating loads, which would ordinarily be centred around the locating bolts, a representative surface was formulated on which to apply the flange heat load. This was achieved through an equivalent groove layout which was developed, as seen in Figure 88. A groove of equal arc length to the actual bolt arrangement was created, ensuring heat was transferred to the same regions of the flange creating a representative loading distribution.

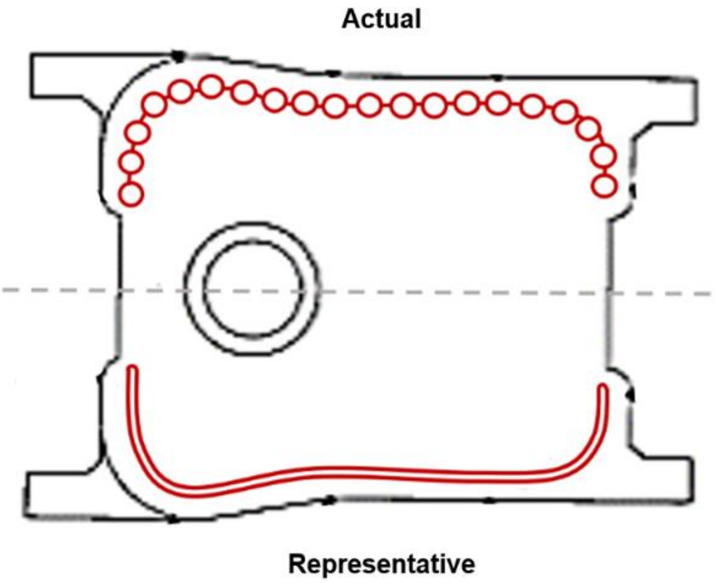

Figure 88: Comparison of actual flange heating vs representative flange heating paths, adopted from [22]

A negative impact of the groove in the outer casing is that it physically splits the flange into an inner and outer region. This will cause discontinuous heat transfer and may result in undesirable deformation and twisting of the flange during the start-up simulation. For this reason, a constraint was added to ensure that the clearance within the groove would remain constant, allowing for the uniform heat transfer through the space as well as the application of a temperature boundary.

This constraint was achieved through the use of a forced connection in the FEM turbine model. A forced connection allows for the mating of two faces which are not coincidental, such as in the case of the inner surfaces of the flange heating groove. This constraint fixes the separation of the two faces to remain constant throughout the simulation whilst still maintaining the ability to apply a temperature boundary to the faces in the connection. This force connection is shown in Figure 89.

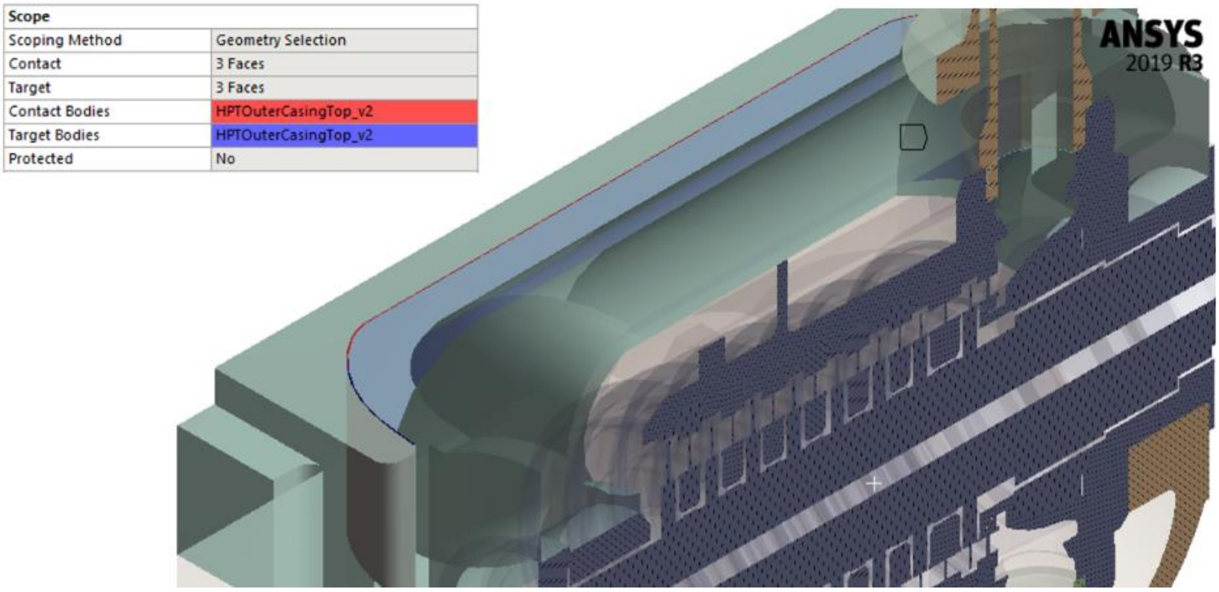

Scope	
Scoping Method	Geometry Selection
Contact	3 Faces
Target	3 Faces
Contact Bodies	HPTOuterCasingTop_v2
Target Bodies	HPTOuterCasingTop_v2
Protected	No

Figure 89: Forced connection application to Flange Heating Groove

5.1.4 Final geometry

The final 3D models of both the HP and IP turbine is shown in Figure 90 as well as in detail in Appendix C.

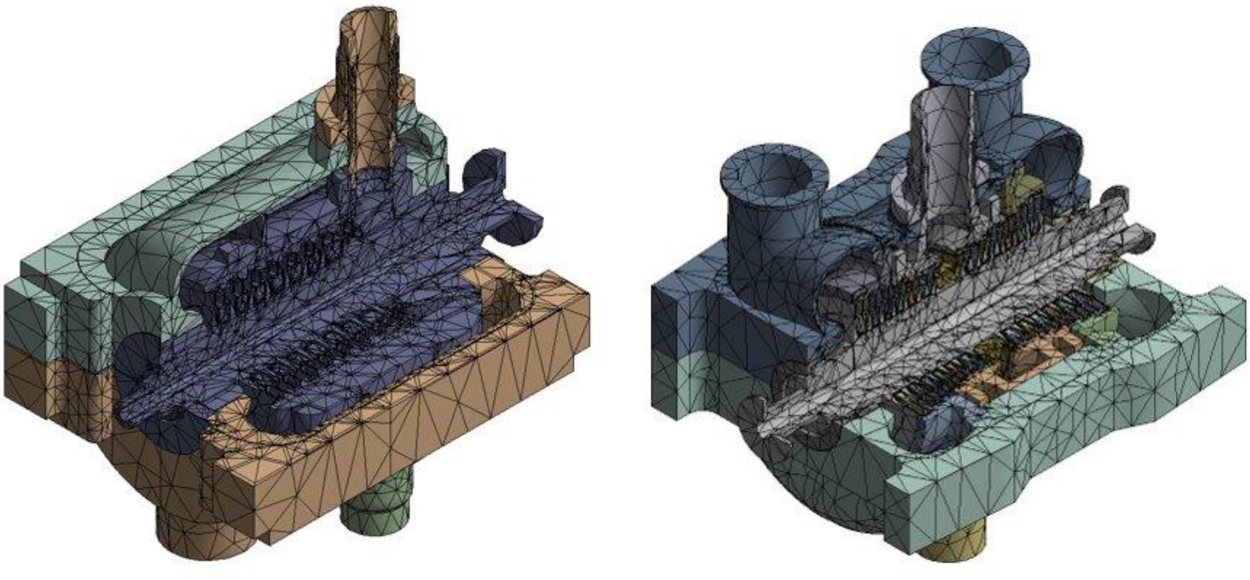

(i) (ii)

Figure 90: (i) HPT and (ii) IPT FEA models

Although some excessive detail was modelled in development of the HP turbine, the lessons learnt were applied directly to the IP turbine modelling. This satisfies the overarching goal to produce a method that can easily be applied to various other turbines without the need of detail OEM data.

5.2 ANSYS Integration

After the development of the 3D models for both the HP and IP Turbine units of the candidate unit, it was necessary to import the Solidworks® files using the ANSYS Mechanical workbench into respective FEM model files.

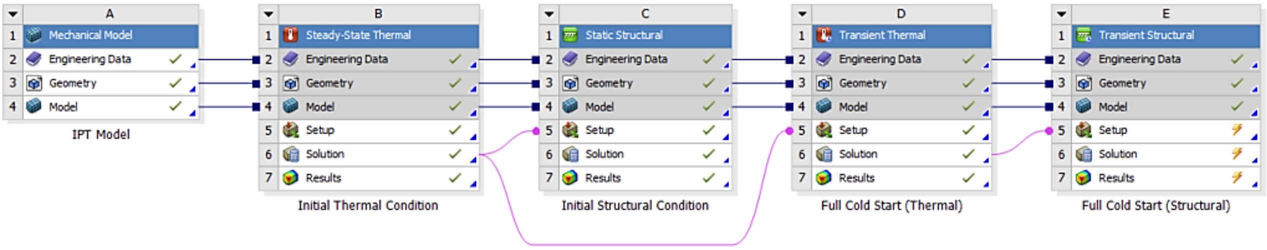

Figure 91: ANSYS Workbench Configuration for IPT model

The above workbench configuration was established for both the HP and IP Turbine FEA models, in a linear sequence of simulations. The initial conditions of the unit were established from steady state thermal and structural simulations. These initial conditions are discussed in more detail in later chapters, with these states being correlated to thermocouple data from site.

The linear sequence of the simulations ensures that the initial condition of the transient simulations is taken from the steady state simulations as the model state is updated from the upstream simulation. The linear sequence results in the structural condition of the model to be updated after each simulation before the start of the next simulation, which was the desirable updating scheme.

The transient simulations differ only in that it allows for the variable application of temperature boundaries as a function of time, from the initial conditions established in the steady state simulations. The establishment of these initial conditions are dealt with in more detail in later chapters.

5.3 Material Assignment

Moving into the FEM environment, it was necessary to accurately capture the material properties of the various components in both units. Reference to OEM documentation provided necessary detail of the different materials used in respective components. The outer and inner casings of the respective units is made of cast Molybdenum Vanadium steel [22][23]. Commonly referred to as Chrome-Molybdenum High Tensile Steel (AISI 4140), this steel has the ability to maintain its mechanical properties at high temperatures up to and beyond 538°C [24]. The rotor of both units is composed of a rotor shaft made of the same Molybdenum Vanadium steel, in this case being forged as opposed to cast [22]. “Non-rusting steel” is described as the material used for both the diaphragms and rotor blades. Given the high temperature application of the rotor and stator blades Stainless Steel 316 was chosen for the diaphragms in the FEM model. Given the continuous geometric simplification made to the rotor, the rotor was prescribed as being made of Molybdenum Vanadium steel (AISI 4140), as with the rest of the rotor shaft.

Table 14: Mechanical and Thermal properties for rotor and casing materials used in HP and IP Turbine FEM Models

Property	**Low Alloy Steel, 4140**	**Stainless Steel 316**
Mechanical Properties		
Elastic Modulus (GPa)	205	193
Poisson’s Ratio	0.29	0.265
Tensile Strength (MPa)	655	580
Yield Strength (MPa)	415	290
Thermal Properties		
Thermal Expansion Coefficient (µm/m.K)	12.3	16.5
Thermal Conductivity (W/m.K)	42.6	18.9
Specific Heat (J/kg-K)	473	500

Table 14, shows the mechanical and thermal properties of Molybdenum Vanadium steel (AISI 4140) assigned in the turbine rotor, and the inner and outer casings.

5.4 Structural Constraints

The thermal expansion experienced by the modelled turbine components is not only a function of the material selection detailed in the previous section but also the structural constraints prescribed to the model. After consulting with on-site engineers, the predominant axial expansion of the rotor and casing components were explored, with the expected axial expansion detailed in Figure 92, below:

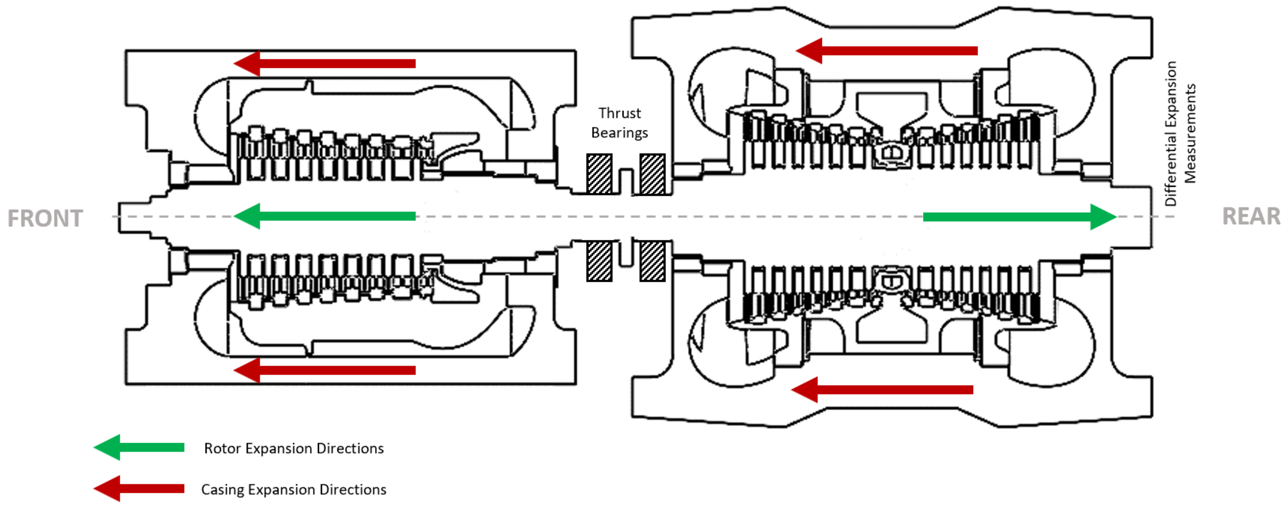

Figure 92: Nominal Expansion Directions expected for HP and IP turbines

A thrust bearing is housed within the turbine pedestal which joins the outer casings of both the HP and IP turbines. The pedestal is allowed to move axially through sliding supports which also allows for the thrust bearing to translate by the same distance as the IP outer casing. Simply put, the distance between the thrust bearing and both outer casings remains constant during operation. The rear end of the IP casing is fixed to ground, thus causing all the casings to expand towards the front. The outer bearings, on the front end of the HP and back end of the IP, are simple radial bearings which are housed within independent pedestals. It is on these pedestals that the differential expansion readings are monitored.

Given that the HP and IP FEM models are independent from each-other, as well as to reduce the computational complexities to structurally couple both models, adaptations had to be made to the constraints applied to the model itself, which will be explained next.

5.4.1 High Pressure Turbine Constraints

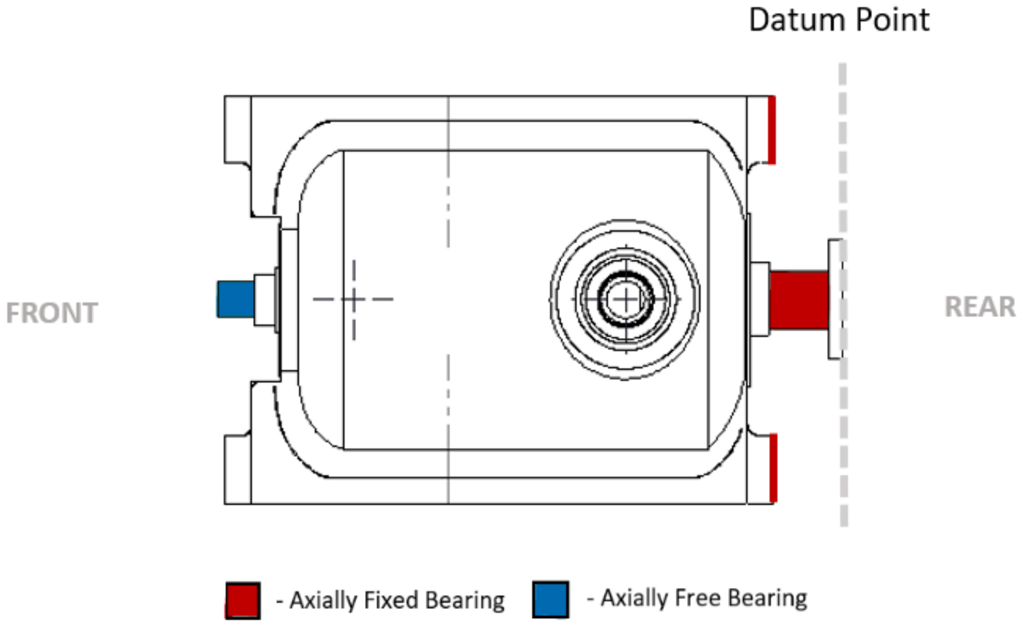

Figure 93: HPT Structural Constraints

Figure 93, shows the structural constraints applied to the HP turbine. The constraint methodology saw the creation of a datum point at the thrust bearing joining both units. This means the rear end of the rotor as well as the rear surface of the outer casing was axially fixed. The front and rear cylindrical support also maintained the radial location of the rotor ensuring that the rotor is able to rotate along a constant line of rotation. The front cylindrical support, representing the front bearing, is allowed to axially move relative to the casing, allowing for a representative differential expansion reading to be measured from the model. For both the HPT and IPT models a constant gravitational force ($g = 9.81\ \mathrm{m.s^{-2}}$) was applied in the downward direction.

A steady state verification using a uniform temperature change, shown in Figure 94, was carried out on the above constraints to ensure the predominant deformation of the unit was as expected.

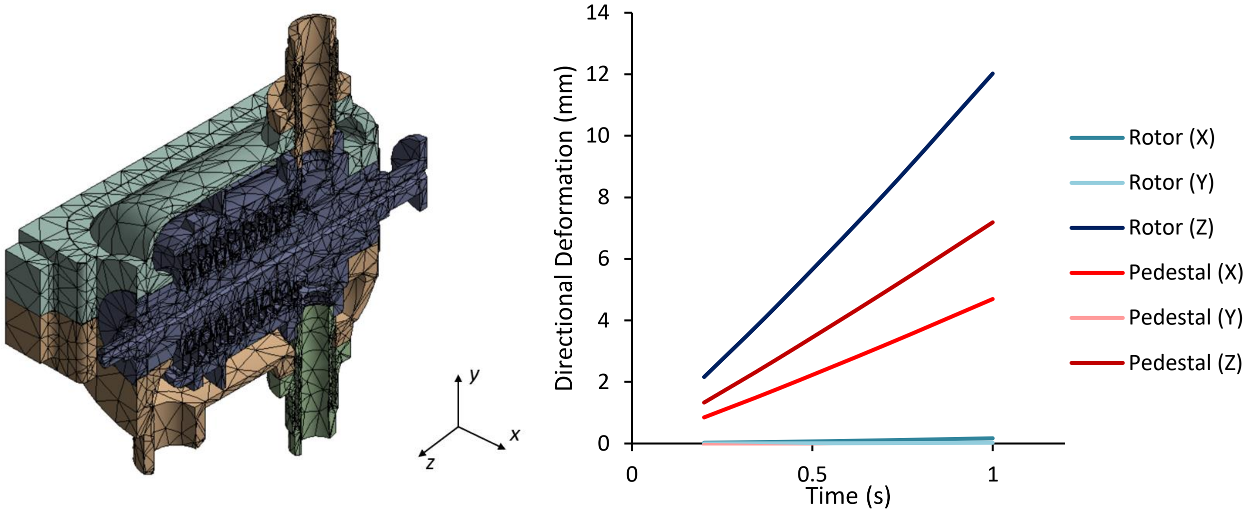

Figure 94: Structural Constraint Verification showing front displacement for a uniform temperature increase

The verification showed that the greatest movement of the model at the front surfaces was in the axial direction (positive Z) with deformation also evident in the transverse (positive X) direction. This transverse expansion was expected and allowable as the unit is expected to expand outwards from the centreline, an action which will be characterised by a transverse expansion of the pedestal interface.

The remaining deformations, which are nominally zero shows that the model is axially constrained, through the minimal deformation of the rotor is the X-direction. The lack of expansion of the rotor and pedestal in the Y-direction further confirms the axial constraint of the rotor and casing at the pedestal interface and that there will be a purely axial expansion of the turbine components between the two bearing locations. The verification, in Figure 94, confirmed the satisfactory application of structural constraints against the expected behaviour of the unit in operation.

5.4.2 Intermediate Pressure Turbine Constraints

The expected expansion of the IPT in Figure 95 shows the role that the thrust bearing between the HP and IP Turbine unit in managing the relative expansion within the IPT.

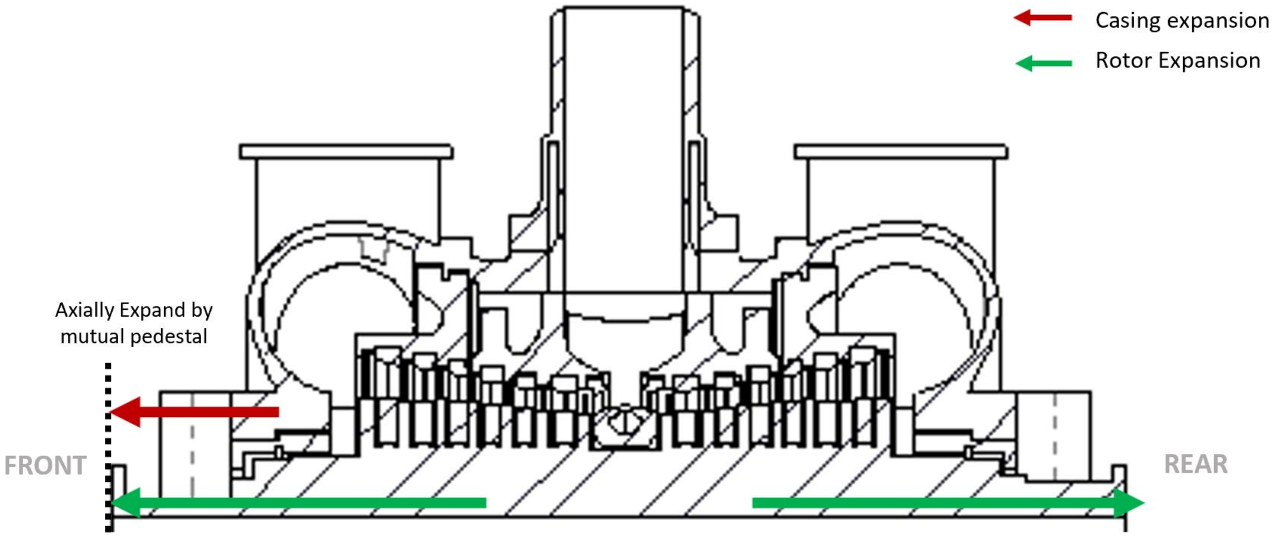

Figure 95: Nominal Expansion directions for IPT

Unlike the HPT the expected expansion of the rotor is towards both the front and rear, starting from the centre. The IPT casing is physically constrained at the rear, with the casing expected to expand axially towards the front. However, since the thrust bearing pedestal is linked to the movement of the IPT front casing, there is no relative expansion between the rotor and casing at the front. The net effect is only a visible expansion at the rear. This is where the differential expansion reading is taken on site. From a structural point, the axial constraint of both the rotor and casing can be applied to the front, similar to what was applied to the rear of the HPT.

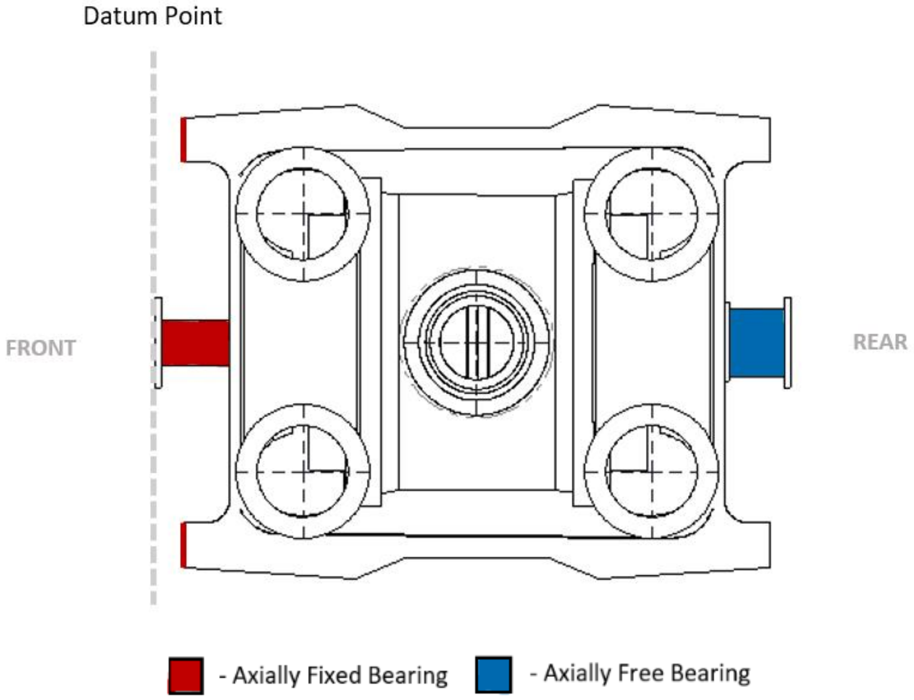

Figure 96: Constraints applied to IPT model

This method imagines one measuring the differential expansion using the thrust bearing as a reference plane, such that the IPT now expands purely towards the rear. The need for such a simplification is motivated by the complex relative expansions of both the casing and rotors as well as the desire to capture the structural constraints of the model in a computationally inexpensive manner.

5.5 Convective vs Surface Temperature Boundaries

An important link between the Flownex SE turbine model and the ANSYS turbine model is the application of the node temperature results, computed in a one-dimensional sense, to a representative 3D volume. The 1D turbine model produces temperatures between each stage. Since the stages are predominantly impulse type, the total temperature remains the same from the stator inlet to the rotor inlet. The work is only extracted after the rotor, hence a change in temperature is observed. Figure 97 shows how the temperature results were applied to the various cavities along the main steam path.

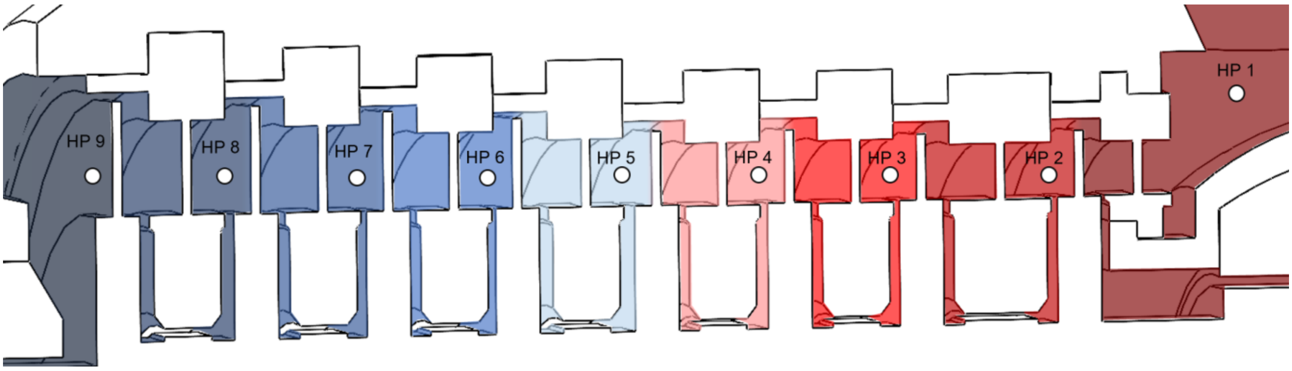

Figure 97: Application of node temperatures to representative volumes

A key observation made during this phase of the study is the appropriate boundary condition to apply to these volumes. ANSYS Mechanical allows one to apply a surface temperature boundary to selected surfaces, such as the surfaces illustrated in Figure 97, which would be prescribed solely as a scalar temperature value. Alternatively, one can specify a convective boundary condition, matching more closely the realistic interaction of steam with turbine components. The fixed temperature boundary would be equivalent to a very high convection coefficient. Recall from Equation 2.15 that the inclusion of a convection coefficient requires a volumetric integration by the solver. One could expect that such a boundary condition will require more computation as compared to a simple fixed surface temperature.

A comparative study of the difference in each of these boundary condition approaches was undertaken. Anecdotally, due to the high mass flow rates observed through the main steam path, one would expect the surface temperature to be very close to the steam temperature in that region. As in the modelling of the low-mass flow regions of the Flownex turbine model, the Dittus-Boelter correlation was used for the turbine stages and gland seal regions as shown in Figure 98.

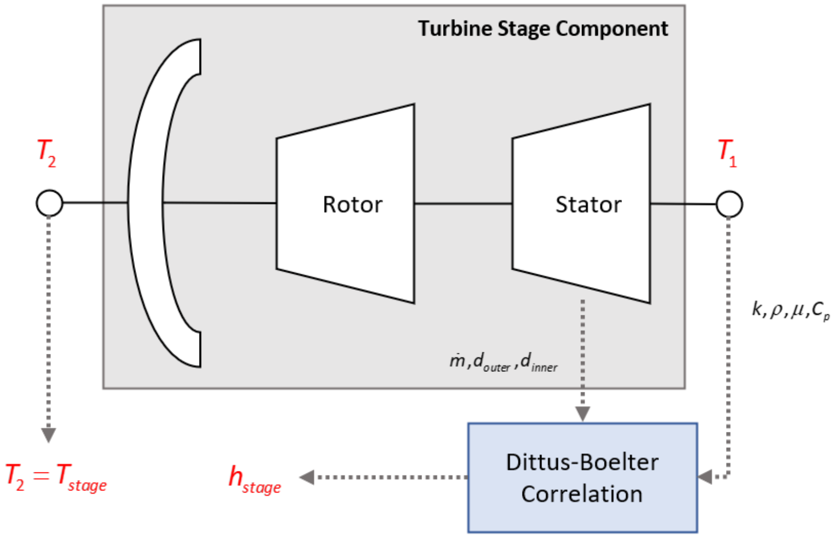

Figure 98: Turbine stage application of Dittus-Boelter Correlation

Applying the above solving method to each turbine stage as well as each stage of the inlet and outlet gland seals yielded the results seen in Figure 99. A limit of 1000 W/m^{2}K is indicated on the graph to indicate the regions where a convection boundary condition would be important.

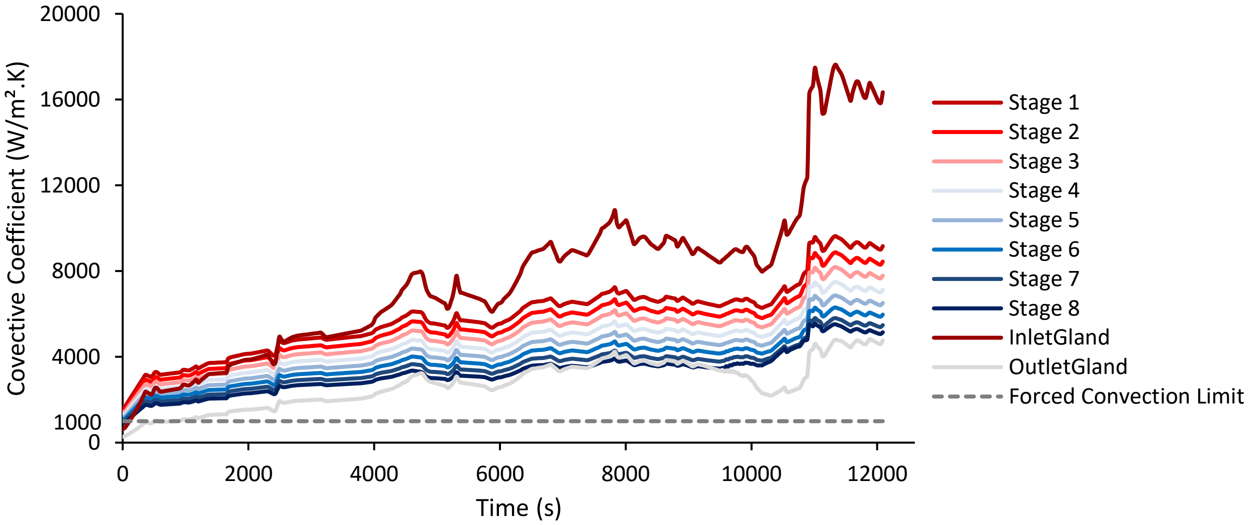

Figure 99: Convective Coefficients for HP turbine and gland stages during start-up

Figure 99, demonstrates that for the majority of the cold start-up procedure these regions experience very high convection conditions. With convective coefficients this high, a surface temperature assumption can be made on the surfaces interacting with the steam flow through the turbine cylinder. This assumption was further tested through a steady state temperature analysis of the HP turbine using a 60% load case temperature gradient. The result of this analysis is shown in Figure 100 and Figure 101.

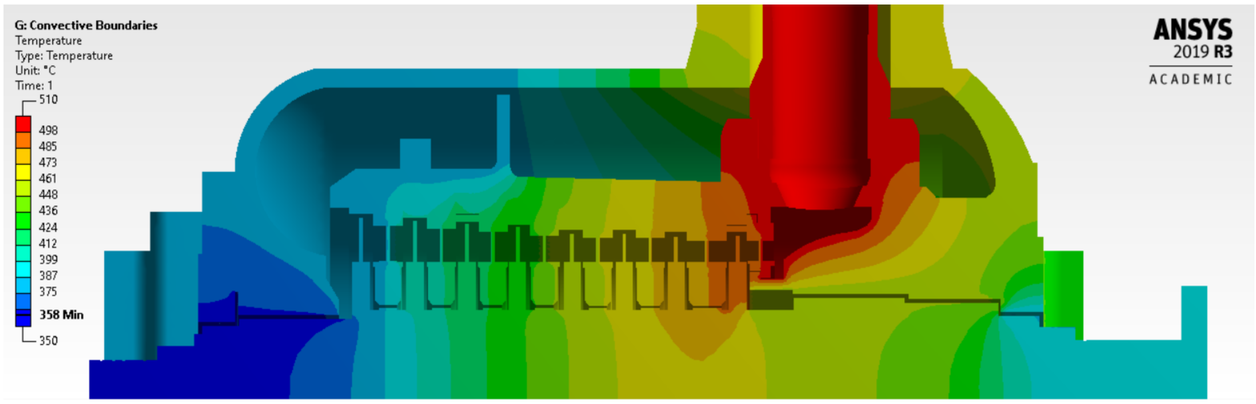

Figure 100: Temperature Gradient from Convective boundary conditions

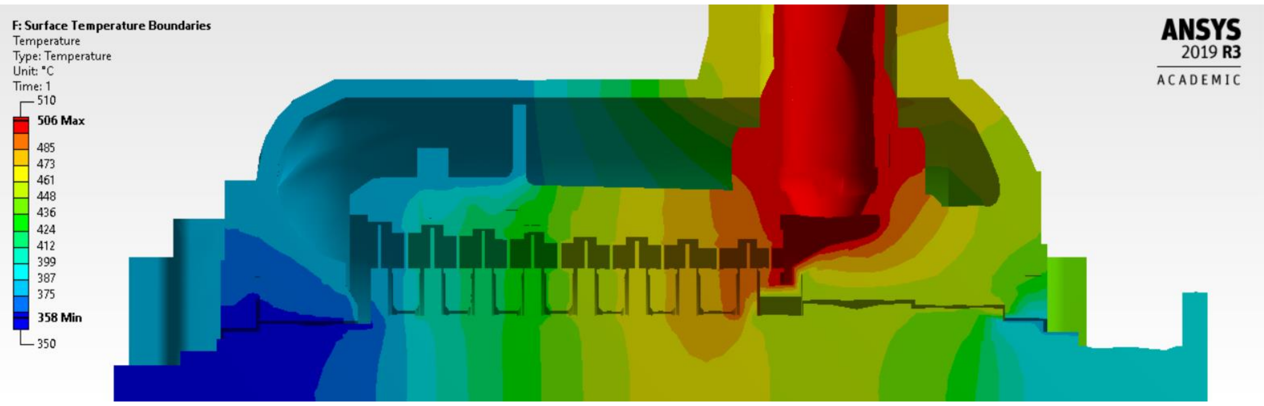

Figure 101: Temperature Gradient from Surface Temperature boundary conditions

For the convective boundary simulation some occurrence of high temperature nodes exceeding the boundary temperatures of the region was observed. This was attributed to insufficient convergence of these nodes due to poor mesh size. Given this, further refinement of the global mesh size was conducted to increase the number of nodes in the convective model relative to the surface temperature model. After this refinement, convergence was found in the convective model for approximately 655 000 nodes, with significantly increased solving time, whereas the surface temperature remained stable with a low node density with approximately 80 000 nodes. The solving time between the two cases was substantially less for the surface temperature case. This was expected in considering Equations 2.13 and 2.14, which shows increased FEA solving requirements for the convective boundary condition case against the surface temperature boundary. The solving time was order of magnitude larger for the convective case, such that without the increase in computational capacity a surface temperature boundary conditions was opted for.

Additionally, the smaller number of nodes required to produce a stable result, as well as the reduced simulation time, makes the surface temperature approach the desirable method in applying the temperature boundaries gathered from the Flownex Turbine Model. An additional benefit is that making such a boundary assumption negates the need to develop a stage-by-stage Dittus Boelter solution scheme and allows simpler application of the temperature boundaries.

The above findings gave a useful indication as to the sensitivity of the model when prescribing convective boundaries. The modelling method which was ultimately used was a hybrid boundary approach using both convective and surface temperature boundary conditions. The approach saw the high flow regions, such as the turbine stages and gland seals, being described by surface temperature boundaries and low flow regions, such as the casing space in the HPT and the rotor cooling flow of the IPT, being described by convective boundaries. The comparative study was useful in this regard as it gave an indication as to the mesh density required for the convective boundaries to achieve computational convergence.

For convective boundaries, the Face Sizing Mesh function, within ANSYS was used. On these faces, the surface mesh was refined to a smaller mesh element size whereas the remaining volume was modelled using a global mesh element size larger than that of the convective boundary. This method was selected as it minimised the number of nodes needed to model the full HP and IP units, whilst ensuring accuracy in the final results.

5.6 Flange Heating Calibration

The flange heating system can be activated any time during the course of the start-up. The source of steam used in the flange heating systems of both units is from the governing valves found at the units' inlet. Figure 102 demonstrates the flow of steam extracted from the governing valves into the flange heating grooves and out to the condensate tanks at the system's outlet.

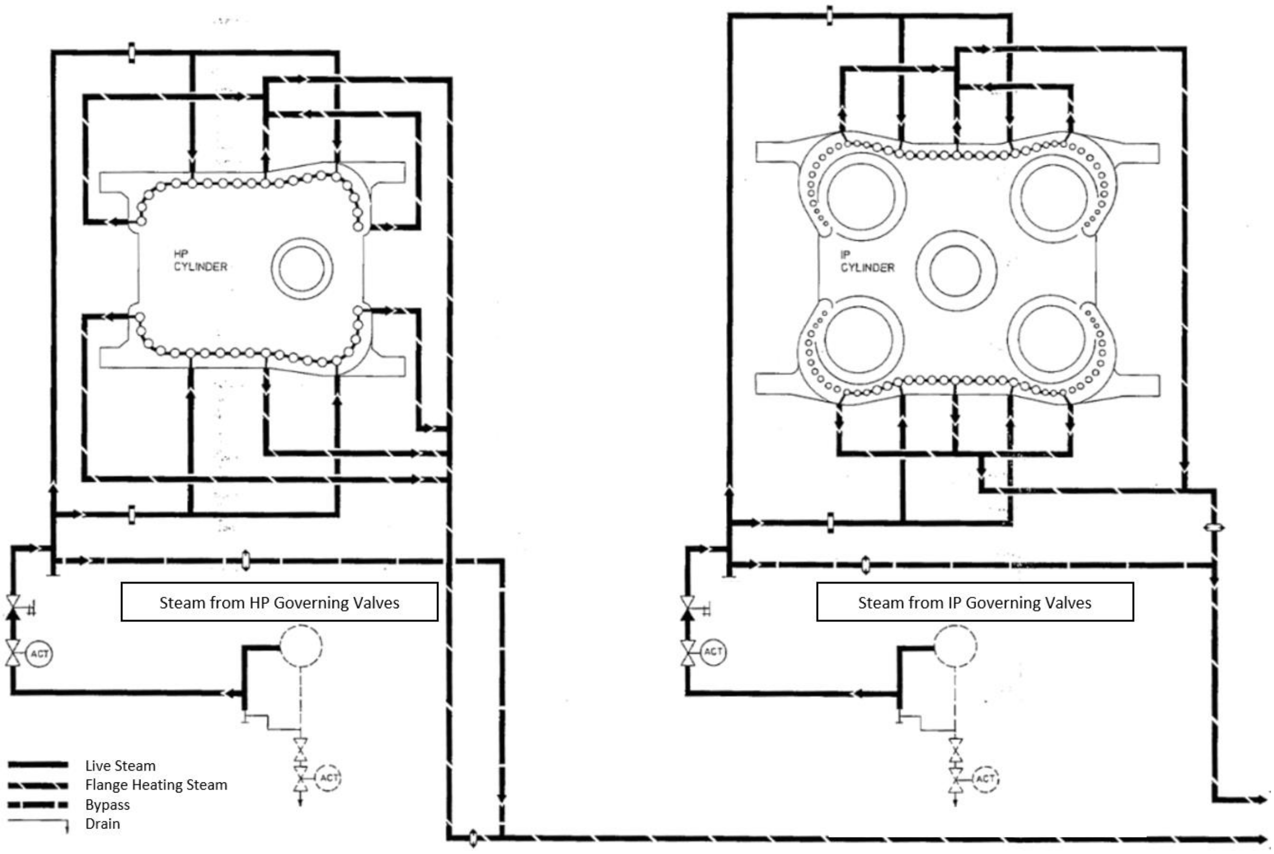

Figure 102: Flange heating system flow and instrumentation diagram

Since the flange heating system is operator-controlled, there is not a prescribed or known condition during start-up. In order to “switch” the heating ON or OFF during the transient, a convective boundary condition was added to the flange heating groove. A low convective coefficient < 0.1 W/m^2.K was used when the flange heating system is in the OFF condition, and a convective coefficient > 100 W/m^2.K was used for the nominally ON condition.

The period of heating as well as the magnitude of the convective coefficient was estimated by looking at sudden changes in the differential expansion data. A sudden drop in the differential expansion would indicate the activation of flange heating, after which the convection coefficient was manually adjusted to achieve agreement between the reported and measured data. This is evident in the figure below.

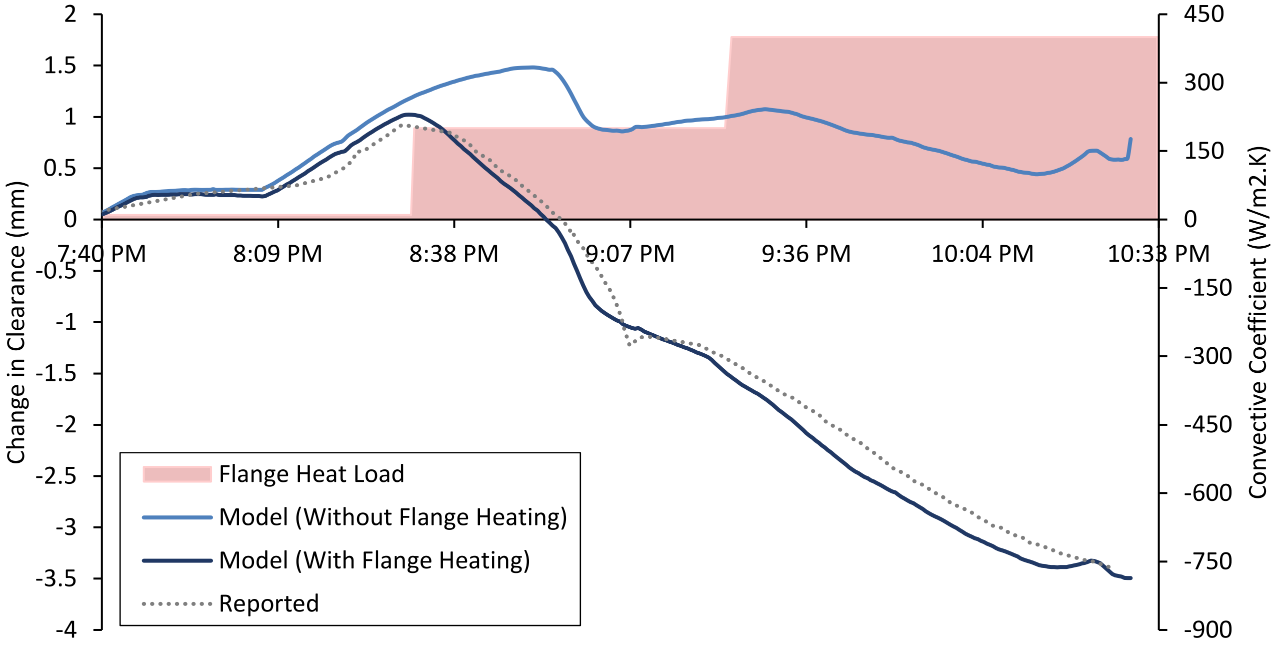

Figure 103: HPT differential expansion with and without flange heating

The same method was employed for the IPT, but since there were more than one peak in the profile, some further refinements were also made.

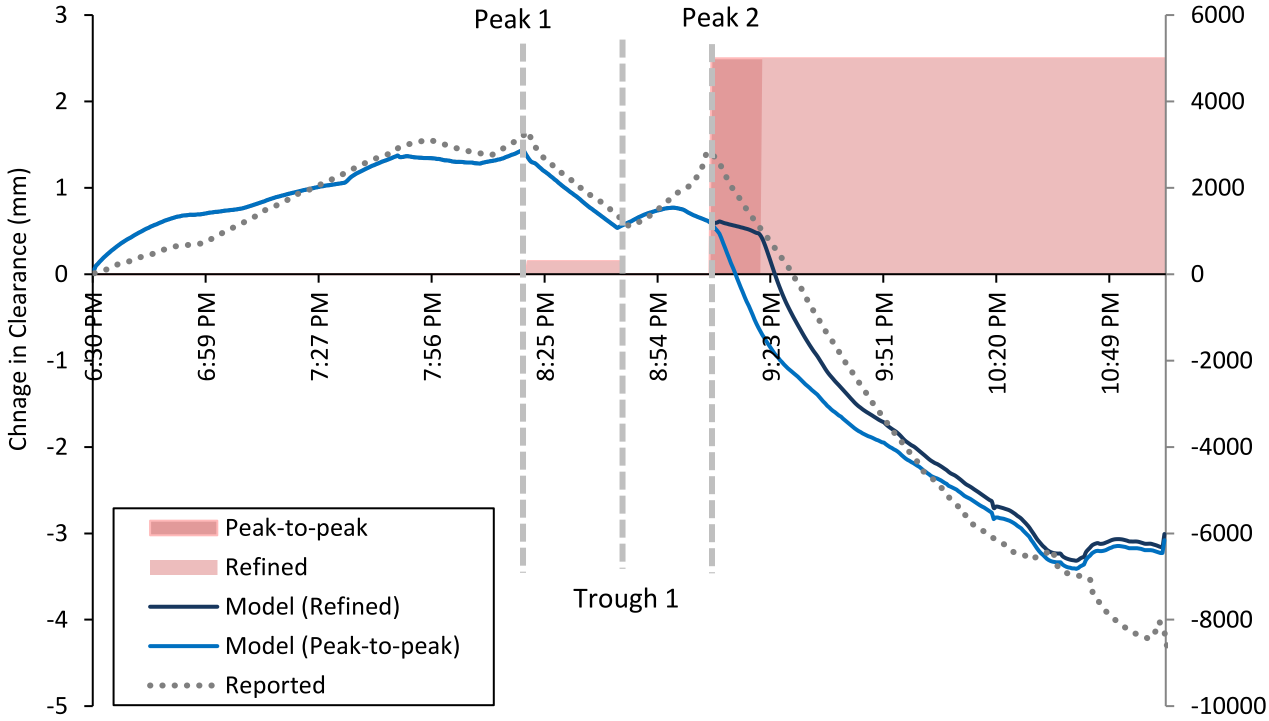

Figure 104: Peak-Trough method to calibrate Flange Heating input in IPT

The second differential expansion peak visible in Figure 104, is still not fully captured. This inability is attributed to two factors: Firstly, as much as the flange heating is a dominant boundary condition affecting differential expansion, the expansion is also a function of the inner temperature boundaries, defined by the 1D Turbine Model. It is possible that at this instance in the start-up, the inner boundary conditions are such that the pedestal and rotor see similar responses for given temperature changes. This is indicated by the “levelling off” of the predicted value during this period of the expected peak. Secondly, it is possible that an inaccurate value of the flange volume of the simplified turbine has led to a slight deviation in the differential response of the pedestal relative to the rotor. At those temperatures and the significant heating which had already occurred to that point, the peak in the reported data suggests a “lag” in the pedestal expansion compared to the rotor. This “lag” would be as a result of the thermal inertia, directly proportional to the mass of the component. The inability for the model to predict this peak points to insufficient thermal mass in the pedestal. Further iterations of this study should ensure that the thermal mass in the flange of the models is accurately captured.

The addition of flange heating in the model is evidently vital to predicting the relative axial expansion of the turbine casings and rotor. In the case of this study, a more thorough understanding, or even actual measured data of the flange heating, would have helped to reduce the amount of calibration needed. This calibration does somewhat detract from the elegance of the method as one can calibrate the thermal expansion results to closely match the measured data. This was deliberately avoided by applying very course flange heating boundaries to the model.

5.7 Mesh Independence Study

An important aspect to manage in FEA is that of mesh density, simply the number of nodes captured within the FEM geometry. In the field of FEA, mesh independence is achieved at a mesh density which produces an accurate, yet efficient result. It is general practice, as in industry, to conduct a mesh independence study.

In simple thermal models, like those seen in a two-dimensional sense, a steady state thermal or structural load is applied to boundary nodes. One tracks the convergence of internal nodes against increasingly dense meshes, seeking convergence of the steady state response. However, in a three-dimensional modelling methodology, as in this study, further considerations needed to be made to the mesh size selection. This study found limitations in the largest mesh size available, due to the need to adequately capture the solid geometry on the 3D turbine model. Additionally, due to the interest in studying transient thermal expansion, a methodology for tracking the convergence of the rate of thermal expansion was developed.

In this study a second order tetrahedral solid mesh type was used, producing nodes through the solid turbine geometry. In order to establish this mesh type through a solid body, ANSYS Mechanical establishes a mesh on a geometry through a process called Sweep Meshing [26]. This is a process by which ANSYS “sweeps” the volumes in the prescribed geometry and attempts to generate a mesh with regular sizing as prescribed by the user [26]. Due to the complexity of the turbine models created for this study, there is a natural limitation to the mesh element sizes that can be used. This limitation is imposed by ANSYS attempting to minimise the number of nodes needed to capture the geometry sufficiently. Through a trial-and-error approach it was found, in the HP turbine, that an element mesh size of approximately 550mm was the upper limit of the allowable Mesh Element Size before the model failed to successfully generate a mesh.

Given that the focus of the study was on the transient modelling of clearance within the HP and IP turbines during start-up, a transient mesh independence study was undertaken. This involved decreasing the mesh element size by 50mm for each simulation and recording the axial expansion of the turbine rotor and pedestal over a 20-minute period after a step temperature change. The axial expansion of the HPT rotor was recorded, seen in Figure 105, for the sequentially smaller mesh element sizes demonstrating a clear convergence of the transient response of the rotor.

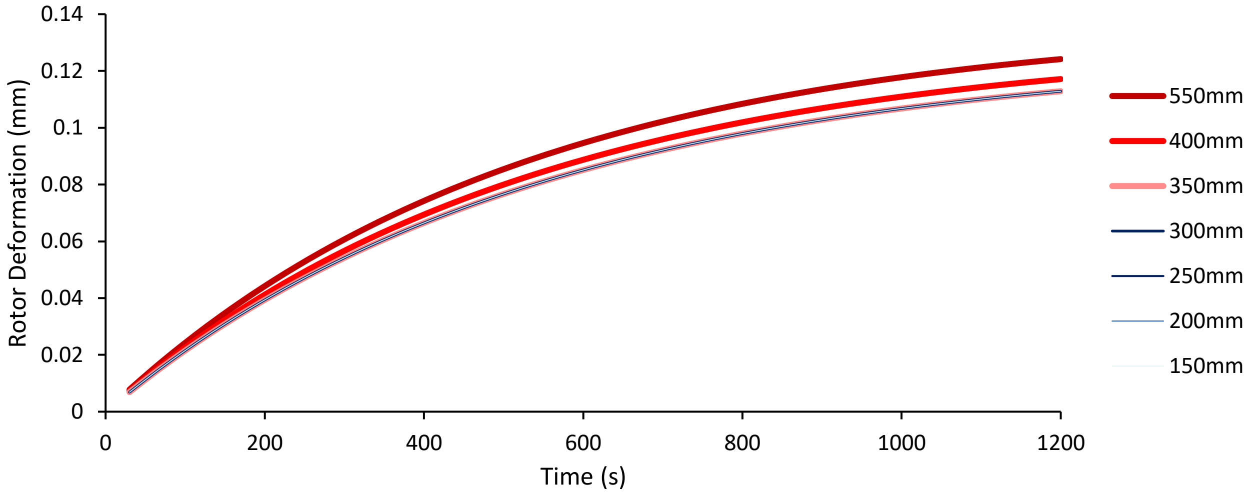

Figure 105: HPT Rotor Offset Axial Expansion given step temperature change

The shape of the deformation in the figure above represents a typical exponential function in the form:

$$z = z_0 + A\left(1 - e^{-t/\tau}\right) \tag{5.1}$$

where

τ - time constant
A - steady state deformation
z_0 - inital expansion @ t_0

Given the focus of the mesh independence study to track the transient response of the rotor as opposed to the total response, mesh independence is best measured w.r.t the time constant. The time constant was the indication that the model had converged to a transient structural response. This is shown below in Figure 106. The solving time for each simulation was also recorded to ensure a choice was made considering both accuracy and time.

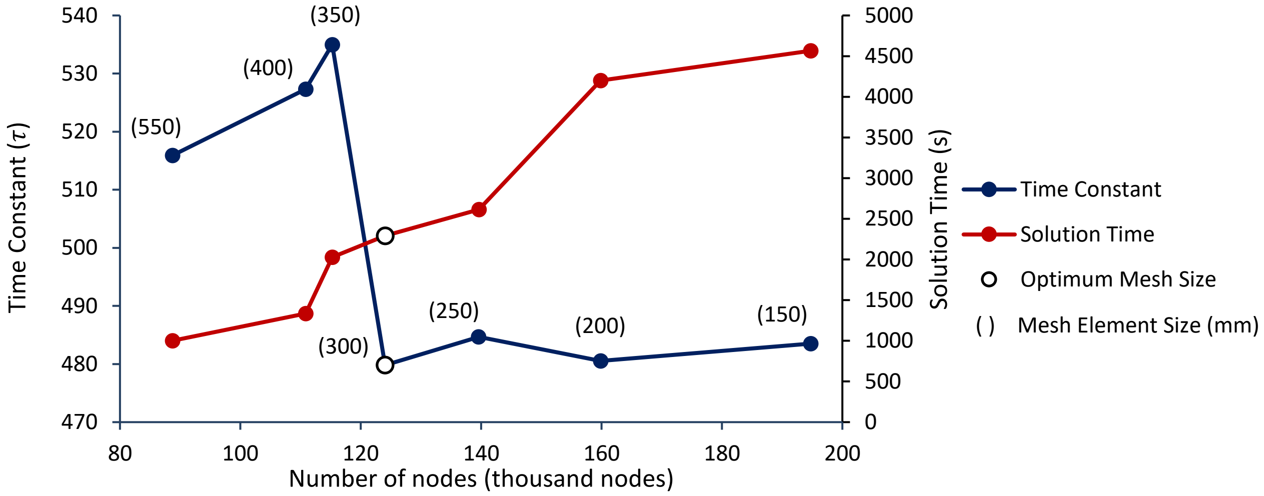

Figure 106: Mesh Independence Study Results for the HPT rotor

It is evident from the mesh convergence that a mesh element size of 300mm (139 611 nodes) is sufficient in producing an accurate and efficient result in the start-up simulation. The same method was used for the IPT.

5.8 FEA Model Validation

5.8.1 Thermal validation data selection

In order to validate the thermal response of the FEM model, on-site thermocouples were used to compare the predicted metal temperatures with the actual measured temperatures during start-up. There is a large collection of thermocouples installed on both the HP and IP turbine units, representing a significant data capturing and validation exercise if one were to attempt to validate the turbine model to all of the thermocouples available. For this reason, it was decided to select only a few representative thermocouples for the HP and IP units respectively. These are shown in the figures below.

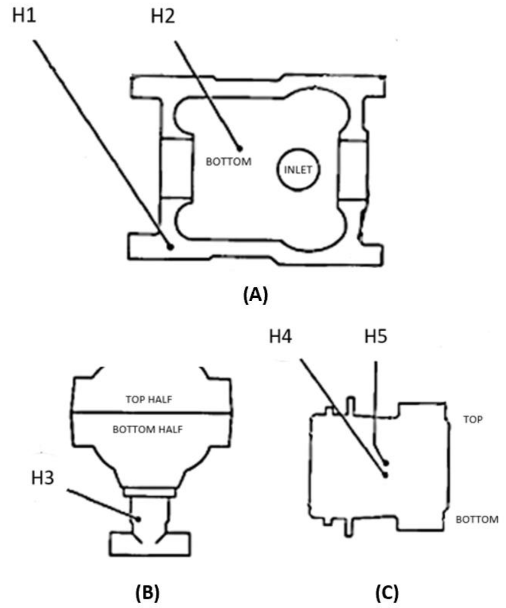

Name	Description
	Outer Casing
H1	LH flange exhaust end mid wall
H2	Barrel bottom midspan mid wall
	Loop Pipe
H3	Bottom tee piece inner wall
	Inner Casing
H4	Inlet plane inner wall
H5	Inlet plane outer wall

Figure 107: (a) Section top view, (b) Outer front view (c) Inner casing top view of selected validating thermocouple locations on HPT

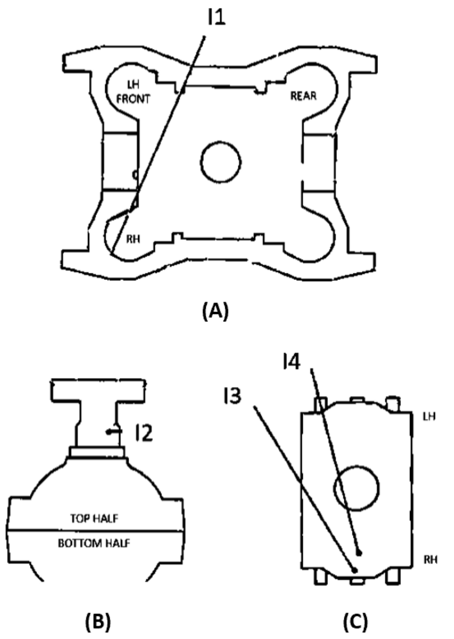

Name	Description
	Outer Casing
I1	RH flange exhaust end mid wall
	Loop Pipe
I2	Top tee piece inner wall
	Inner Casing
I3	Inlet plane inner wall
I4	Inlet plane outer wall

Figure 108: (a) Section top view, (b) Outer front view (c) Inner casing top view of selected validating thermocouple locations on IPT

Each of these thermocouples was selected for a specific purpose in validating the modelling approach in this study. Thermocouple H1, situated on the left-hand front flange, was important in capturing the differential expansion of the flange relative to the rotor. In addition, the thermocouple proved important in calibrating a likely flange heating profile during cold start-up. Thermocouple H2, situated on bottom half of the outer cylinder, is important in validating both the Flownex and ANSYS turbine models. The thermocouple allowed for the validation of the barrier plate steam flow in the 1D Flownex Turbine Model shown previously in Figure 51, validating the use of the Dittus-Boelter Correlation. Secondly, this thermocouple validated the approach taken in the ANSYS turbine model in assuming a surface temperature boundary prescribed to the area at the exhaust end of the barrier plate and a convective boundary to the low flow casing space region beyond the barrier plate as seen in Figure 109.

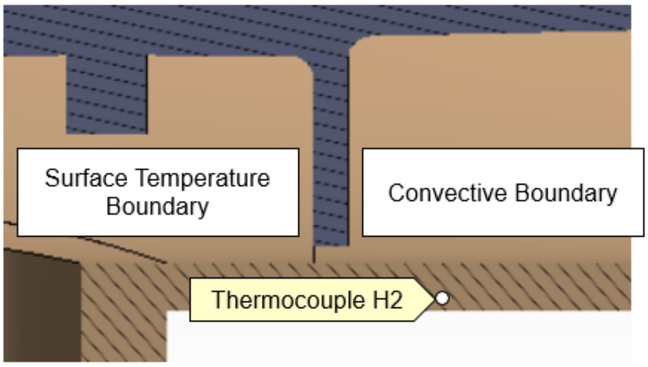

Figure 109: Thermocouple H2 location relative to temperature boundaries in ANSYS turbine model

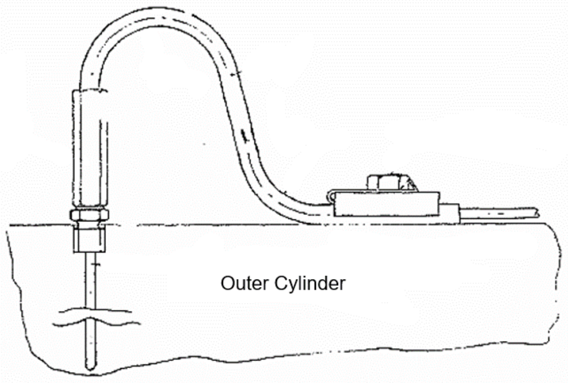

Figure 110: Middle Metal Thermocouple configuration on outer cylinder

The validation of the predicted temperature of the model at Thermocouple H3, was less important than the remaining thermocouples but did allow for a final check on the primary boundary condition of Flownex and ANSYS model in that the Flownex boundary conditions were generated in an hour-by-hour sense of the cold start whereas the thermocouple data was captured relative to the exact time of day, this reading allowed for the alignment of the rest of the thermocouple readings relative to the model results from this calibration.

The validation of Thermocouple H4 & H5 was most significant, along with that of Thermocouple H1 to the overall success of modelling approach in this study. The configuration of this thermocouple is shown in Figure 111 and Figure 112 below.

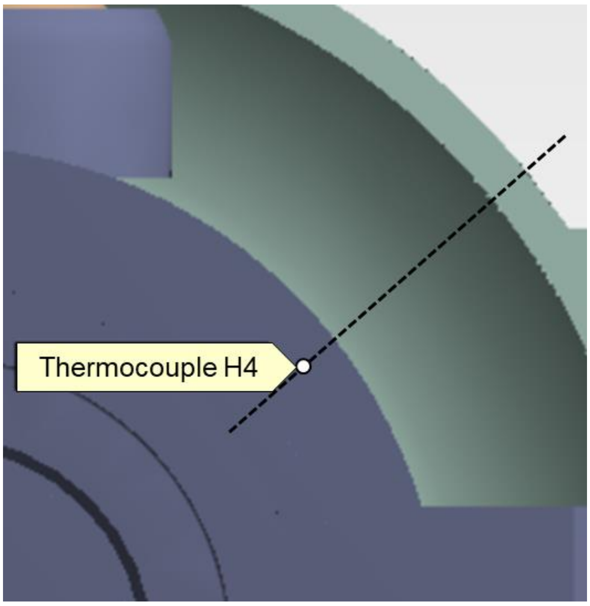

Figure 111: Thermocouple H4 location relative to temperature boundaries in ANSYS turbine model

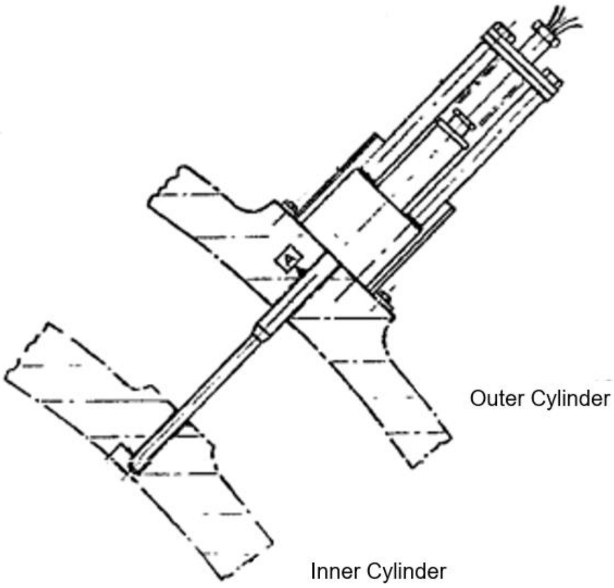

Figure 112: Inner & Outer Metal Thermocouple configuration on outer cylinder

This thermocouple is significant as its validation is a function of the temperature boundary prescribed by the results of the Flownex turbine model. The axial location of this thermocouple can be seen in Figure 107 such that the thermocouple reading is a function of fourth stage temperature boundary in the Flownex model. The validation of this thermocouple validates the turbine stage component within the model as well as validating the 1-dimensional Nozzle analogy approach in modelling turbine start-ups.

The thermocouples used in the IPT were a function of whether the sensor was capturing reliable information for the given start-up. Unfortunately, of the four sensors collected, only two were operable. Notwithstanding, a degree of validation was still possible. Thermocouples I3 and I4 are of the same configuration as Thermocouples H4 and H5, capturing both the outer and inner metal temperature at the inlet plane of the unit. In a similar way to the HPT, these thermocouples served to validate the stage-by-stage boundary conditions prescribed by the 1D Turbine model.

Given the scarcity of the validating thermocouples for the IPT, the loop pipe thermocouple, Thermocouple I1, was used to validate the inlet boundary conditions and validate the surface temperature boundary approach adopted in both the HPT and IPT. The exact configuration of the loop pipe thermocouple itself was difficult to deduce from the available documentation, but relative to the sensor diagram, a representative location for the thermocouple was selected, as shown in Figure 113.

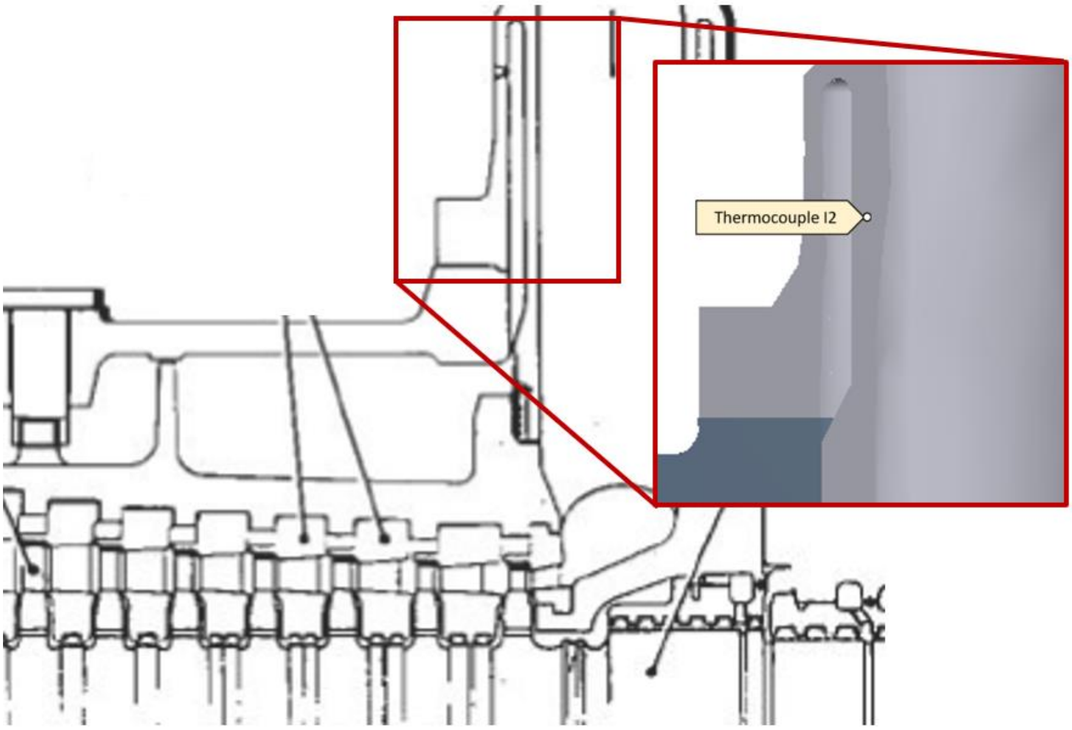

Figure 113: Thermocouple I2 location relative to temperature boundaries in ANSYS turbine model

It is evident from the selection of these thermocouples that, despite the primary focus of these thermocouples being to validate the 3D FEA model, the validation of the thermocouples plays a vital role in the validation of the turbine modelling methodology as a whole, including the 1D Turbine Model. Additionally, it shows the importance of on-site thermocouple data in validating modelling approaches taken in this study, such as boundary condition selection and volume representation in the 1D Turbine model.

5.8.2 Turbine Initial Thermal Condition

From the boundary conditions sourced from plant data, the initial condition of the unit at the point at which steam first enters the HP and IP cylinders is important to match the material response of each turbine component. The development of this initial condition was based on the general operational procedure on site with the admission of steam through the gland seals prior to main steam admission, as well as thermocouple data from the initial time step of the developed cold start thermal boundary layers.

This was modelled as a Steady State thermal simulation in ANSYS. The thermal boundaries used in this model assumed that steam entered and exited the cylinder though the gland seals, with no steam leaving through the inlet and exhaust pipes of the respective units. A further outer boundary condition was prescribed on the flanges of both models to simulate the much cooler flanges at the beginning of the start-up procedure. This condition was calibrated by looking at the flange thermocouple measurements.

Table 15: Comparison of Reported and Modelled Thermocouple results from Initial Condition Modelling

Thermocouple	Reported Value	Modelled Value	Absolute Error (%)
H1	130.66	130.73	0.05
H2	234.38	228.58	1.89
H4	289.45	288.1	0.47

Table 15, above demonstrates that the approach adopted allows for a replication of the probable turbine condition at the first initial time step of the cold start procedure. Further confirmation of the approach was sought in the differential expansion at the initial time step. The result was a predicted differential expansion of 5.07 mm compared to a reported value of 4.74 mm accounting for a 7.0% error between reported and modelled values. Given the sensitivity of this reading to initial conditions of the unit as it is on site, it was decided that the initial conditions met the criteria for being a sufficient representation of initial start-up conditions and that an offset reading from this initial condition would be used during the latter differential expansion validation. This meant that all expansions of both the rotor and pedestal would be measured relative to the initial conditions detailed above. The initial temperature profile of the HPT unit is shown below in Figure 114, demonstrating the significant flow in the inner cylinder of the unit but with significantly cooled condition in the flange region.

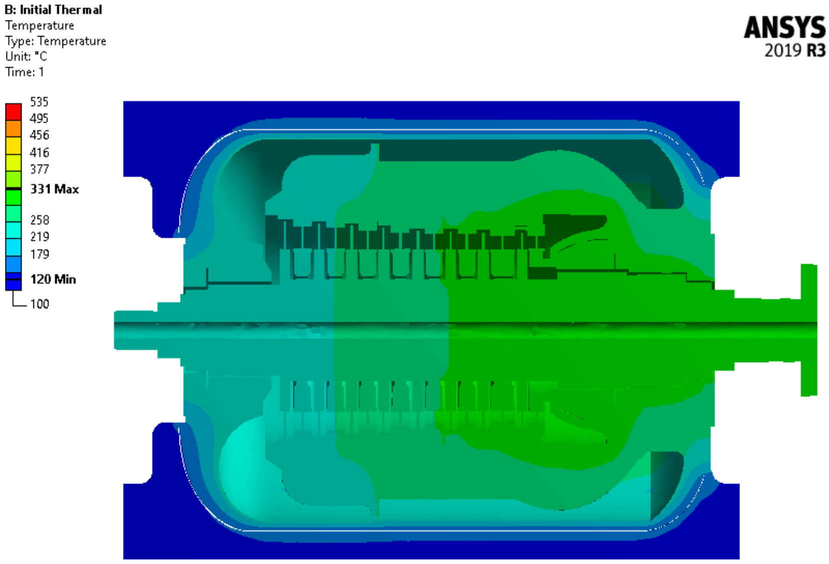

Figure 114: Initial Temperature Profile of HPT prior to Cold Start

The initial condition formulated above, was also validated against the reported differential expansion reading at the first time-step of the start-up simulation. Table 16, shows the differential expansion value predicted by the model from the initial turbine condition.

Table 16: Initial Differential Expansion at Initial Condition

Sensor	Reported Value	Modelled Value	Absolute Error (%)
HPT Diff. Expansion	5.07	4.73	7.18

This result shows a 7.18% error between the reported and predicted value, which is a good correlation, given the assumptions made about the exact condition that the unit is in at the beginning of the start-up. The accuracy of this number speaks to the validity of the method used to establish the initial condition of the HP turbine model.

The initial condition of the IPT was more difficult to formulate than the HPT. For the HPT, at the point at which steam is first introduced into the unit, substantial heating has likely taken place, which validates the internal heating seen in the initial condition. This results in a case in which the metal temperatures are likely close to that of the main steam at first admission. For the IPT, a uniform metal temperature was assumed through the entire model, seen in Figure 115

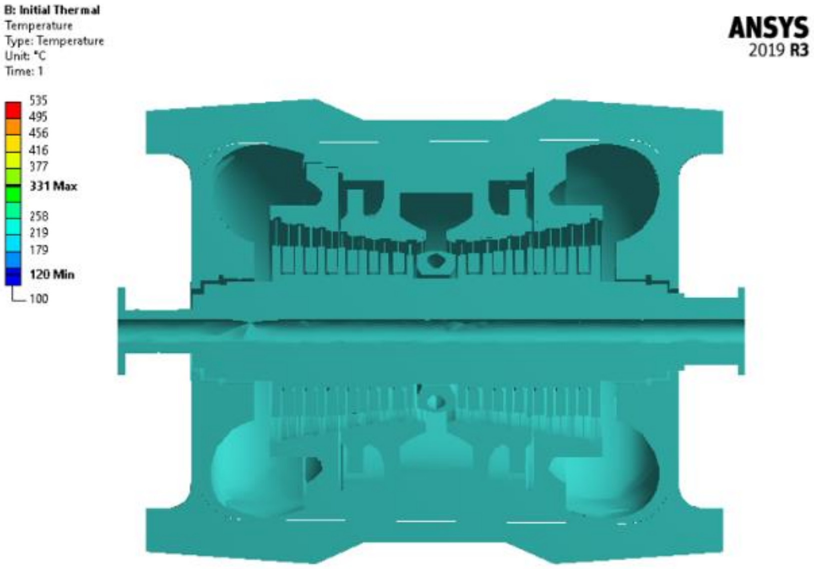

Figure 115: Initial Temperature Profile of IPT prior to Cold Start

This temperature was assumed from the thermocouple data collected from the candidate unit, which led to the assumption of the initial metal temperature being in the order of 230°C.

5.8.3 Thermal validation results

From the flange thermocouple (Thermocouple H1), the likely time of flange heating taking place could be estimated, and the calibrated convective coefficient could be applied to the flange heating grooves as described in previous chapters. Figure 116 shows the temperature progression during the Cold Start procedure as modelled in the HPT. From left to right of the figure, one is able to observe the initial condition of the turbine at the start of the simulation as well as the localised heating of the unit during the first hour of the cold start procedure. This localised heating, in principle, is the reason that the flange heating system is so important to the safe start-up of the unit from cold conditions. Around 2 hours into the start-up it is apparent that the flange heating operation allows for the uniform heating of the entire flange leading to the on-load condition observed in the furthest right frame of the figure.

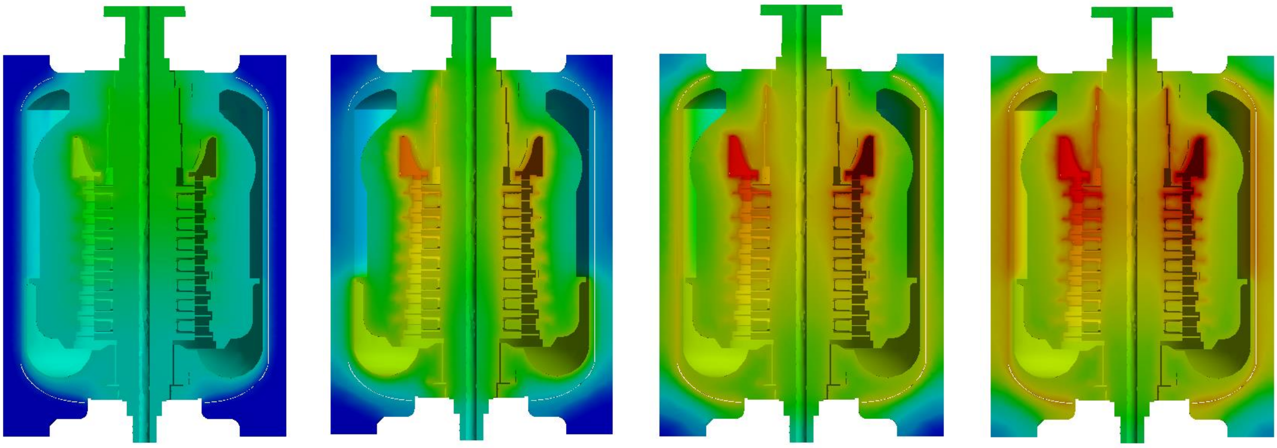

Initial Steam Admission (+30s)

Initial Heating (+50mins)

Flange Heating (2hrs)

On load (+3hrs)

Figure 116: HPT Temperature Gradients during Cold Start-up

Figure 117 demonstrates the agreement between the measured and reported flange temperatures. It confirms the validity of the flange heating approach. The error statistics of the Thermocouple H1 results shows a high level of agreement between the modelled and reported values, all falling within a narrow distribution between 0.05% to 6.39% absolute error.

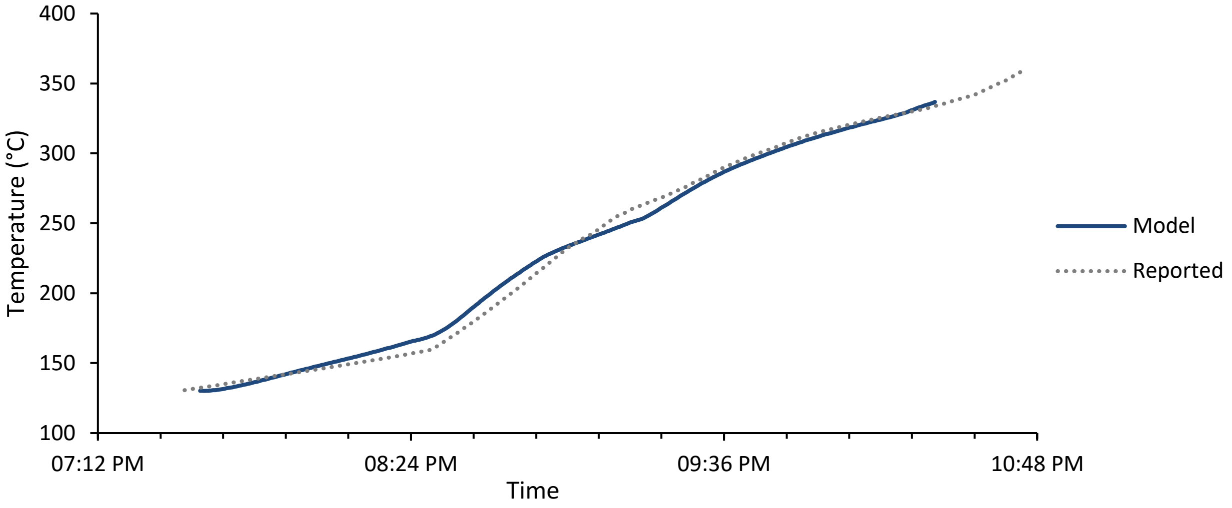

Figure 117: LH Flange Thermocouple (H1) Result

The result of the outer barrel thermocouple, Thermocouple H2, shows the highest error across the validating thermocouples. Whilst the maximum error falls below a 10% threshold, the trend observed from this thermocouple shows deviations from the reported values, as seen in Figure 118.

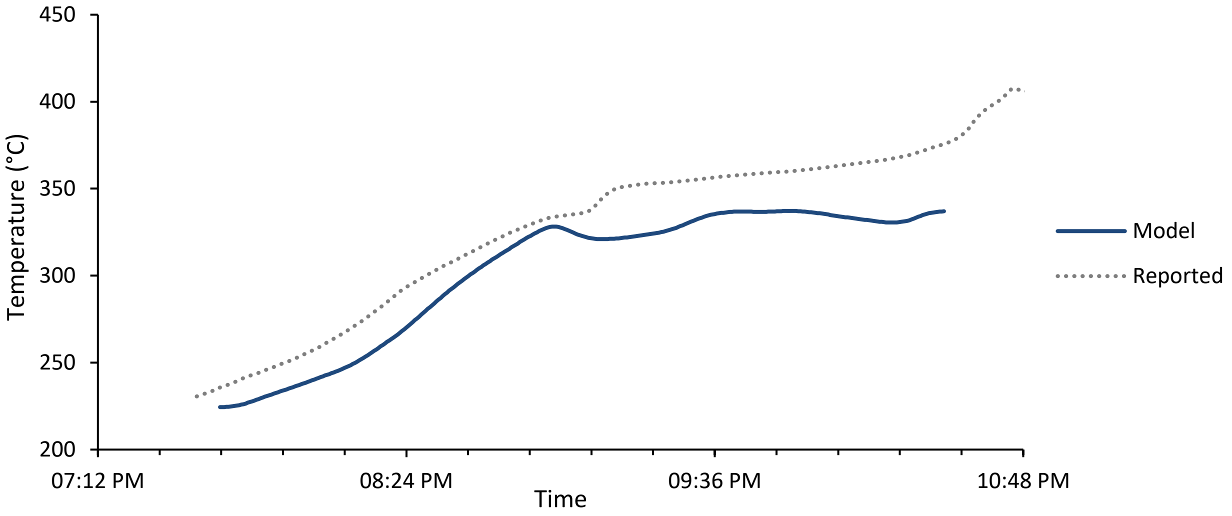

Figure 118: Outer Barrel Thermocouple (H2) Result

Possible reasons for the reduced correlations are the simplifications made in modelling the casing space region between the Inner and Outer casing into one heat transfer component. The modelling of the barrier plate as a single stage labyrinth seal also proved complex to calibrate towards replicating the reported temperature across the outer cylinder.

The results shown for Thermocouple H4, are significant in the fact that they validate the temperature boundaries generated by the 1-dimensional Flownex Model. The validation suggests that the Turbine Stage Component is able to generate correct temperature profiles from given global boundary conditions for transient simulations. The majority of the data points in Figure 119 fall within an 8% error range, with the remaining points being accounted for by the first hour of the start-up. This lack of correlation can be accounted for in the limitations presented in the exhaust steam temperatures, which were also significantly lower than report values.

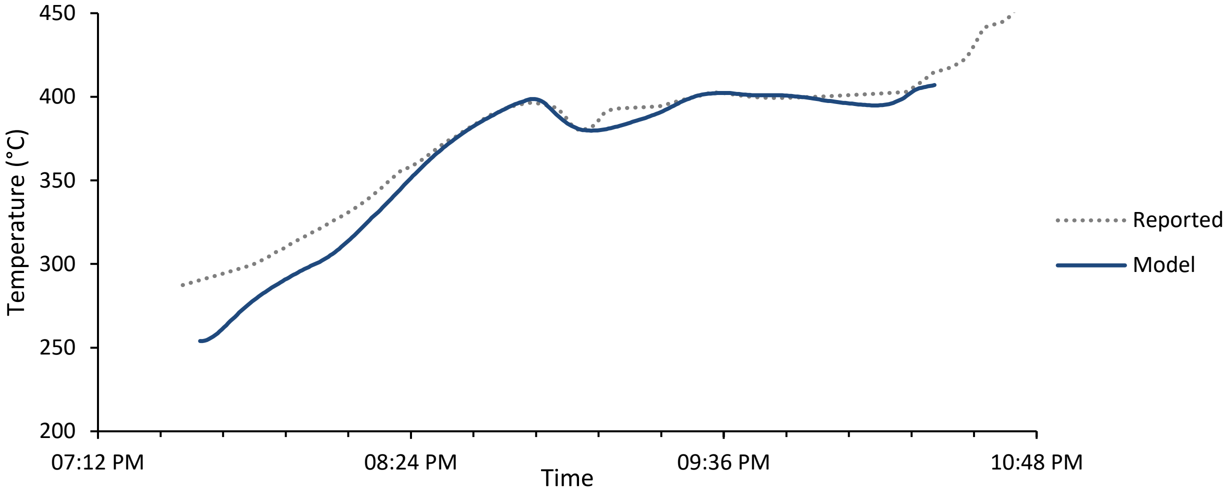

Figure 119: Inner Casing Thermocouple (H4) Result

Looking at the IPT, the validation was more difficult because of the uniform metal temperature assumption made as the initial condition. The validation of the thermocouple result from the inlet plane inner metal temperature, Thermocouple I3, is shown below.

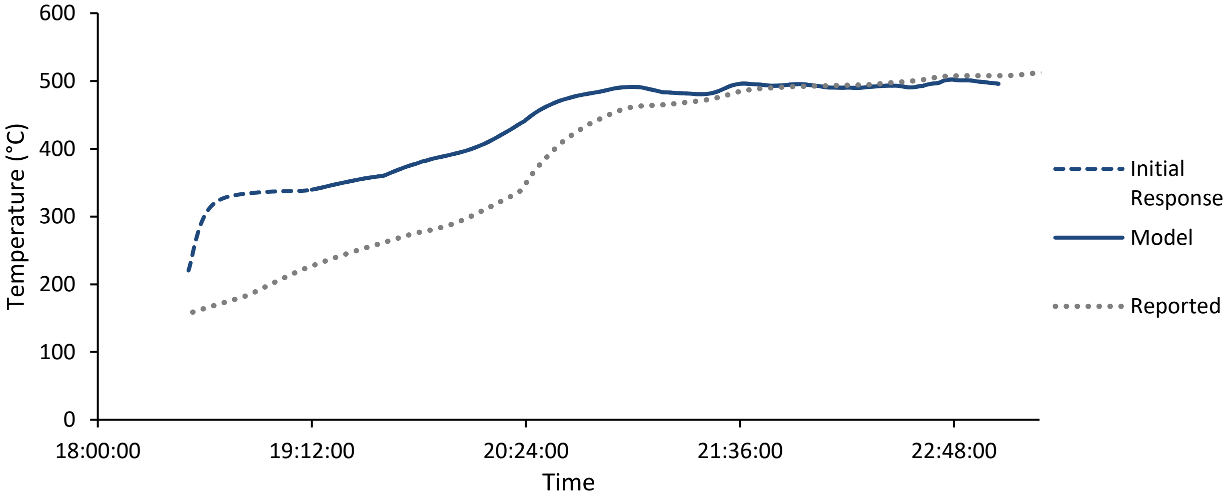

Figure 120: Inner casing, Thermocouple I3, temperature during Cold Start

The thermocouple result yielded some interesting conclusions. The steep initial response of the thermocouple can be attributed to the use of surface boundary conditions on the outer surface of the inner casing. Additionally, the reported data seems to suggest that a more gradual heating of the outer surfaces is more likely, possibly exposing a shortcoming of the surface temperature boundary condition. It is possible that a convective boundary condition would be more appropriate for the IPT, especially considering the low mass flow conditions in the initial start-up. This finding is confirmed in that, as the start-up progressed, with increasing mass flow through the IPT, the temperatures converge after a period of consistent temperature trends. A similar trend is also observed in the loop pipe, Thermocouple I2, below.

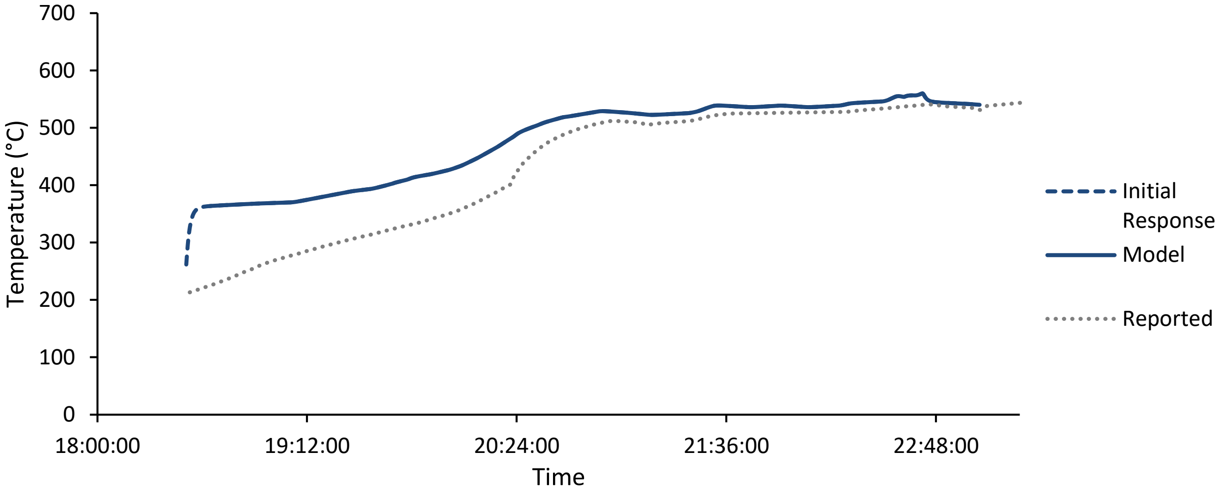

The validation of the IPT thermocouple suggests that convective boundary conditions would be more appropriate for the IPT modelling considering the mass flow range experienced during cold start-up. However, this would have significant impacts on the modelling expectations of the IPT model. These include:

- An increase in the computational time of the IPT model, in solving the convective boundaries as discussed in Chapter 5.5
- An increase in the attention paid to the establishment of the IPT model as small interferences and volumes were found to hinder convergence of the FEA solver

Whilst adjusting the thermal boundary conditions would improve the accuracy of the IPT model, as can be seen in the following differential expansion validation, one is still able to get a good understanding of the thermal boundaries and subsequent thermal expansion given the surface boundary condition assumption.

5.8.4 Differential Expansion validation

The validation of the structural behaviour of the HP and IP units was determined by the comparison of the deformation of the models relative to the on-site differential expansion measurement. The measurement of this quantity is the axial expansion of the turbine pedestal relative to the rotor collar, measured through a magnetic induction sensor, as shown in Figure 121.

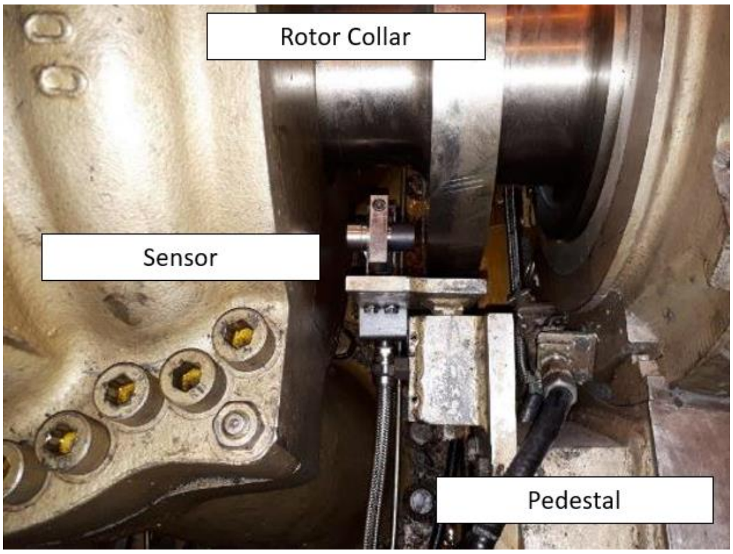

Figure 121: Differential Expansion measurement configuration

The measurement of this relative movement is described by the following equation:

$$\Delta z = z_{pedestal} - z_{rotor} \tag{5.2}$$

A positive Δz reading indicates widening of the gap between the pedestal and the rotor collar and the negative Δz reading indicating a reduction in that gap.

The validation of the differential expansion of each unit served as a final validation of the paired modelling approach undertaken in this study. The differential expansion validated the representative structural boundaries used in both turbine models as well as the flange heating calibration undertaken in the study.

As shown in section 5.8.2, there is a slight difference between the reported and measured initial differential expansion. In order to better compare the overall results with the measurements, the measurements were all offset by the difference in initial condition. As such, the results of both turbines start exactly at the same expansion as the measurement. The offset differential expansion of both units is shown in Figure 122 and Figure 123.

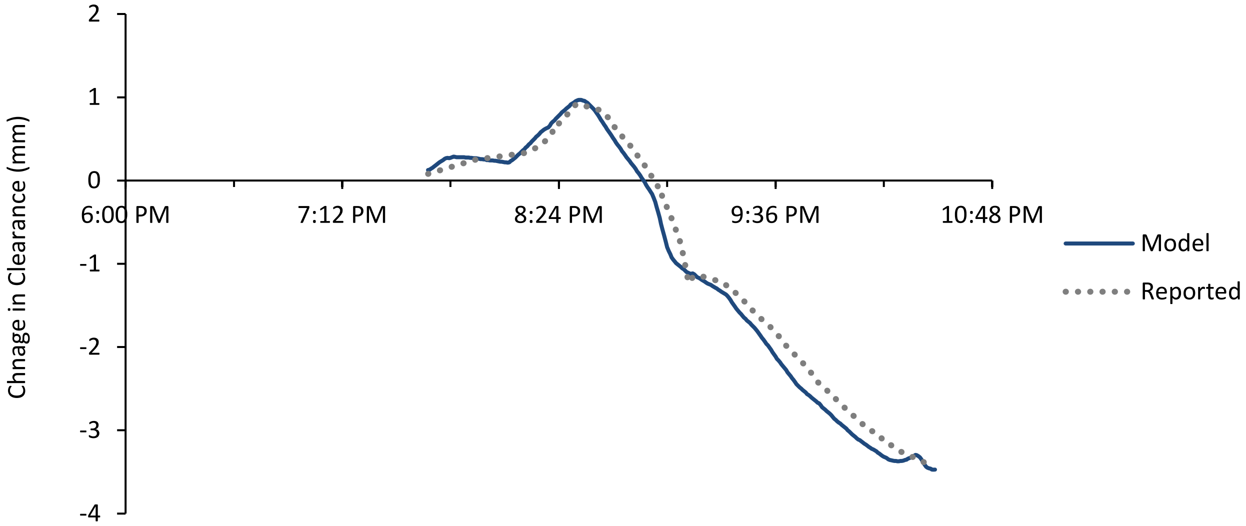

Figure 122: Offset differential expansion in HPT unit

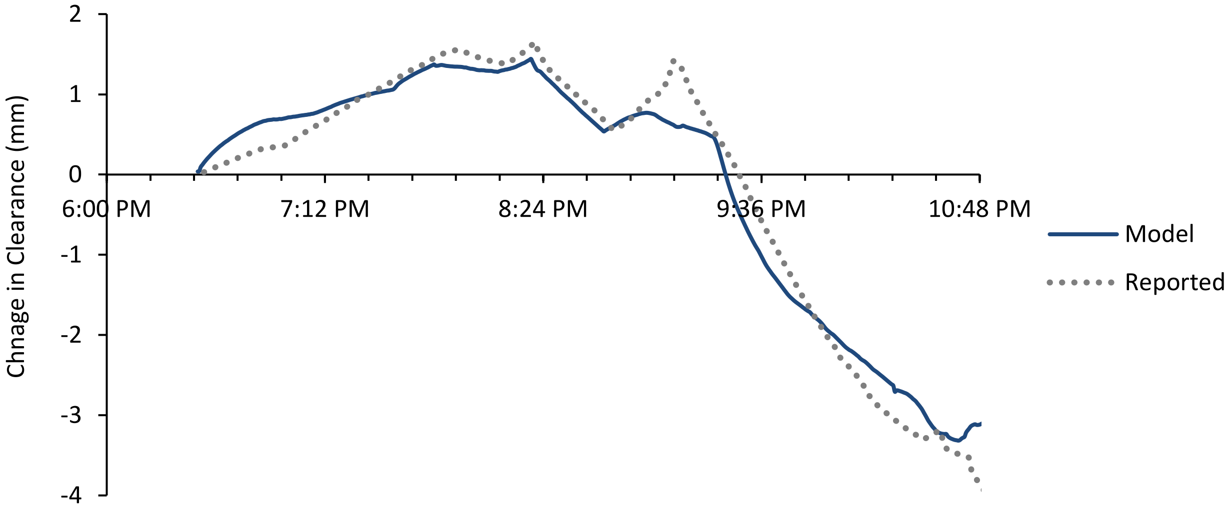

Figure 123: Offset differential expansion in IPT unit

The above results provide strong confidence in the validity of the paired modelling approach as well as the additional calibrations performed on the 3D FEA model. However, it is worth noting the divergence of the predicted differential expansion at approximately 21:00 in the IPT validation. The inability of the model to predict this sharp increase in the reported differential expansion is attributed to two factors. Firstly, the potential shortcomings of the choice of surface temperature boundaries in the IPT model, as discussed in the thermocouple validation of the previous chapter. Secondly, the potential limitations which exist in estimating the flange volumes for both turbines is exacerbated in the IPT due to the unit's significant size. It is more than possible that an under estimation of the IPT flange volume has led to insufficient thermal inertia and as such an inability of the model to predict the increasing differential expansion evident in the reported data. Despite this, the agreement of the remaining periods demonstrates the efficacy of the paired modelling methodology as a whole.

It was found that the flange heating system in both units contributed significantly to the relative expansion of the pedestal against the rotor, which will be discussed in a later chapter. Some specific conclusions can be made:

- The **material selection** undertaken at the initial FEA model establishment is sound as the material response of significant turbine components, namely the rotor and outer casing, is consistent with the observed behaviour on site.
- The **temperature boundaries prescribed by the 1D turbine model** are accurate to those found in the actual unit, shown by the close agreement of the expansion values during the first hours of both unit validations. This agreement is purely a function of the prescribed temperatures as the flange heating system is yet to have an effect during these time periods.
- The relative expansion of significant components agreeing with reported data also provides significant **confidence in the behaviour of unknown clearances** over the course of the start-up. These clearances include rotor tip, stator root and gland seal clearances – which will be discussed in the next chapter.

The differential expansion validation constituted the last validation undertaken in the establishment of the turbine models for the HPT and IPT units and confirmed that the paired modelling approach undertaken in this study was effective in generating a computational inexpensive model of a commercial steam turbine.

6. Case studies and Findings

The purpose of this chapter is to demonstrate the possible case studies which one could perform using the paired modelling approach. The findings of these case studies are illustrative as opposed to conclusive with regards to the candidate turbine unit.

6.1 Efficiency due to unit age

Calibrating the loss coefficient between the heat balance and load change validation gave rise to the classification of the turbine as a “new” (as per heat balance) or “aged” condition as the loss coefficient had increased. From this approach it was possible for one to quantify the power loss attributed to the aging of the turbine unit. This ability is demonstrated in the steady state results of a nominally 60% load case for the aged turbine model, shown in Figure 124 below:

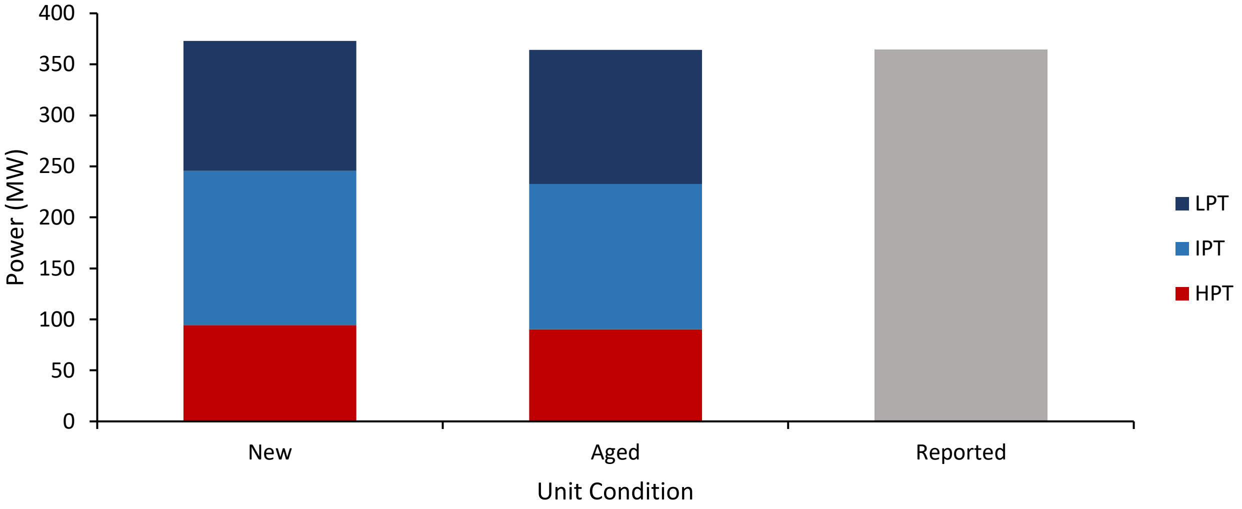

Load	New	Aged	Reported	Power Loss
Unit Power Output	373.10	364.03	364.34	2.4%

Figure 124: Power loss as a result of aging captured by the 1-dimensional turbine model

The above results demonstrate the importance of obtaining real plant data from the candidate unit to be used in the initial calibration of the model to obtain accurate predictions. Whilst heat balance diagrams, typically developed by the OEM, are based on design conditions the reported plant data plays a vital role in accurate steam turbine model allowing one to perform eventual off-design analysis.

This finding also points to the efficacy of the nozzle model in capturing subtle changes in the unit over its useful life, which could potentially be used in lifecycle analysis and asset management of the unit.

6.2 Radial Clearance Behaviours

A main motivator for this study was the ability to predict clearances which are impossible to measure during normal operation. The observations made on a site visit at the start of this study indicated evidence of component interference, seen in Figure 28, and it was hypothesised that the occurrence of such rubbing was as a result of transient operations, such as start-ups. Given the validation of the paired turbine modelling approach in the previous chapter, two important radial clearances could be considered for each turbine stage: the rotor tip and stator root clearance.

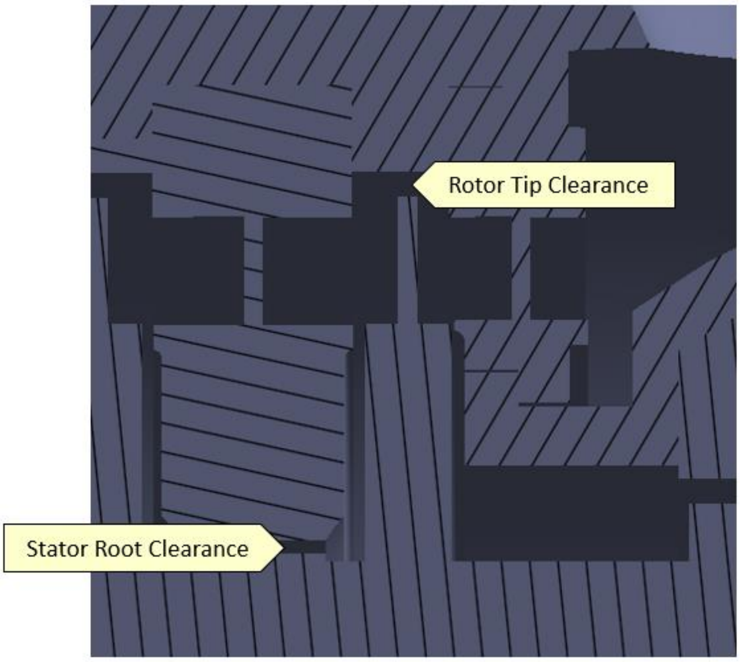

Figure 125: Location of Rotor Tip and Stator Root clearances

A key ability stemming from the method is the understanding of minimum cold clearances required for a turbine to operate efficiently and without risk of component interference. If the clearances under discussion were too large and underwent significant expansion, the efficiency of the relevant turbine stages would decrease as a result of the increased leak flow around the turbine stages. It is evident, therefore, that these clearances are fundamental to safe and efficient turbine operation.

The cold clearance measurements from the candidate unit are readily available from maintenance documentation due to the importance of such clearances. Figure 126, shows the minimum, maximum and average clearance during the full cold start-up procedure as well as these clearances relative to cold clearance specified for the unit.

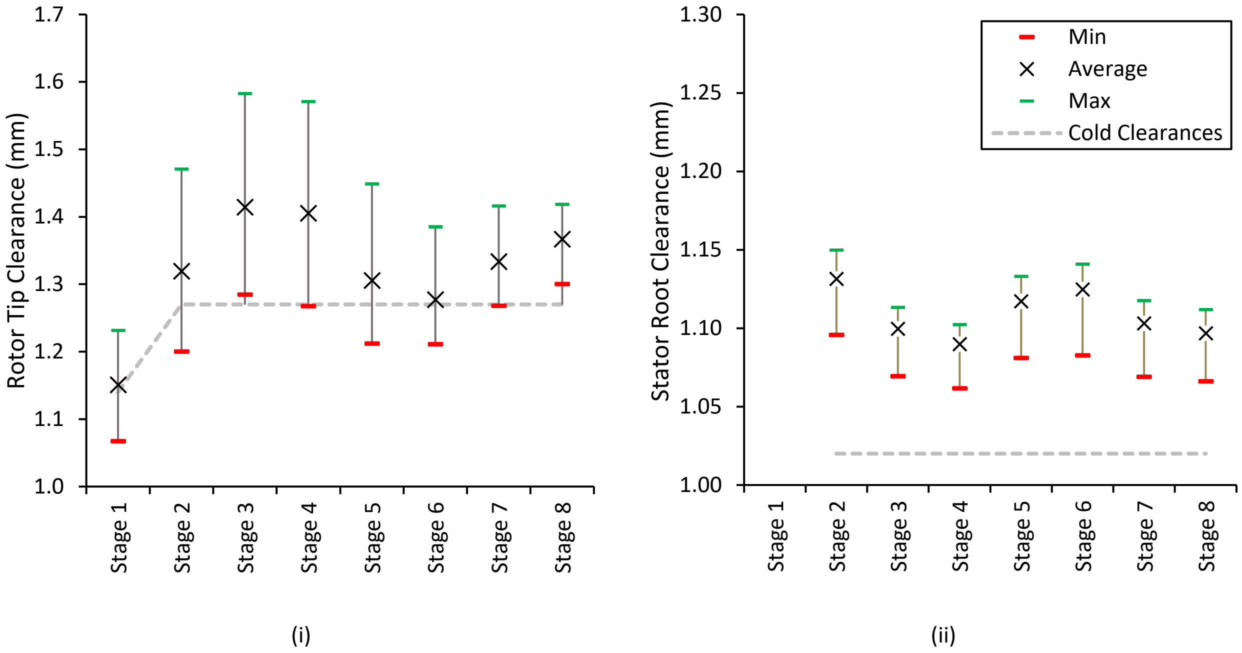

Figure 126: High Pressure Turbine (i) Rotor tip and (ii) Stator Root clearance ranges during Cold Start

From the above, the conservative approach often employed in the clearance specification of the high-pressure turbine is evident. In this unit, the results suggest that both clearances increase during the course of the cold start-up procedure. The largest reduction in clearance is observed in the rotor tip clearance of the first stage, marking a 6% reduction clearance at the minimum clearance value. All of the average clearances across the stages sit above the cold clearance value with up to a 24% increase in the clearance being observed at the third stage.

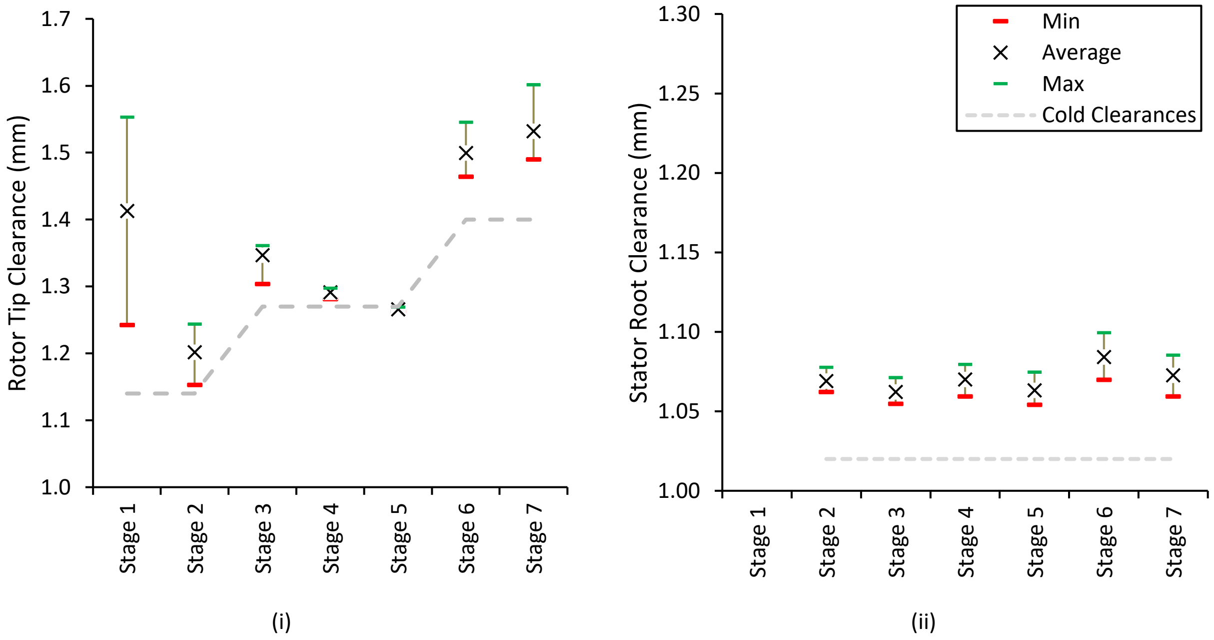

Figure 127: Intermediate Pressure Turbine (i) Rotor tip and (ii) Stator Root clearance ranges during Cold Start

Looking at the Intermediate Pressure Turbine a similar trend is observed as in the High-Pressure Turbine. The rotor tip and stator root clearances tended towards increasing over the course of the cold start-up, indicating the possibility for a reduction in efficiency of the unit. However, observations were made which were unique to the IPT itself.

Firstly, the first stage shows the largest clearance distribution across both HP and IP turbines, which could be attributed to the cooling flow interacting with the superheated inlet steam at the first stage. The clearance distribution could also point to large radial stresses being promoted in the rotor and diaphragm at this region given the large distribution of clearance, despite stress considerations falling outside the scope of this study.

Secondly, the reduction in the stator root clearance distribution in the IPT versus the HPT is shown, which could be symptomatic of the significant increase in size and thermal mass which is present in the IPT relative to the HPT. As found by Topel, rotor, stator and casing components were the predominant components impacting the expansion characteristics of steam turbines [16]. It follows therefore that, given the size increases of all these components between the HPT and IPT, one would expect a difference in the thermal expansion behaviours between both units.

Thirdly, the clearance distribution surrounding the extraction flow found in the IPT between the fourth and fifth stage is peculiar. One can observe that the clearance distribution decreases as one approaches the extraction point to such an extent that there is virtually no variation in clearance. The likely reason for this small variation is the configuration of the extraction point. Figure 128, demonstrates that the extraction steam interacts with the outer surfaces of the inner casing in addition to the diaphragm and rotor of the fourth stage itself. Given equal temperature boundaries on the inner and outer surfaces, it would be expected that differential expansion between the rotor and diaphragm would be reduced at this location.

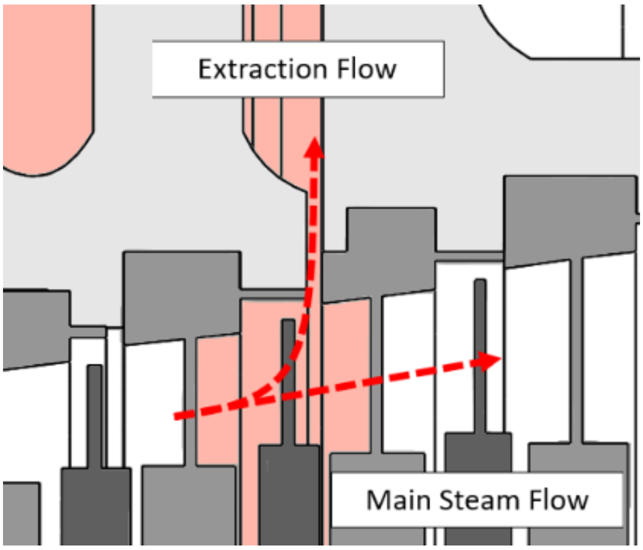

Figure 128: Extraction temperature boundary in IPT FEA model

The finding made in the IPT, around the extraction point, speaks to the accurate capturing of the steam-surface interactions and the validity of the modelling methodology presented in this study in modelling complex peripheral steam flows. An overarching conclusion which can be demonstrated from the above analysis is the ability of the paired turbine model to predict clearances which were previously impossible to quantify in operational steam turbines. Studies like these would enable maintenance and site engineers to evaluate their choice of cold clearance relative to the expected transient operations expected of the unit, leading to increased efficiency and availability.

6.3 Shortened Cold Start Period

Another strong motivation for developing this modelling methodology is to increase the flexibility of conventional steam turbines away from a consistent base-load operating approach. This would see the introduction of more transient operations, possibly leading to more start-ups being completed. A reduced start-up duration of turbine units will become quite beneficial in these scenarios. In this study three start-up periods were considered:

- **Normal Cold Start:** a control replicating the full cold start-up as reported from the plant data provided, lasting approximately **4 hours**.
- **Intermediate Cold Start**: a shorter start-up with a 50% reduction in the period from “cold” to on-load condition, lasting approximately **2 hours**.
- **Fast Cold Start**: the shortest start-up with a 25% reduction in the start-up period, lasting approximately **1 hour**.

Below is the differential expansion results for the three start up periods:

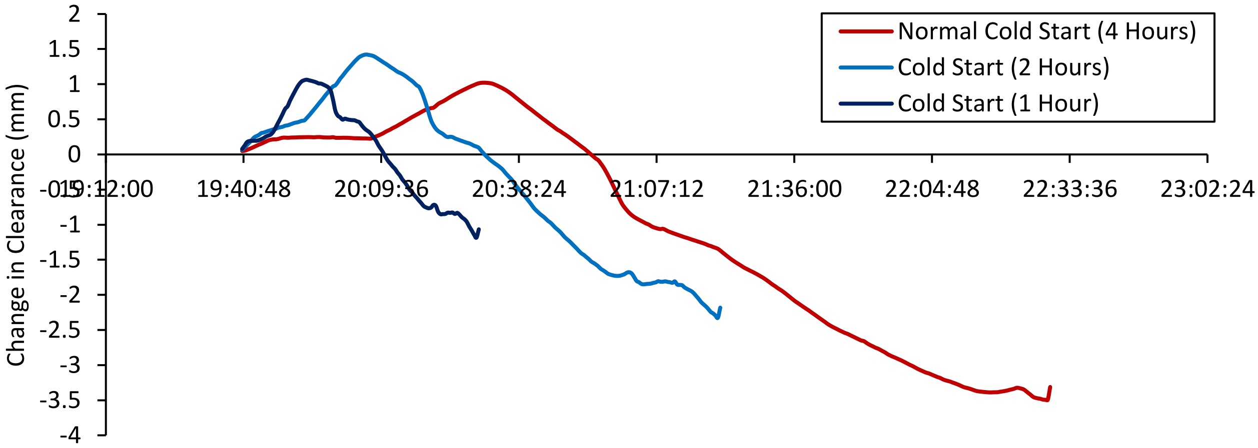

Figure 129: HPT Differential Expansion Values during three varying Cold Start-up periods

One might be led to assume that the fastest cold start would lead to the largest differential expansion value, but as can be seen from the results, this is not the case. The rate at which the temperatures change in the fast cold start, leads to a limited time in which heat can be transferred from the steam to the surrounding components, leading to a reduction in the relative expansion of those components. This is not to say that the fast Cold Start is by any means feasible, as the current modelling methodology does not consider the thermal stresses promoted in each component. A refinement of the current modelling methodology, including fasteners and more complex structural boundaries could allow one to perform a stress analysis on the turbine components, as in the work of Bakhmutska [10].

Radial expansion is also a concern in the flexible operation of steam turbines. Figure 130, shows the distribution of the rotor tip clearances during the two shortened start-ups. Similar to the normal cold start, the trend indicates an opening of the rotor tip clearances. For the intermediate cold start, significant clearance increases were seen in the first four stages with the largest of these being almost 30% of the original clearance (29.4%) occurring at the third stage. For the fast cold start, a similar trend is observed. The expansion bears a resemblance to the normal cold start-up trend except that there is an increase in the clearances in the last two stages.

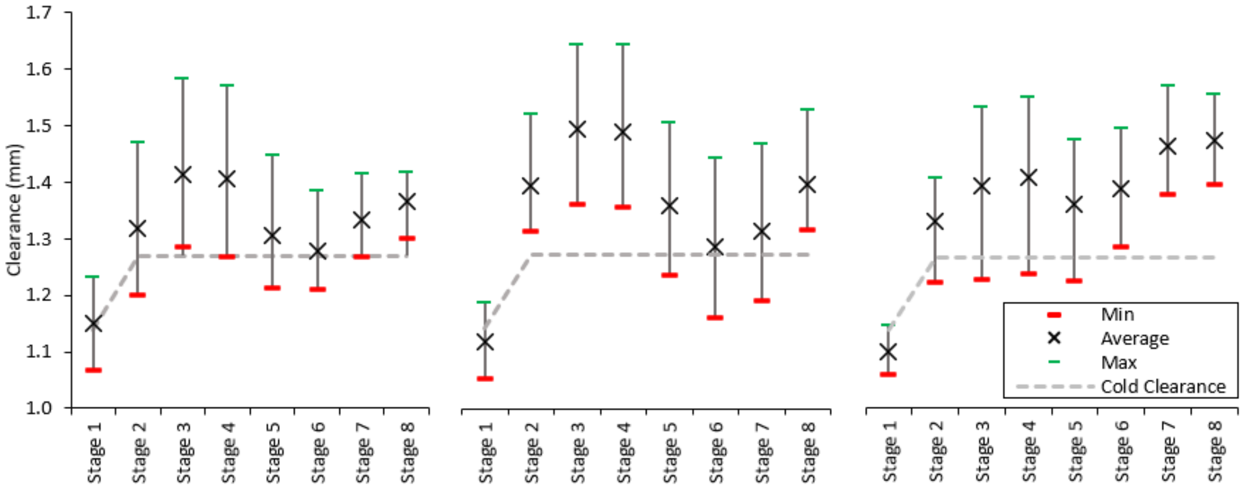

(i) *(ii)* *(iii)*

Figure 130: (i) Normal (ii) Intermediate and (iii) Fast Cold Start HPT Rotor Tip Clearances

The same analysis was performed on the IPT unit, with the same three start-up speeds, and with the following results:

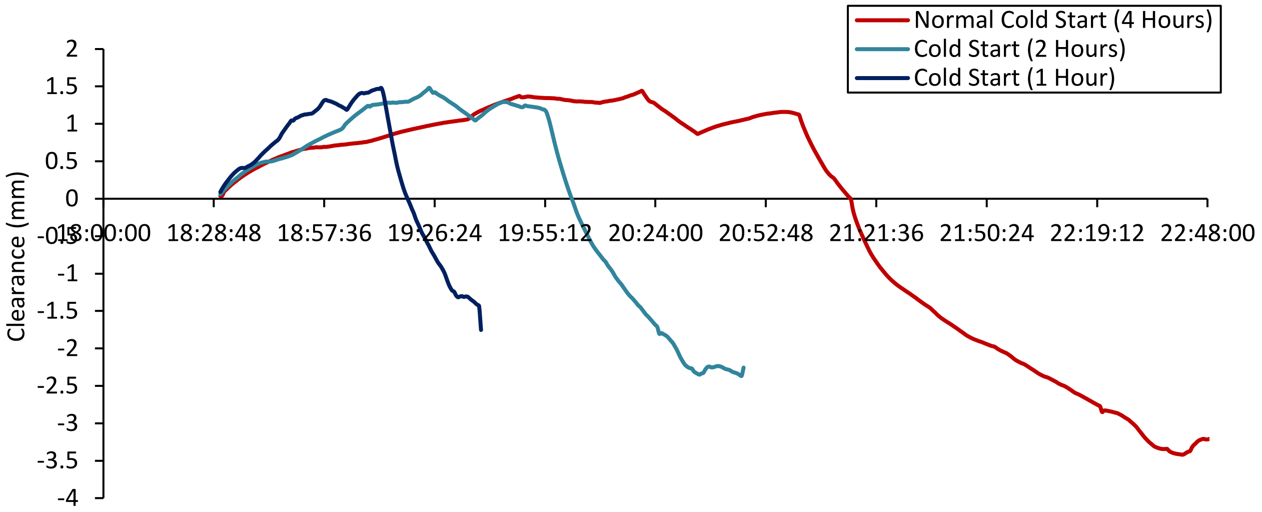

Figure 131: IPT Differential Expansion Values during three varying Cold Start-up periods

The differential expansion trends observed in the IP turbine differed from those of the HP turbine. The maximum differential expansion value remained relatively consistent across the three start-up periods. Considering that the same relative flange heating loads were applied across the three periods, not much difference could be found between the simulations. This leads one to conclude that the sensitively of the IP turbine to thermal load changes is less than the HP turbine. A likely reason for this difference is the thermal mass present in the IP turbine relative to the HP turbine, as seen in Table 17. Of particular importance is the total volumetric increase across the HP and IP turbines, particularly in the rotor.

Table 17: Volume Comparison of major turbine components of HP and IP units

	HPT (m^3)	**IPT (m^3)**	**% Increase**
Rotor	0.0304	3.137	10 219
Inner Casing	2.905	3.837	32
Outer Casing	7.960	11.86	48

Whilst the axial deformation of the IPT is demonstrated consistent between the different start-up periods, the radial expansion of the IP rotor shows more significant changes. Figure 132, shows the rotor tip clearances across the three start-up periods

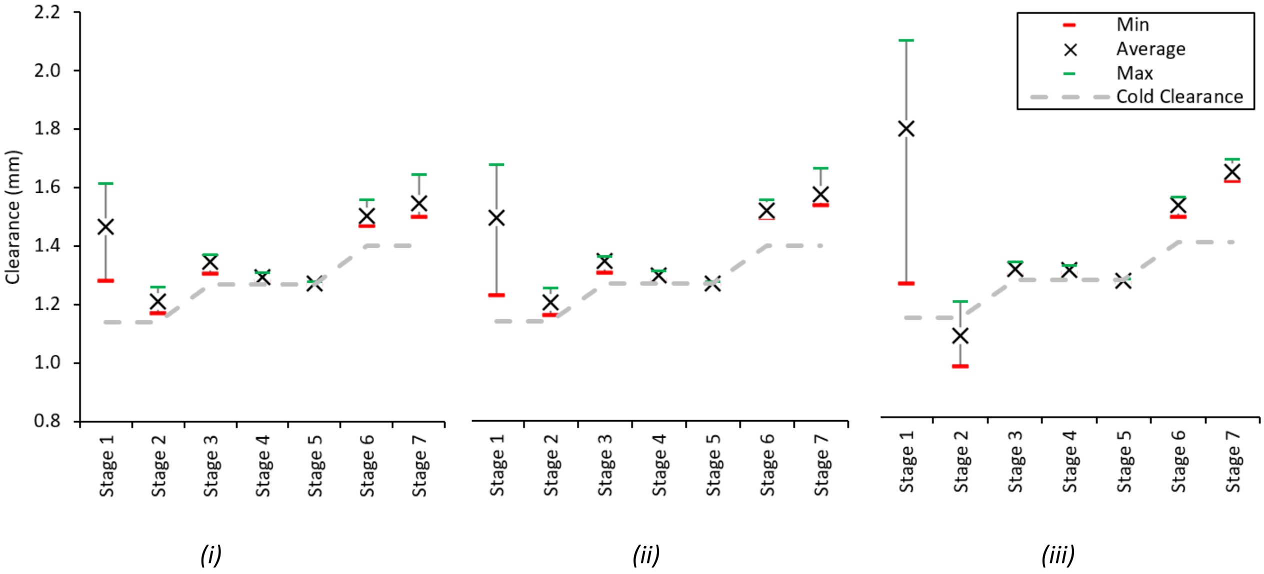

Figure 132: (i) Normal (ii) Intermediate and (iii) Fast Cold Start IPT Rotor Tip Clearances

Looking at the clearance behaviours confirms, as in the HP turbine, a sensitivity of the first stages of the unit towards fluctuating clearance behaviour. Of particular importance was the decrease in the clearance in the second stage rotor tip in the fast start-up, and the increase in the clearance range of the first stage for the same start-up. For the remaining stages of the IP turbine, the deviation of the clearance behaviour is significantly less than the first two stages.

A valuable lesson from this study is the sensitivity of the first stages' clearances to start-up rate.

6.4 Cooling Flow

The modelling of the Intermediate Pressure Turbine cooling flow was undertaken during the initial 1D modelling of the turbine process. Following the establishment of the model, an investigation into the effect that this cooling flow had on the thermal expansion and subsequent clearance behaviours was undertaken. Figure 133, shows the temperature gradients promoted around the cooling flow path during the investigation.

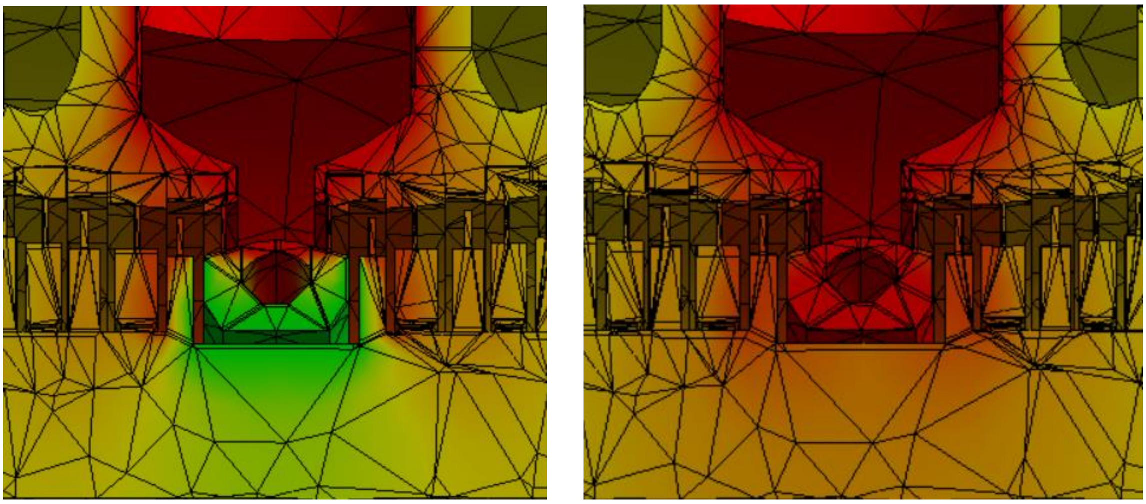

(i) *(ii)*

Figure 133: IPT First Stage Temperature gradients (i) With and (ii) Without Cooling flow

Of importance during this case study, was evaluating the structural response of the IP rotor in the absence of the cooling flow boundaries. Figure 134, shows the rotor tip clearance between the cooled and non-cooled simulations.

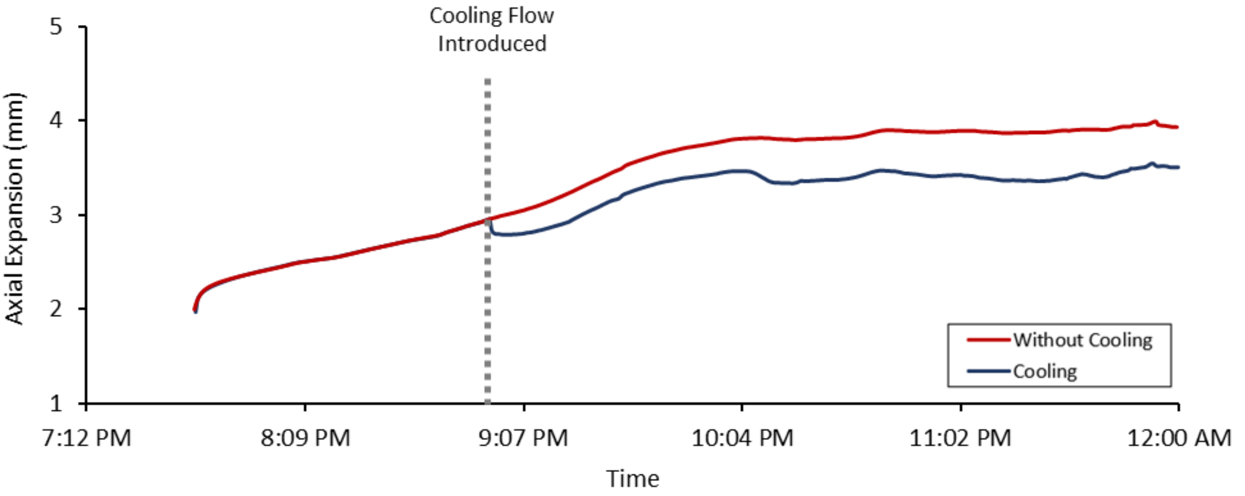

Figure 134: Axial clearance (i) With and (ii) Without Cooling Flow

Figure 134, demonstrates the direct correlation of the IP rotor axial deformation to the cooling flow introduction. One can observe that the axial expansion of the rotor is more for the heated case than in the non-heated case. Of interest, based on the finding of the previous case studies was the effect that the cooling had on the first stage radial clearances. Figure 135, shows the clearance distribution for both simulations.

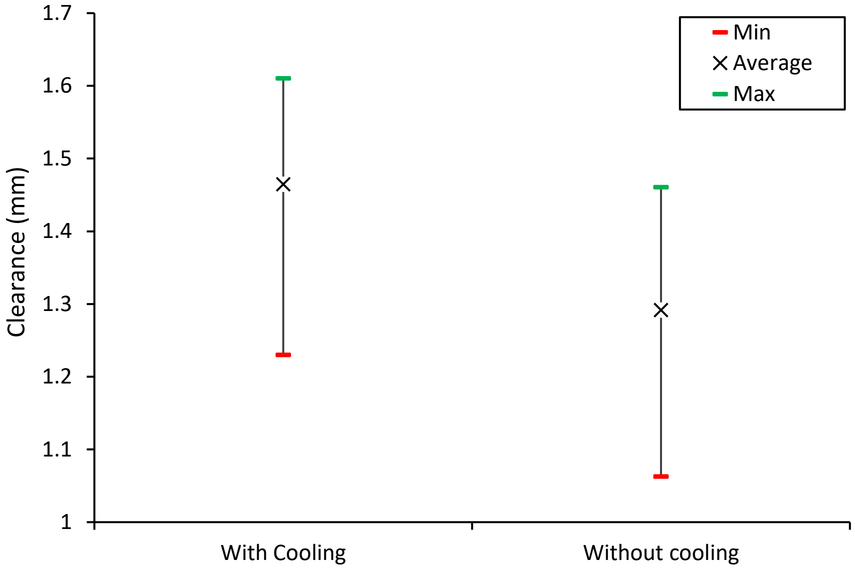

Figure 135: 1st Stage rotor tip clearances

In the non-cooled case, the clearance distribution shows a minimum clearance less than that of the cold clearance specified for the unit (approximately 1.17 mm). Whilst the primary reason for the cooling flow is driven by thermal stress control, the analysis suggests that the cooling flow “narrows” the clearance distribution of the first stage rotor tip and also plays a small role in preventing the closing of the rotor tip clearance over the course of the cold start-up

7. Conclusions and Recommendations

7.1 1D Model Conclusions

This project demonstrated that it is possible to develop a 1D Turbine Model, using the Nozzle Analogy theory to predict the stage-by-stage fluid temperatures which exist during transient turbine operation. Representative modelling of the peripheral turbine flows was also captured in the 1D Turbine Model including gland seal, internal casing and cooling flows featured between the HP and IP turbine units. This was achieved with very little geometric input from turbine OEM's, utilising turbine data readily available for site engineers at an Eskom Power Plant. An unexpected finding from the 1D Model was the effect that the nozzle loss coefficients had, and the importance of this variable to be well calibrated in achieving representative temperature gradients based on actual unit condition.

In order to reduce the number of model input boundary conditions for the 1D model, it was necessary to develop a complete Rankine Cycle process model that links up with the turbine models. In this way only a very few set of inputs was required to enable to calculation of the entire start-up transient. This process model was easily developed using the specialised custom ATProM compound components.

7.2 1D Model Recommendations

Recommendation 1:

The initial calibration of the multistage turbine should be automated to allow for quicker modelling. This can be in the form of the Designer function in Flownex SE, or the development of an Python script which can execute instances of the steady state full load case and converge to the optimum correction factors.

Recommendation 2:

The approach taken in modelling the bypass procedure in the initial stages of the start-up could be refined. Such refinement would allow for the modelling of the transition of the turbine system from having the HP bypass system in operation to the main steam admission into the HPT.

Recommendation 3:

Further discretisation of the internal casing flow heat transfer modelling is also recommended. In the later validation of the 3D FEA model in this region it was discovered that having a more detailed temperature gradient extending from the barrier plate would likely lead to more accurate validation.

7.3 3D Model Conclusions

The development of a 3D FEA Model was also successful in allowing one to gain insights into the thermal and structural response of steam turbines during the cold start-up procedure. Whilst difficulties were experienced in developing the initial conditions of both the HP and IP units, the transient response of the units during the thermal and structural simulations were sufficiently accurate to allow for the validation of the resulting models against plant data.

It was also found that the validation of the 3D turbine model also added confidence to the 1D Turbine model by confirming the stage-by-stage temperature results. The investigation of appropriate temperature boundary definitions in the FEA analysis was explored and whilst the surface temperature boundary was opted for, shortcomings in the IPT modelling suggested that convective boundaries would've been more appropriate.

Additionally, whilst most significant in the study of low-pressure turbines, the role of centrifugal forces on radial expansion was considered not significant in the structural modelling of the HP and IP turbines in this study. Upon reflection, given the role this effect has in turbine machinery as a whole, further investigation of centrifugal effects should be prioritised in future studies.

The 3D Turbine model successfully predicted the expansion of the rotor relative to the casing as well as allowed investigations regarding the internal clearance of the rotor tip and stator root for the Cold Start-Up, even at accelerated start-up rates. This therefore met one of the primary objectives of the study as a whole.

The one major unforeseen drawback was the significant role which the flange heating system played in the overall results. An undesired amount of calibration was needed to achieve the correct results. This detracts from the otherwise minimal input approach in setting up and solving the transient response.

7.4 3D Model Recommendations

Recommendation 1:

Convective thermal boundary conditions should be used in the IPT model, given the initial introduction of steam into the unit at extremely low mass flows. This would allow more gradual heating of the turbine components during initial start-up phases.

Recommendation 2:

More attention should be given to ensuring the capturing the geometry of components with significant mass, such as turbine flanges.

Recommendation 3:

The mass flows entering the flange heating system should be obtained from plant data. One might only be able to retrieve an ON/OFF signal from the plant data, which should then be translated via a thorough pressure drop model to an equivalent mass flow, as well as the likely heat transfer coefficient present in the flange cavities.

Recommendation 4:

Given the limitations imposed by selecting a pure temperature boundary condition, refinement of the model such that convective boundaries be applied at the beginning of a run and a transition to temperature boundaries where appropriate would likely improve the validity of particularly the IPT model.

7.5 Concluding Remarks

The methodology developed in this study allowed one to comprehensively model the complex Cold Start-Up procedure in an operational steam turbine. The modelling approach allowed for the computationally inexpensive prediction of transient clearance behaviours, especially clearances which are impossible to measure in operation. The knowledge gathered from this study in the complexities of modelling steam turbine units of this size are significant to the field of steam turbine modelling with industrial relevance. Given the success of this method, the application of this method within turbine operations in South Africa could yield invaluable results as plants move toward flexible operating approaches.

8. List of References

[1] W. F. Fuls, “Accurate stage-by-stage modelling of axial turbines using an appropriate nozzle analogy with minimal geometric data,” *Appl. Therm. Eng.*, vol. 116, pp. 134–146, 2017, doi: 10.1016/j.applthermaleng.2017.01.048.

[2] W. F. Fuls, J. S. Clark, and A. C. Marx, “Application of the nozzle analogy to easily predict steam turbine performance with minimal geometric input,” *Proc. ASME Turbo Expo*, vol. 8, 2019, doi: 10.1115/GT2019-90891.

[3] S. J. Mills, *Integrating intermittent renewable energy technologies with coal-fired power plant*. 2011.

[4] C. Calitz, Joanne; Bischof-Niemz, Tobias; Mushwana, “Statistics of utility-scale solar PV and wind in South Africa in 2015,” no. May, p. 94, 2016, [Online]. Available: http://www.csir.co.za/docs/Statistics of Wind and Solar PV in South Africa in 2015 - CSIR - FINAL.pdf.

[5] CSIR Energy Centre, “Least-cost electricity mix for South Africa until 2040 Presentation,” in *Windaba 2016 conference*, 2017, no. November 2016.

[6] Eskom, “Eskom ’ s generation plant mix,” *COP17 fact sheet*, 2002. Available: https://www.eskom.co.za/wp-content/uploads/2021/09/GX-0001-Generation-Plant-Mix-Rev-23.pdf

[7] A. Leyzerovich, *Steam Turbines for Modern Fossil-Fuel Power Plants*. The Fairmont Press, 2008.

[8] P. Denholm, M. O’Connell, G. Brinkman, and J. Jorgenson, “Overgeneration from Solar Energy in California: A Field Guide to the Duck Chart (NREL/TP-6A20-65023),” *Tech. Rep.*, no. November, p. 46, 2015, [Online]. Available: http://www.nrel.gov/docs/fy16osti/65453.pdf.

[9] C. Henderson, “Increasing the flexibility of coal-fired power plant.pdf.” .Available: https://usea.org/sites/default/files/092014_Increasing%20the%20flexibility%20of%20coal-fired%20power%20plants_ccc242.pdf

[10] J. O. Bakhmutska, V. N. Goloshchapov, and R. Kochurov, “Rotor Heating Conditions Influence on the Thermostructural State and Lifetime of the 325 MW Steam Turbine During Start-Ups,” *Bull. Natl. Tech. Univ. «KhPI» Ser. Dyn. Strength Mach.*, vol. 1, no. 39, pp. 89–94, 2017, doi: 10.20998/2078-9130.2017.39.115774.

[11] L. Moroz, B. Frolov, and R. Kochurov, “Steam Turbine Rotor Transient Thermo-Structural Analysis and Lifetime Prediction,” pp. 1–8, 2016.

[12] D. Born, P. Stein, G. Marinescu, S. Koch, and D. Schumacher, “Thermal modeling of an intermediate pressure steam turbine by means of conjugate heat transfer - Simulation and validation,” *J. Eng. Gas Turbines Power*, vol. 139, no. 3, 2017, doi: 10.1115/1.4034513.

[13] D. Mukhopadhyay, H. M. Brilliant, and X. Zheng, “Development of a conjugate heat transfer simulation methodology for prediction of steam turbine cooldown phenomena and shell deflection,” *Proc. ASME Turbo Expo*, vol. 5C, no. June 2014, 2014, doi: 10.1115/GT2014-25874.

[14] G. Marinescu, M. Sell, A. Ehrsam, and P. B. Brunner, “Experimental investigation into thermal behavior of steam turbine components. Part 3 - Startup and the impact on LCF life,” *Proc. ASME Turbo Expo*, vol. 3 C, no. April 2020, 2013, doi: 10.1115/GT2013-94356.

[15] G. Marinescu, P. Stein, and M. Sell, “Natural cooling and startup of steam turbines: Validity of the over-conductivity function,” *J. Eng. Gas Turbines Power*, vol. 137, no. 11, 2015, doi: 10.1115/1.4030411.

[16] M. Topel, *Steam Turbine Thermal Modeling for Improved Transient Operation*. 2014.

[17] Flownex, “Flownex Library Theory Manual,” no. December, 2011, [Online]. Available: internal-pdf://flownextheoryhelp-1989977090/FlownexTheoryHelp.pdf.

[18] ANSYS Inc., “ANSYS Manual - Release 5.6,” *Theory Reference*, no. November. pp. 1–1286, 1999, [Online]. Available: http://research.me.udel.edu/~lwang/teaching/MEx81/ansys56manual.pdf.

[19] M. Banaszkiewicz, “Steam turbines start-ups,” *Trans. Inst. Fluid-Flow Mach.*, vol. 126, no. 126, pp. 169–198, 2014.

[20] J. Clarke and W. Fuls, “Low Load Operation of Turbine-Driven Boiler Feed Pumps,” no. September, 2019.

[21] D. Taler and J. Taler, “Simple heat transfer correlations for turbulent tube flow,” *E3S Web Conf.*, vol. 13, pp. 1–7, 2017, doi: 10.1051/e3sconf/20171302008.

[22] GEC, “GEC Operations Manual - Chapter 4: HP Cylinder.” .

[23] GEC, “GEC Operations Manual - Chapter 5: IP Cylinder.” .

[24] AZO Materials, “AISI 4140 Chrome-Molybdenum High Tensile Steel,” 2012. https://www.azom.com/article.aspx?ArticleID=6116.

[25] Modern Energetics, “Flange Sealing System,” *Turbine Plant Systems*, 2014. http://mda139.net/turbineplant/ffunction-and-system-layout.html.

[26] ANSYS, “The Fundamentals of FEA Meshing for Structural Analysis,” 2021. https://www.ansys.com/blog/fundamentals-of-fea-meshing-for-structural-analysis

Appendix A. Nozzle Area Calculations

A worked example of the Nozzle Area calculation is presented for the High-Pressure Turbine in the candidate unit selected for this study. Looking at the inlet and outlet conditions, the following conditions were found

Table 18: High Pressure Turbine inlet and outlet conditions

	Inlet	**Outlet**
Pressure (MPa)	16.1	4.1
Temperature ($^\circ$ C)	535	334
Enthalpy* (kJ/kg)	3396.99	3050.015
Entropy* (kJ/K.kg)	6.428	6.503

**Calculated values*

From the above conditions it was possible to derive the isentropic efficiency of the overall turbine as below:

$$\eta_s = \frac{h_{in} - h_{out}}{h_{in} - h_{s.out}} = 88\%$$

Where $h_{s.out}$ is the isentropic outlet entropy of the turbine using the outlet pressure and an isentropic assumption such that entropy remains constant across the unit.

$$h_{s.out}(P, s) = 3005.401 \ \frac{kJ}{kg}$$

The isentropic stage enthalpy drop was calculated, assuming an equal drop per stage. Given that the HP turbine had 8 stages (N_{stage}), the following was calculated:

$$\Delta h_s = \frac{h_{in} - h_{s.out}}{N_{stage}} = 48.949 \ \frac{\text{kJ}}{kg}$$

As explained in the main body of this dissertation, the initial derivation of the stator exit angle (α) and reaction ratio (R), were performed using the first stage. From the turbine diagrams collected from site as well as measurements taken on site, the following nominal turbine blade diameters were sourced

Table 19: First stage diameters

	Value
Outer diameter (mm)	1111
Inner diameter (mm)	960

Using these measurements, the mean diameter and blade velocity were determined for the stage as below:

$$d_m = \frac{1}{2} \cdot \left(d_{outer} + d_{inner} \right) = 1.035 \text{ m}$$

$$v_b = \frac{1}{2} \cdot d_m \cdot \omega = 162.656 \ \frac{m}{s}$$

Where $\omega = 314.156 \ \frac{\text{rad}}{s}$ for the turbine at full load at 3000 rpm

Assuming a purely impulse turbine stage (R = 0), a stage loading of ($\psi = 2$) could be derived. An assumption was made such that the maximum possible efficiency of the first stage could not surpass that of the overall isentropic turbine efficiency in order to solve for the probable stator exit angle in the equation below:

$$\Delta h_s = \eta_s \cdot \psi \cdot \left(\frac{v_b}{\cos \alpha} \right)^2 \rightarrow \alpha = 19.8^\circ$$

Given that the probably exit angle had been solved for, a nominal angle of 12° was assumed for all of the turbine stages. The isentropic enthalpy drop of each stage was derived using the above equation. The enthalpy drops across each stage is summed as follows:

$$\Delta h_{HP} = \sum_{n}^{n=N_{stage}} \Delta h_n$$

Given the initial stage sizing was performed on the first stage of turbine leads to a higher enthalpy drop across the unit as isentropically determined, further calculations need to be made. Given that a pure impulse stage is improbable in real turbine operation, the Reaction Ratio was iteratively solved, using the Goal Seek function on Microsoft Excel, for a non-zero value which would see convergence of the total isentropic enthalpy drop across the HP turbine.

$$\Delta h_{HP} = \sum_{n}^{n=N_{stage}} \Delta h_n \rightarrow R = 0.245$$

Table 20: HP First stage blade characteristics

	Value
Stator Exit angle (°) → assumed	$19.8 \rightarrow 20$
Reaction Ration	0.245

The above sizing allowed for a representative turbine stage to be derived for the remaining modelling. Given the non-zero reaction ratio, an enthalpy drop across the stator and rotor was expected as follows:

STATOR **ROTOR**

$$\Delta h_{stator} = \Delta h_s \cdot (1-R) = 36.96 \ \frac{\text{kJ}}{kg} \qquad \Delta h_{stator} = \Delta h_s \cdot R = 11.99 \ \frac{\text{kJ}}{kg}$$

Considering the stator the absolute and relative velocities can be solved, using the equations derived by Fuls [27], as below:

$$v_2 = \sqrt{2 \cdot \Delta h_{stator}} = 271.88 \ \frac{m}{s}$$

$$v_{2r} = \sqrt{{v_b}^2 + {v_2}^2 - 2 \cdot v_b \cdot v_2 \cdot \cos\alpha} = 131.4 \ \frac{m}{s}$$

From the isentropic enthalpy drop across the stator the stator exit density could be derived:

$$h_{st.out} = h_{in} - \Delta h_{stator} = 3360.03 \ \frac{kJ}{kg}$$

therefore

$$\rho_{st.out} = \rho(h_{st.out}, s_{in}) = 44.136 \ \frac{kg}{m^3}$$

Given the known full load mass flow, $\dot{m} = 501.207 \ \frac{kg}{s}$, the stator nozzle area could be derived as below:

$$A_{n.st} = \frac{\dot{m}}{\rho_{st.out} \cdot v_2} = 0.044 \text{ m}^2$$

For the rotor nozzle sizing the relative rotor exit velocity was solved for in the following equation derived by Fuls [1]:

$$v_{3r} = \sqrt{2 \cdot \Delta h_{rotor} + {v_{2r}}^2} = 184.77 \ \frac{m}{s}$$

In the same way as the stator the density at the rotor exit was determined as follows:

$$h_{r.out} = h_{st.out} - \Delta h_{rotor} = 3348.04 \ \frac{kJ}{kg}$$

Therefore;

$$\rho_{r.out} = \rho\left(h_{r.out}, s_{in}\right) = 44.136 \ \frac{kg}{m^3}$$

Given the same full load mass flow, the following area was specified for the rotor:

$$A_{n.r} = \frac{\dot{m}}{\rho_{r.out} \cdot v_{3r}} = 0.0620 \text{ m}^2$$

Assuming a 100% carry over between the stator and rotor, the full velocity triangle could. be derived for first stage of the high-pressure turbine as below:

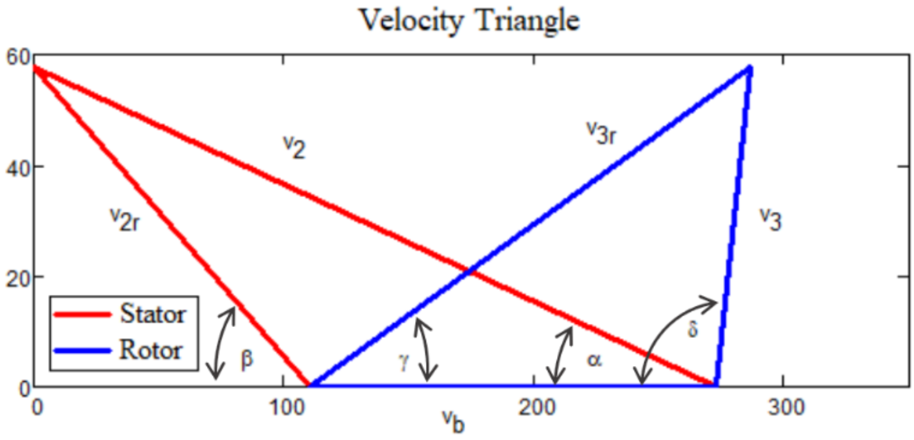

Figure A1: HP First Stage Velocity Triangle

The above nozzle sizing process was repeated for all of the HP and IP turbine stages with the following results:

Table 21: HP Turbine Nozzle Sizes

Stage	Stator (m²)	Rotor (m²)
1	0.044	0.062
2	0.046	0.066
3	0.049	0.070
4	0.052	0.074
5	0.056	0.079
6	0.060	0.085
7	0.064	0.091
8	0.069	0.098

The same method was used for the first stage of the IP turbine unit, which yielded the following representative blade characteristics:

Table 22: IP First stage blade characteristics

	Value
Stator Exit angle (°) → assumed	15.1 → 15
Reaction Ration	0.237

The constant reaction ratio across the HP and IP units demonstrated the legitimacy of the sizing method in producing consistent blading across both units. The nominal exit angle and reaction ratio was used in the sizing the IP turbine nozzle areas, with the following results:

Table 23: IP Turbine Nozzle Sizes

Stage	**Stator (m^2)**	**Rotor (m^2)**
1	0.141	0.231
2	0.158	0.260
3	0.179	0.295
4	0.206	0.341
5	0.240	0.400
6	0.287	0.481
7	0.350	0.590

Appendix B. Heat Transfer Verification

The verification of the heat transfer elements was conducted on a 12-hour section of plant data collected from the candidate unit. The purpose of the verification was to ensure expected heat transfer trends were observed through the rotor and casing components of the 1D turbine model.

The results of this verification are as below:

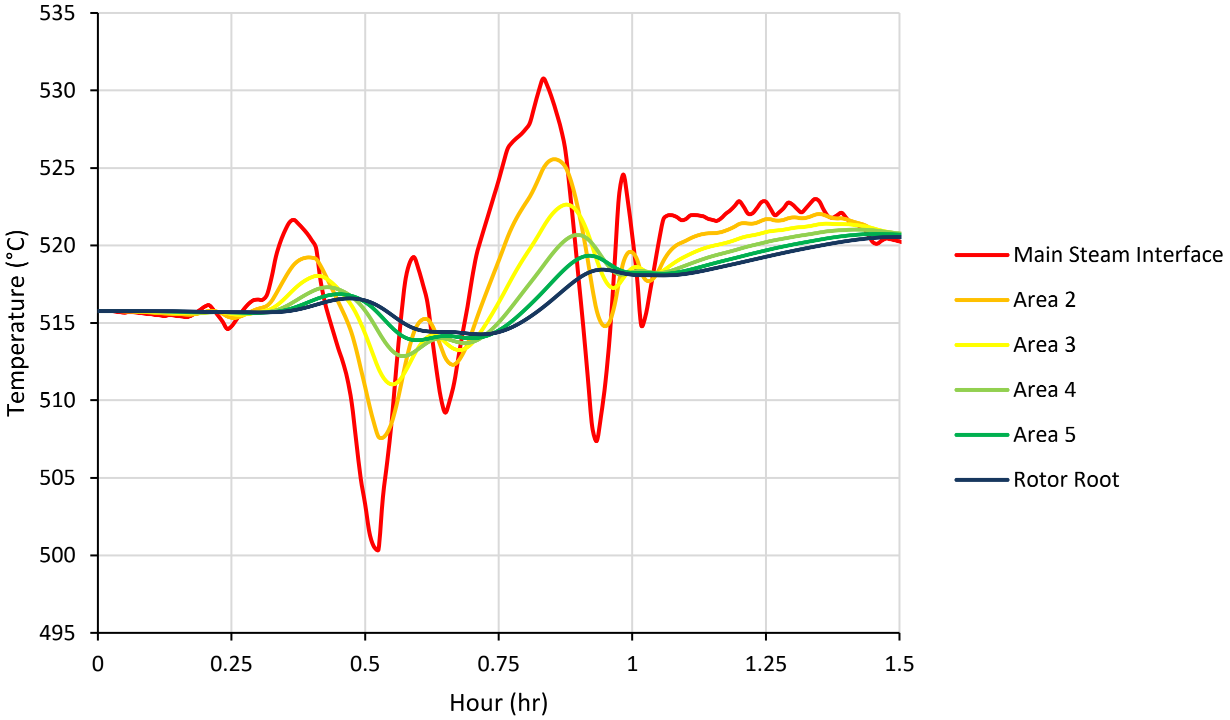

Figure B1: Rotor Heat Transfer Verification

The verification was successful as the graph clearly demonstrates the functionality of the adiabatic boundary at the rotor root and the thermal inertia exhibited by a turbine component of significant mass. This is evident by the “lag” of the inner temperatures after a period of significant main steam temperature change. It was also observed that there were periods in which the steam was heating the rotor and time in which the steam was being heated by the rotor. This was an important phenomenon to capture in the model.

The verification of the inner casing heat transfer approach was also carried out. The temperature gradients were expected to be different to the rotor as there was both an upstream and downstream convective boundary on the casing heat transfer element, allowing for heat flux through the component.

The expected heat transfer trend was observed in the verification in that the temperature gradients maintain a relative difference throughout the time of the simulation indicating a flow of heat through the component.

The regions of significant temperature change, observed in figure B1, provided an initial indication of undesirable thermal expansion during periods of significant load change or temperature change in the main steam – the motivation for the study as a whole.

Appendix C. Final 3D models

The following 3D turbine models were developed using Soldiworks, as well as sectioned and isometric turbine diagram drawings.

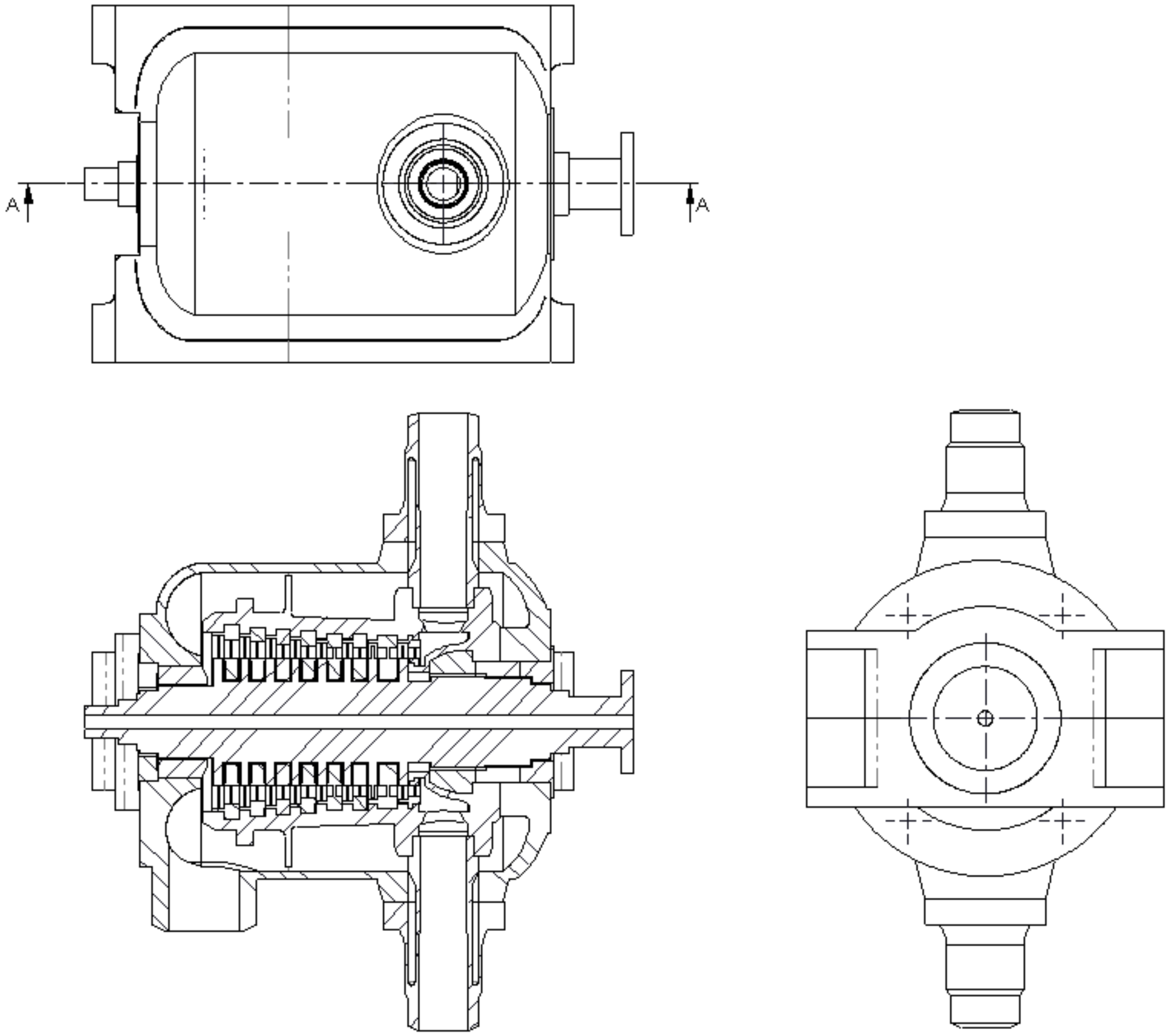

Figure C1: 3D HP Model (not to scale)

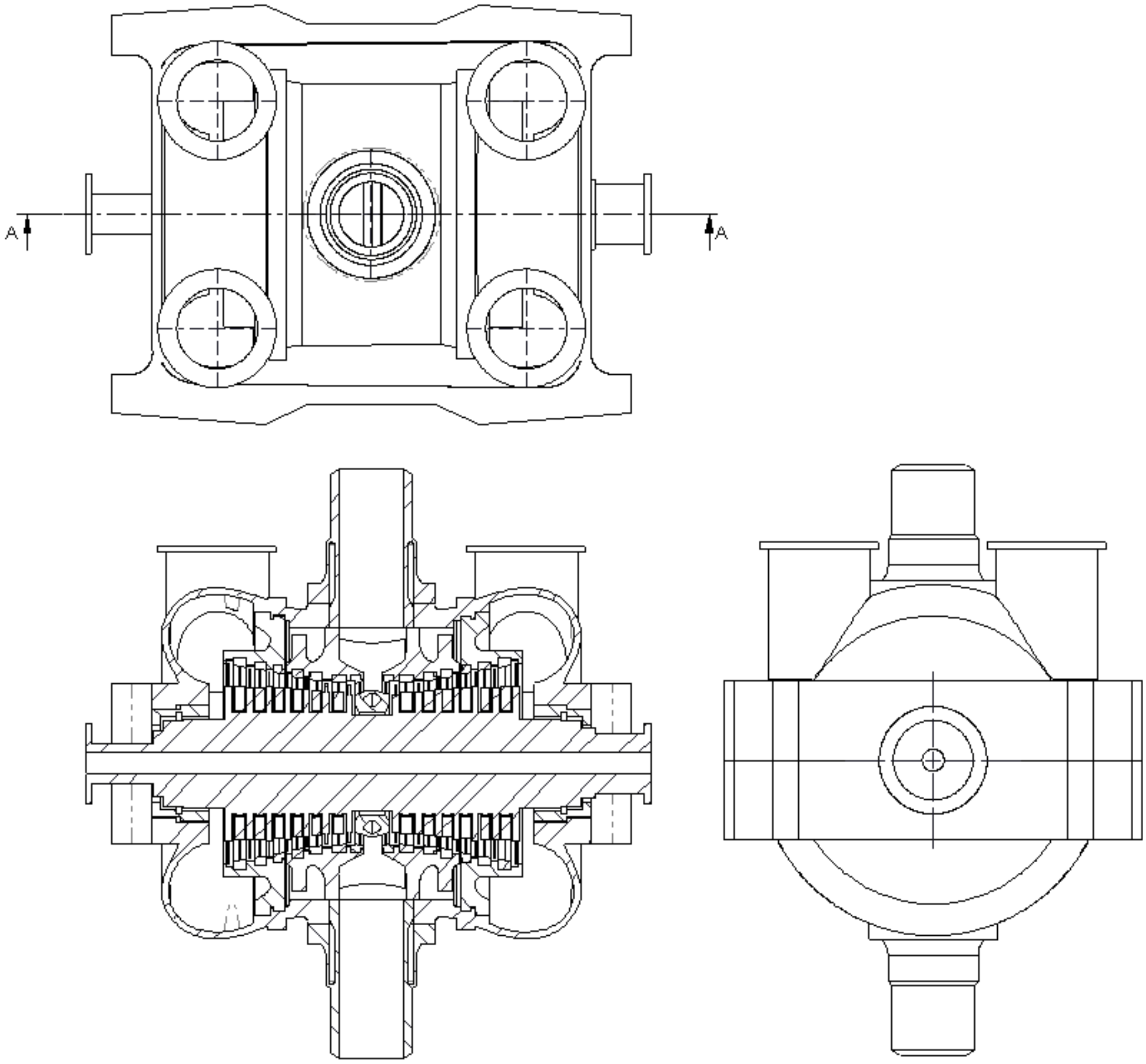

Figure C2: 3D IP Model (not to scale)